Design, Validation and Testing of an in vitro Bladder Flow Simulator

by

Kyarash MOHAMMADI

THESIS PRESENTED TO ÉCOLE DE TECHNOLOGIE SUPÉRIEURE IN PARTIAL FULFILLEMENT FOR A MASTER’S DEGREE WITH THESIS IN MECHANICAL ENGINEERING
M.A.SC.

MONTREAL, DECEMBER 12, 2025

ÉCOLE DE TECHNOLOGIE SUPÉRIEURE
UNIVERSITÉ DU QUÉBEC

BOARD OF EXAMINERS

THIS THESIS HAS BEEN EVALUATED

BY THE FOLLOWING BOARD OF EXAMINERS

Mr. Giuseppe Di Labbio, Thesis Supervisor
Department of Mechanical Engineering at École de technologie supérieure

Mr. Naeem Bhojani, Thesis Co-supervisor
Department of Surgery at
Centre de recherche du Centre Hospitalier de l'Université de Montréal

Mrs. Elmira Moosavi, President of the Board of Examiners
Department of Mechanical Engineering at École de technologie supérieure

Mr. Ali Ahmadi, Member of the jury
Department of Mechanical Engineering at École de technologie supérieure

Mr. Luc Duong, Member of the jury
Department of Software and IT Engineering at École de technologie supérieure

THIS THESIS WAS PRESENTED AND DEFENDED

IN THE PRESENCE OF A BOARD OF EXAMINERS AND PUBLIC

DECEMBER 9, 2025

AT ÉCOLE DE TECHNOLOGIE SUPÉRIEURE

DEDICATION

To my beloved aunt, Ame Ziba,

Your love, kindness, and courage continue to inspire me

This thesis is dedicated to your memory

ACKNOWLEDGMENT

I would first like to express my deepest gratitude to my supervisor, Dr. Giuseppe Di Labbio, for his guidance and constant support during this project. Thank you for being available, for your clear feedback, and for understanding my situation during difficult periods. You have been an outstanding teacher and mentor. Working with you not only allowed me to learn a tremendous amount technically, but also helped shape my personality to become more professional and independent. This has been a wonderful experience, and I am sincerely thankful for everything I learned from you.

I would also like to thank my colleagues in the lab for their help, discussions, and for standing beside me while running tests and experiments. In particular, I am grateful to Mario Corbin and Xavier Rimpault for their support with the design and realization of the simulator, to Nabil Mazeghrane for his help with the silicone work, to Serge Plamondon for his assistance with logistics and tensile testing, to Michel Drouin for his help with LabVIEW programming, to Dr. Naeem Bhojani for his help with the urology clinic visit, to Dr. Luc Duong for his support with the ultrasound work, and to Dr. Lyes Kadem for welcoming me into his lab at Concordia and allowing me to use their facilities. Your support was essential in bringing this project to life.

My deepest thanks go to my family. To my parents and my sister, Kyana, for their constant love, encouragement, and sacrifices, even from far away. I would also like to thank my partner, Mahtab, who has always supported me mentally and emotionally; All of your support helped me keep going through the most difficult moments. Finally, to the memory of my aunt, Ame Ziba, whose kindness and strength continue to inspire me and to whom I dedicate this thesis.

CONCEPTION ET VALIDATION D'UN SIMULATEUR D'ÉCOULEMENT VÉSICAL

KYARASH MOHAMMADI

RESUME

Les jets urétéraux et l'écoulement intravésical qui en résulte pourraient constituer des biomarqueurs de conditions du système urinaire basés sur la dynamique des fluides. Cependant, les mesures *in vivo* offrent un accès limité à l'écoulement. Ce mémoire présente la conception et la validation d'un simulateur d'écoulement vésical *in vitro* compatible avec l'échographie et la vélocimétrie par image de particules (PIV), permettant des études contrôlées de l'écoulement vésical en fonction de diverses conditions du système urinaire. La plateforme combine un fantôme en silicone de la vessie (taille adulte), une chambre en acrylique optiquement transparente, deux entrées urétérales actionnées par des seringues avec des moteurs linéaires programmables pour générer différentes morphologies de jet.

Le remplissage progressif de 256 à 286 mL a produit une réponse pression-volume quasi linéaire de 0 à 13,26 mmHg, avec une élastance globale de 0,44 ± 0,01 mmHg·mL^{-1} (conformité de de 1,66 ± 0,02 mL·cmH$_2$O^{-1}), indiquant une rigidité reproductible et indépendante du volume sur toute la plage testée. L'échographie Doppler couleur et pulsé a ensuite été utilisée pour caractériser trois programmes de jets urétéraux physiologiquement motivés. Les jets biphasiques (cas sain) ont atteint des durées de 3,8 ± 0,3 s tout en reproduisant les pics programmés de 20 à 90 cm·s^{-1} à 3 cm·s^{-1} près (≤ 8 %). Les jets monophasiques (événements physiologiques plus rares) ont produit des durées de 3,3 ± 0,2 s avec des pics de 20 à 30 cm·s^{-1} à moins de 9 % de la valeur cible, tandis que les jets pathologiques continus ont produit des plateaux de 4,9 ± 0.2 s à 10–25 cm·s^{-1} avec une erreur de vitesse de 6 à 15 %. Ces valeurs et morphologies correspondaient étroitement aux données humaines publiées, confirmant que le simulateur peut reproduire les signatures ultrasonores normales et dysfonctionnelles.

La vélocimétrie par images de particules (PIV) planaire dans un milieu eau-glycérine a été utilisée pour étudier les champs de vitesse, de vorticité et de dissipation visqueuse d'énergie pour les trois mêmes morphologies de jet. Avec la forme biphasique, l'énergie cinétique et sa dissipation se concentrent en deux brèves impulsions de haute intensité, avec des vitesses de pointe de 38,60 cm·s^{-1} et une dissipation locale d'environ 170 W·m^{-3}, induisant une pénétration rapide du jet et un mélange vigoureux. Avec une forme transitoire (modérément biphasique), le cisaillement est redistribué sur une période plus longue de cisaillement élevé, avec des pics moins importants (30,61 cm·s^{-1}) et des tourbillons qui durent plus longtemps dans la vessie. La forme continue a produit la dissipation instantanée la plus faible, avec des maximas spatiaux d'environ 25 à 30 W·m^{-3}, tout en maintenant un cisaillement modéré du jet pendant une plus grande partie de l'éjection, avec des vitesses ponctuelles d'environ 16,05 cm·s^{-1} et une zone de recirculation lent le long des parois. Ces résultats démontrent que le simulateur proposé permet de relier des signatures échographiques cliniquement accessibles à la dynamique de l'écoulement intravésical et offre une plateforme modulaire pour de futures études.

Mots-clés: Simulateur de flux vésical, Jets urétéraux, Échographie, Affections urinaires, Vélocimétrie par image de particules (PIV)

DESIGN AND VALIDATION OF A BLADDER FLOW SIMULATOR

Kyarash MOHAMMADI

ABSTRACT

Ureteral jet patterns and the resulting intravesical flow may offer fluid-dynamic biomarkers of urinary system dysfunction, however *in vivo* measurements offer limited access to the full flow field. This thesis presents the design and validation of an *in vitro* bladder flow simulator that is compatible with both ultrasound and particle image velocimetry (PIV), enabling controlled studies of bladder flow dynamics as a function of various conditions of the urinary system. The platform combines an adult-sized silicone bladder phantom mounted in an optically clear chamber, dual syringe-driven ureteral inlets actuated by programmable linear motors to reproduce a range of jet morphologies, and intravesical pressure sensing.

Stepwise filling from 256 to 286 mL produced a nearly linear pressure–volume response from 0 to 13.26 mmHg, with a global elastance of 0.44 ± 0.01 $mmHg{\cdot}mL^{-1}$ (compliance of 1.66 ± 0.02 $mL{\cdot}cmH_2O^{-1}$), indicating reproducible, volume-independent stiffness over the tested range. Color and pulsed Doppler ultrasound were then used to characterize three physiologically motivated ureteral jet programs. Biphasic jets (healthy case) attained ejection durations of 3.8 ± 0.3 s (4.00-s target) while reproducing programmed peaks of 20 to 90 $cm{\cdot}s^{-1}$ to within 3 $cm{\cdot}s^{-1}$ (≤ 8%). Monophasic jets (rarer physiological events) yielded 3.3 ± 0.2 s ejection durations (3.50-s target) with 20–30 $cm{\cdot}s^{-1}$ peaks within 9% of the target. Continuous jets (pathological case) produced 4.9 s ± 0.2 s plateaus (5.00-s target) at 10–25 $cm{\cdot}s^{-1}$ with 6–15% velocity error. These values and waveform morphologies closely matched published human recordings in the literature, confirming that the simulator can reproduce both normal and dysfunctional ultrasound signatures.

Planar PIV in a water–glycerin medium was used to study intravesical velocity, vorticity, and viscous energy dissipation fields for the same three inflow waveforms. Biphasic waveforms concentrated kinetic energy and dissipation into two brief bursts, with a peak speed of 38.60 $cm{\cdot}s^{-1}$ and a peak local dissipation of 170 $W{\cdot}m^{-3}$. The bursts drove rapid jet penetration and vigorous mixing. A transitional (moderately biphasic) program redistributed shear into a spatially longer high-shear region with lower peaks (30.61 $cm{\cdot}s^{-1}$) but more sustained recirculation at the upper bladder wall. The continuous program yielded the lowest instantaneous dissipation, with spatial maxima of only 25–30 $W{\cdot}m^{-3}$, yet maintained a moderate jet shear for the longest portion of the ejection, with intravesical peak velocities around 16.05 $cm{\cdot}s^{-1}$ and large regions of slow recirculating flow along the walls. Together, these results demonstrate that the proposed simulator can link clinically-accessible ultrasound signatures to intravesical flow metrics and provides a modular platform for future studies.

Keywords: Bladder Flow Simulator, Ureteral jets, Doppler ultrasound, Urinary condition, Particle Image Velocimetry (PIV)

TABLE OF CONTENTS

Page

LIST OF TABLES

LIST OF FIGURES

Page

LIST OF ABREVIATIONS

ABS	Acrylonitrile butadiene styrene
ANLUTD	Adult neurogenic lower urinary tract dysfunction
BPH	Benign prostate hyperplasia
BWT	Bladder wall thickness
BLDC	Brushless direct current
CAD	Computer-aided design
CFD	Computational fluid dynamics
CLAHE	Contrast-limited adaptive histogram equalization
CLI	Command-line interface
CT	Computed tomography
FISO	Fiber-optic pressure measurement system
FOC	Field-oriented control
FOV	Field of view
KE	Kinetic energy
LUTS	Lower urinary tract symptoms
PIV	Particle image velocimetry
PRF	Pulse repetition frequency
PVA	Polyvinyl alcohol
ROI	Region of interest
UVJ	Ureterovesical junction
VUR	Vesicoureteral reflux

LIST OF SYMBOLS

V	Bladder volume [mL]
P	Intravesical pressure [mmHg or cmH_2O]
ΔV	Volume increment between two filling states [mL]
ΔP	Pressure increment between two filling states [mmHg or cmH_2O]
C	Bladder compliance, $\Delta V/\Delta P$ [mL·cmH_2O^{-1}]
E	Elastance, $\Delta P/\Delta V$[mmHg·mL^{-1}]
D	Ureter / nozzle internal diameter [mm]
Q	Volumetric flow rate [mL·s^{-1}]
t	Time [s]
x, y, z	Cartesian spatial coordinates [mm or cm]
$\mid u \mid$	Velocity magnitude
ωz	Out-of-plane vorticity component [s^{-1}]
ε	Viscous energy dissipation rate per unit volume [W·m^{-3}]
μ	Dynamic viscosity of working fluid [Pa·s]
ρ	Density of working fluid [kg·m^{-3}]
Re	Reynolds number, Re $= \rho UD/\mu$
$KE(t)$	Spatial mean kinetic energy per unit mass in the bladder [m²·s^{-2}]
H, W, D_{bl}	Bladder ellipsoid height, width, and depth [cm]
σ	Cauchy stress in tensile tests [Pa]

INTRODUCTION

Most of the time, the urinary system works quietly yet tirelessly in the background. Over a lifetime, a person produces about 50,000 liters of urine, enough to fill a large residential inground pool. Day to day, roughly a liter or two moves from the kidneys to the bladder in a series of small packets, stored until it is time to go. When this simple rhythm is interrupted, life is interrupted too: sleep is broken, plans revolve around bathrooms, and worry sets in. This chapter provides an overview of how the urinary system works, identifies common urinary conditions, and demonstrates the need for a better approach to their diagnosis.

Anatomy and Physiology of the Urinary System

The urinary system maintains homeostasis—regulating fluid and electrolytes, clearing metabolic waste, and helping stabilize blood pressure—through the coordinated actions of (1) the kidneys, which filter blood and produce urine, (2) the ureters, which transport urine to the bladder, (3) the bladder, which stores urine, and (4) the urethra, which expels it (Hall et al., 2011). A schematic of the urinary system is shown in Figure 0.1.

The kidneys produce urine in three steps: filtration (water and small solutes pass into the filtrate), reabsorption (tubules take back needed water and solutes to the blood), and secretion (tubular cells add selected waste from blood into the filtrate). Together, these steps allow the body to remove waste while conserving the nutrients it needs (Ogobuiro & Tuma, 2025).

The ureters are two 25–30-cm long muscular tubes that transport urine from the kidneys to the bladder via peristalsis (wave-like muscular contractions). Their oblique entry into the bladder functions as a valve that helps prevent reflux. Where the ureters meet the bladder, jets of urine are expelled intermittently in pulses into the bladder cavity, known as ureteral jets.

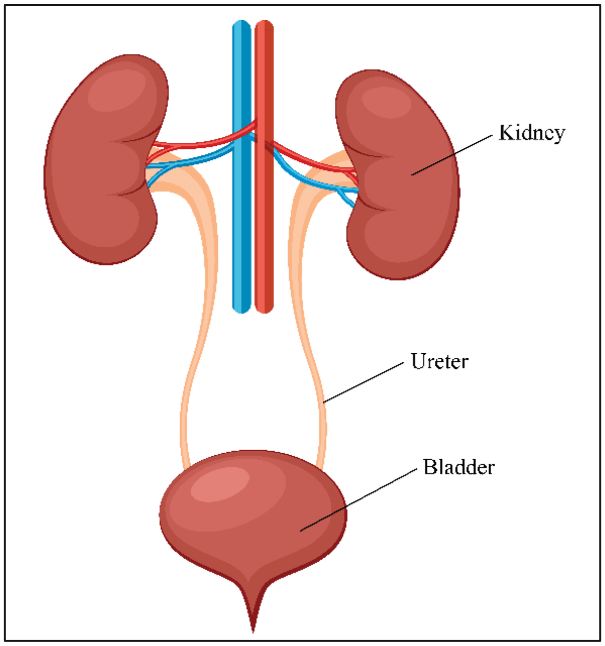

Figure 0.1 Schematic of the urinary system depicting the kidneys, the ureters, and the bladder

The bladder is a hollow, compliant muscular organ located in the pelvis and functioning as a reservoir for urine storage and voiding. In adults, normal functional bladder capacity falls within 300–400 mL and maximum bladder capacity within 300–550 mL (Lukacz et al., 2011). The typical voiding volume tends to be lower due to neural regulation mechanisms that induce a first urge to urinate at a capacity of 150–200 mL (*Campbell-Walsh Urology 12th Edition Review*, 2020). The anatomical surroundings of the bladder differ significantly between men and women given the different sexual organs. In men, the bladder sits directly above the prostate gland while in women, the bladder sits below the uterus.

The bladder wall is composed of three distinct layers, as shown in Figure 0.2. The urothelium forms the innermost lining and provides a protective barrier against urine. Surrounding it is the detrusor muscle, responsible for generating the contractile power required to empty the bladder. Finally, the outer adventitia (or serosa) provides structural support, anchoring the bladder within the pelvic cavity (Andersson & Arner, 2004).

Voiding of the bladder occurs through the urethra which passes through the urogenital diaphragm. The female urethra is short (3–4 cm) while the male urethra is long (18–22 cm), passing additionally through the prostate and the penis (Sam et al., 2025).

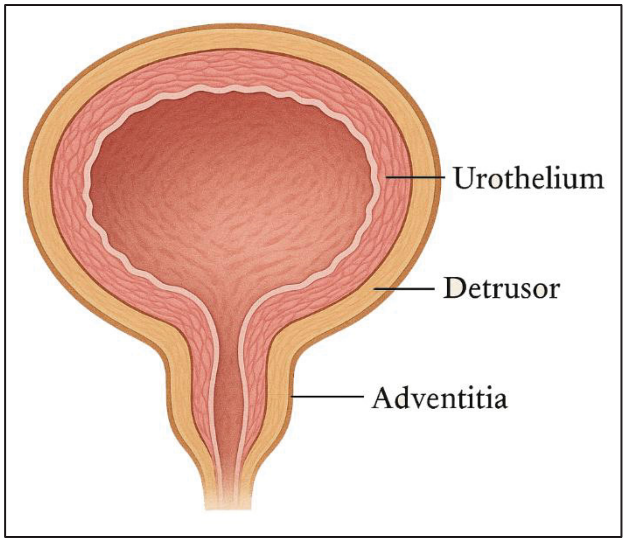

Figure 0.2 Cross-section of the bladder wall showing the urothelium (inner lining), detrusor muscle (middle), and adventitia (outer layer)

Burden of Urinary System Conditions

Diseases and dysfunctions of the urinary system represent a major health burden, affecting hundreds of millions of individuals worldwide. Various conditions such as kidney stones, bladder obstruction, urinary tract infections (UTIs), and frequent urination contribute substantially to morbidity, healthcare costs, and reduced quality of life (Yang et al., 2022).

Epidemiological studies estimate that urinary tract stones affect 10–12% of the global population, with recurrence rates approaching 50% within 10 years (Scales et al., 2012). Bladder dysfunction, including incontinence, is highly prevalent in aging populations, with over 200 million people affected worldwide (Irwin et al., 2011). In men, benign prostate hyperplasia (BPH) is one of the most common causes of bladder outlet obstruction, affecting over 50% of men older than 60 years of age and nearly 90% of those over 85 (Berry et al., 1984). UTIs, meanwhile, represent one of the most frequent bacterial infections worldwide, with up to 50% of women experiencing at least one episode in their lifetime (Foxman, 2014).

Many urinary conditions develop gradually and are only detected in their later stages or once symptoms become severe (e.g., kidney stones, chronic kidney disease). Current diagnostic methods—such as cystoscopy, uroflowmetry, and contrast imaging—remain either invasive, poorly quantitative, or unable to detect impaired urinary function at their earliest stages. There is therefore a need for diagnostic approaches that are safe, non-invasive, and sensitive enough to detect subtle functional changes early-on.

Fluid Mechanics as a Tool for Early Diagnosis

Fluid flow is highly sensitive to boundary conditions such as geometry, wall properties, fluid properties, and inflow/outflow conditions. Even small physiological changes can leave behind detectable changes in flow behavior (e.g., velocity, shear, vortex structures). This sensitivity explains why fluid mechanics has become an increasingly popular tool in the study of cardiovascular and cerebrovascular pathologies. Over the past 20 years or so, several flow-based diagnostic indicators have been developed to detect dysfunction from cardiovascular flows. For example, Gharib et al. (2006) correlated the formation time of the left ventricular vortex with dilated cardiomyopathy. Barker et al. (2014) demonstrated that dilated and stenotic conditions of the ascending and thoracic aorta present increased dissipation of kinetic energy due to viscous effects. Di Labbio & Kadem (2018) have likewise correlated viscous dissipation, cardiac vortex properties, and material transport behavior with the severity of aortic valve regurgitation. Similarly, patient specific flow modeling in arterial (Malek et al., 1999) and cerebrovascular (Cebral et al., 2011) systems show that disturbed shear and vortex structures align with sites of atherosclerosis and aneurysm progression.

The urinary system presents a parallel opportunity. The intravesical flow depends on several key parameters or boundary conditions, namely, the bladder geometry (e.g., size, shape), the bladder wall's mechanical properties (e.g., compliance, texture), the ureteral jet properties (e.g., orifice shape and size; jet angle, speed, frequency, duration, time dynamics), and the fluid properties of urine (e.g., density, viscosity, solutes, crystals). Small changes in any one of these properties must induce small and quantifiable changes in the intravesical flow. Developing flow-based metrics that best capture these subtle variations may allow clinicians to identify urinary conditions earlier than with conventional methods. Advances in experimental techniques enable the detailed analysis of the intravesical flow. Particle image velocimetry (PIV) enables quantitative flow measurements within *in vitro* models with high spatiotemporal resolution, while ultrasound allows for non-invasive *in vivo* assessment of urinary flow patterns (Price et al., 2000). Together, these methods enable a new class of experiments that can bridge the gap between fluid dynamics and urology.

Ureteral Jets and Their Physiological Importance

Ureteral jets play a central role in bladder fluid dynamics. Each jet enters the bladder as a localized pulsed stream. Color Doppler ultrasound provides a non-invasive means of observing these jets (Figure 0.3) and assessing their direction, speed, and frequency in both healthy and dysfunctional states (Burge et al., 1991).

When a urinary condition is present, jet behavior is often affected. Obstruction, such as from ureteral narrowing or BPH, may reduce or even eliminate jet activity (O'Reilly et al., 1996). Renal dysfunction can significantly alter jet velocity and volume (Jandaghi et al., 2013). In addition, recurrent UTIs are often associated with incomplete bladder emptying, which will affect the fluid dynamics induced by ureteral jets (Foxman, 2014).

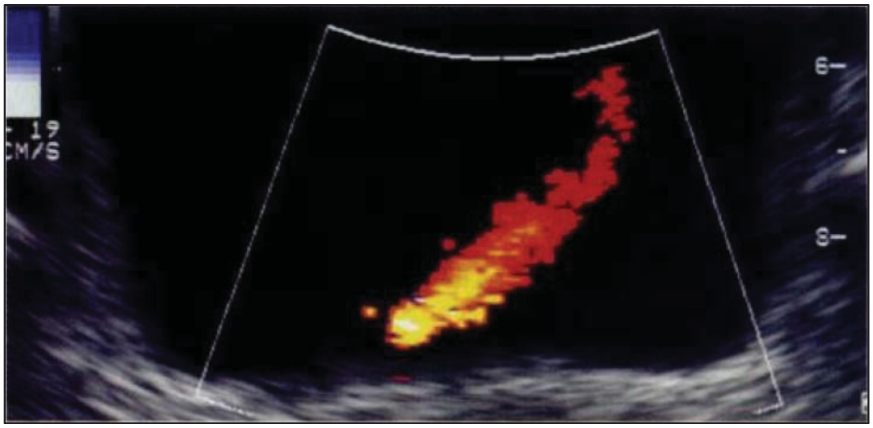

Figure 0.3 Color Doppler ultrasound image of a normal ureteral jet entering the bladder
Adapted from Burge et al. (1991)

These observations suggest that ureteral jet characteristics and the consequent flow patterns may serve as fluid-dynamic biomarkers of dysfunction. As the jets occur regularly (1–3 per minute per ureter; Hassan et al., 2021) and are accessible with clinical imaging modalities, they provide ideal conditions to apply the principles of fluid mechanics for diagnosis.

Scope of the Present Thesis

The major goal of the overarching research project is to establish a clear relationship between bladder flow patterns and urogenital conditions through sensitive flow-derived diagnostic markers compatible with various imaging modalities. This thesis aims to contribute significantly to this goal by developing a comprehensive experimental *in vitro* platform for studying physiological and pathological bladder flow dynamics. This aim is achieved through three objectives.

Objective 1 — Design of a customizable *in vitro* bladder flow simulator that can replicate physiological and pathological filling dynamics. To satisfy this objective, the simulator must include a realistic bladder model, generate customizable ureteral jets, and be compatible with both ultrasound and PIV.

Objective 2 — Validation of the simulator's physiological fidelity. To satisfy this objective, the simulator must be capable of reproducing *in vivo* color and pulsed Doppler ureteral jet signatures and intravesical pressures.

Objective 3 — Demonstration of the value of bladder flow dynamics for diagnosis using a hypothetical test case (mock study) representing the progression of a urogenital condition. To satisfy this objective, we acquire and analyze *in vitro* velocity fields within a healthy bladder model using PIV, examine the differences in flow patterns for a mock urogenital condition, and evaluate flow-based diagnostic metrics inspired by cardiovascular flow research.

Originality — This work is the first to build and validate a bladder phantom that reproduces realistic ureteral jet waveforms and quantifies their impact on intravesical flow using ultrasound and flow-field measurements.

Organization of the Thesis

This thesis is organized as follows. Chapter 1 reviews the anatomical, physiological, and imaging background for ureteral jets, bladder mechanics, urine properties, and existing urinary system simulators. Given that the thesis objectives span distinct topics (i.e., mechanical design, simulator validation, and a mock fluid dynamics study), the thesis is structured to present the methodology, results, and discussions for each objective in their own chapters. Chapter 2 presents the design, fabrication, and control of the *in vitro* bladder simulator, including the compliant bladder phantom, dual ureteral jet actuation mechanism, fluid circuits, and pressure–volume characterization. Chapter 3 validates the simulator using color and pulsed Doppler ultrasound, showing that monophasic, biphasic, and continuous jets can be reproduced with physiological timings, velocities, and overall waveform morphologies. Chapter 4 presents particle image velocimetry (PIV) measurements inside the bladder, compares three jet waveforms imitating a hypothetical development of a urinary condition, and interprets the resulting flow structures and mixing patterns. The thesis concludes by summarizing the main findings, discussing limitations, and outlining directions for future work.

CHAPTER 1

LITERATURE REVIEW

In section 1.1, we demonstrate clear relationships between the ureteral jets and urogenital conditions in the literature which serves as the motivation for this thesis. The simulator must reproduce the anatomical and physiological conditions controlling the intravesical flow. These include the bladder's geometry and mechanical properties, the fluid properties of urine, and the ureteral jet characteristics, each of which are respectively reviewed in sections 1.2 to 1.4. Lastly, in section 1.5, we provide an overview of existing simulators of the urinary system.

1.1 Why Ureteral Jets Matter

Color and pulsed Doppler ultrasound can visualize the ureteral jets emanating from the ureterovesical junctions (UVJs); see Figure 0.3. The foundational work of Cox et al. (1992) established that beyond a binary "present/absent" sign, the velocity, duration, and frequency of the ureteral jets carry important physiological and diagnostic information. In a small cohort of hydrated healthy male adults, they quantified mean peak velocity (~57 cm/s) and duration (~4.6 s), noting ~2.2 peaks per ejection event and a wide variability in inter-jet intervals (2–150 s), effectively defining normal reference ranges for subsequent comparisons.

The link between ureteral jet behavior and disease has also been assessed by color Doppler in the early 90s. Burge et al. (1991) showed that patients with unilateral ureteral stones often exhibit absent jets on the affected side or a continuous low-level signal, whereas the opposite (unaffected) side and healthy controls show distinct, pulsatile jets—thus linking waveform presence and morphology to the degree of obstruction. Later studies emphasized that reliable interpretation requires adequate observation time (≥ 10 min) because jet frequency fluctuates with hydration and physiology (Delair & Kurzrock, 2006).

Beyond obstruction, interpretation of the ureteral jet patterns and their association with various conditions has gained significant value. Leung et al. (2002) noted six Doppler waveform classes—monophasic, biphasic, triphasic, polyphasic, square, and continuous—arguing that these reflect sphincteric control at the UVJ and broader physiological state (e.g., diuresis), and reframed ureteral jets as morphological biomarkers rather than mere on/off signs (Leung et al., 2007). In a pediatric study, Gemmell et al. (2024) demonstrated that the ureteral jet angle can serve as a noninvasive screening approach for moderate–high grade vesicoureteral reflux (VUR). Moreover, pediatric enuresis cohorts show a higher incidence of immature monophasic ureteral jet waveforms and greater post-void bladder wall thickness (Choi et al., 2021), consistent with altered detrusor function and bladder remodeling (V. Y.-F. Leung et al., 2006).

Taken together, these findings demonstrate that ureteral jet properties are clinically informative markers of lower tract physiology and dysfunction. However, substantial inter- and intra-patient variability, influenced by hydration status, diuresis, age, and observation window limit the reliability of single-time interpretation. Standardized acquisition and larger condition-specific cohorts are needed to refine reference ranges and diagnostic thresholds.

1.2 Bladder Geometry and Mechanical Properties

The bladder is a distensible organ with an adult functional capacity typically ranging from 300 to 500 mL (Lamonerie et al., 2004), while the first urge to void generally occurs at 150–250 mL (Glass Clark et al., 2020). Ultrasound-based volume estimation frequently models the bladder as an ellipsoid using the formula: width (W) × depth (D) × height (H) × 0.52 (Byun et al., 2003; Gyampoh et al., 2004). Glass Clark et al. (2020) reported mean healthy bladder dimensions at 300 mL as W = 7.66 cm, D = 6.56 cm, and H = 9.41 cm based on 12 individuals.

Bladder wall thickness (BWT) and the trigone are also critical geometrical parameters. In normal adults, distended bladders typically exhibit a wall thickness of about 3 mm, while non-distended or obstructed bladders show thicker walls (Hakenberg et al., 2000). Figure 1.1 shows the trigone, with the ureteral orifices positioned approximately 2.5–5 cm apart depending on bladder distension (Rahn et al., 2007; Standring, 2016). The intramural ureter length averages about 2 cm, acting as a natural anti-reflux valve (Kirsch et al., 2009). Average ureter diameters range between 3–4 mm (Song et al., 2010).

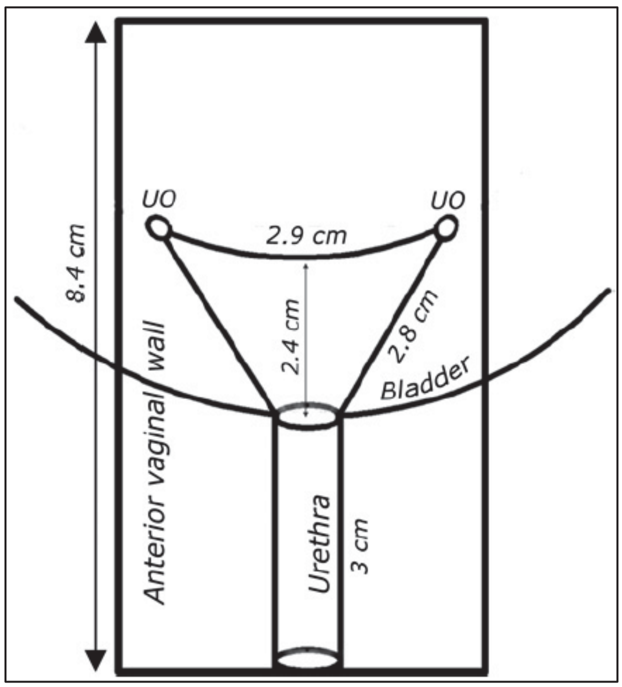

Figure 1.1 Anatomical relationships of the ureteral orifices, trigone, and urethra
Adapted from Rahn et al. (2007)

From a biomechanical perspective, bladder compliance is governed by the elastic modulus of the various layers of tissue; see Figure 0.2. Johnson et al. (2020) measured the elastic modulus of human bladder tissue as approximately 0.5 MPa at 25% strain. Porcine bladders show similar values (Li et al., 2014), validating their use for surrogate models.

1.3 Fluid Properties and Composition of Urine

Urine has a characteristic composition that influences density, viscosity, and acoustic backscatter. Urine consists of 91–96% water, with the remainder consisting of various solutes (Jesuthasan et al., 2022). The major solutes include urea, creatinine, uric acid, and electrolytes (Na^{+}, K^{+}, Cl^{-}, Mg^{2+}, Ca^{2+}), along with trace proteins, hormones, and pigments; concentrations vary with diet, hydration, and renal function (Leslie et al., 2025). Specific gravity commonly falls between 1.005 and 1.030, depending on solute concentration and temperature (UCSF Health, 2023).

The kinematic viscosity at 37°C averages ~0.83 cSt, slightly higher than water at the same temperature due to the solute content (Inman et al., 2013). Early sonographic work also explored density differences between ureteral urine and bladder urine as a contributor to jet conspicuity on ultrasound (Baker & Middleton, 1992).

1.4 Ureteral Jets: Physiology and Pathophysiology

Leung's six-waveform classification framework links ureteral jet morphology to UVJ sphincter behavior and overall physiology. Healthy adults commonly show biphasic or triphasic jets with velocities in the ~30–60 cm/s range and durations ~4–6 s when hydrated (V. Y. Leung et al., 2007). Cox et al. (1992) also provided classic benchmarks based on healthy volunteers (peak velocity ~57 cm/s; duration ~4.6 s), as noted in the introduction. In healthy adults, under a 10-minute observation protocol, Yildirim et al. (2010) reported peak ureteral jet velocities around 30 cm/s with durations of about 4.4 to 5.2 s and roughly 3.6 jets per 10 minutes.

Color and pulsed Doppler studies consistently show that ureteral jet patterns change with pathology, and that these changes are quantifiable when observation time and hydration are controlled. In unilateral obstruction from stones or distal strictures, the symptomatic ureter often shows absent jets, a continuous low-level signal, or markedly blunted periodic bursts, whereas the contralateral ureter remains near normal. For example, in a stone cohort studies (Burge et al., 1991; Jandaghi et al., 2013), 15–30 minutes after ingesting 750–1000 mL of fluid, the obstructed side demonstrated large reductions in jet frequency, duration, and peak velocity compared with the opposite side, with averages around 0.6 vs. 3.0 jets per minute, 1.2 vs. 5.3 seconds, and 5 vs. 32 cm/s. The proposed cut-offs for obstructed vs. contralateral differences yielded high sensitivities and specificities for obstruction.

Beyond mechanical blockage, vesicoureteral reflux in children has been approached using jet trajectory and angle as noninvasive options in place of voiding cystourethrography (VCUG). A recent systematic review by Gemmell et al. (2024) reported that larger ureteral jet angles correlate with moderate to high reflux grades. However, they noted marked heterogeneity in acquisition protocols, which limits the value of pooled estimates, and suggesting that standardized methods and prospective validation in age-defined cohorts are required. Enuresis and detrusor overactivity cohorts show a higher prevalence of immature monophasic jets than controls and, within affected children, these immature patterns correlate with increased post-void bladder wall thickness and detrusor overactivity (Choi et al., 2021).

Table 1.1 summarizes the ureteral jet literature discussed above, listing the major points of the design and cohort of the studies along with the ureteral jet characteristics.

Table 1.1 Comparative ureteral jet parameters in healthy and diseased ureters (compiled from published studies)

Study	Study Design and Cohort	Peak velocity (cm/s)	Duration (s)	Frequency	Notes
Healthy cohorts					
Cox et al., 1992	15 healthy adults; oral hydration; observed up to 30 min	~57	4.6	—	Approximately 2.2 peaks per jet
Jandaghi et al., 2013	Patients with unilateral stones, contralateral non-obstructed ureters	32	5.3	3 jets/min	Values from unaffected ureters
Yıldırım et al., 2010	31 healthy volunteers; 10-minute observation	~30	4.4–5.2	~3.6 jets/10 min	Reported per 10-min interval
Diseased cohorts					
Burge et al., 1991	26 patients with unilateral ureteral stones	—	—	—	Absent or continuous jet on obstructed side
Jandaghi et al., 2013	46 patients with ureteral stones, obstructed side	5.4	1.2	0.6 jets/min	Clear reduction compared to contralateral side
Yıldırım et al., 2010	24 patients with non-obstructive renal stones	35.5 / 31.5	5.7 / 4.7	4.4 vs. 3.6 jets/10 min	Monophasic patterns dominant on affected side
Hassan et al., 2021	97 patients with ureteral stones; 10-minute observation	—	—	0.7 vs. 2.9 jets/min (obstructed /normal)	Frequency strongly discriminates obstruction

1.5 Prior Bladder Simulators and Their Purposes

Our goal is to build a customizable *in vitro* bladder flow simulator that reproduces bladder anatomy and physiology while also being compatible with quantitative flow measurement modalities (i.e., ultrasound and PIV). To our knowledge, no published system integrates all of these capabilities on a single platform. Below, we survey the existing simulators.

Existing *in vitro* and training models of the bladder include educational phantoms as well as mechanical systems for research. Commercial bladder scanner phantoms (e.g., Yezitronix BL-RG-3.1) are designed for ultrasound training and post-void residual/volume calibration. They are robust and convenient but use rigid or semi-rigid constructs prioritizing geometric realism and repeatability over bladder compliance (*Bladder Scanner Phantom*, n.d.). High-fidelity abdominal/pelvic ultrasound phantoms (*Female Pelvic Ultrasound Phantom Full Set KYOTO KAGAKU*, n.d.) similarly support anatomy scanning skills, probe handling, and basic pathology modules. Neither of these systems reproduce ureteral inflow.

Soft-tissue endoscopic trainers, such as FlexBlad, are engineered for realistic cystoscopy practice, with expandable silicone bladders that emulate distension and interior anatomy (Choi et al., 2021). These devices advance anatomical fidelity and compliance, yet they are not configured to reproduce ureteral inflow. Research phantoms have introduced pressure–flow validated filling/voiding rigs. A recent *in vitro* bladder model reproduced vesicoureteral reflux and demonstrated its effect on stent encrustation patterns (Zheng et al., 2022). Similarly, the SIMBA phantom (Ahyou et al., 2023) focuses on pressure–volume behavior during filling and voiding using a silicone bladder in an airtight chamber—appropriate for urodynamics education and testing.

While all phantoms and simulators mentioned above each have their specific purposes and value, inclusion of the ureteral jets remains outside their scope, and therefore they do not adequately model bladder filling. Moreover, most existing platforms do not support PIV for detailed quantitative flow study. We therefore conclude that there exists no anatomically- and physiologically-accurate bladder simulator that fully reproduces bladder filling dynamics suitable for the study of the relationship between intravesical flow and urogenital conditions. Table 1.2 summarizes the key features of existing bladder simulators.

Table 1.2 Examples of prior bladder simulators and phantoms

Study / Source	Purpose	Compliance and Mechanical Features	Imaging Modalities
Yezitronix Bladder Scanner Phantom	Calibration and training for bladder volume or post-void residual scanning	Rigid or semi-rigid; not physiologically compliant	Ultrasound
Kyoto Kagaku Ultrasound Phantoms	General pelvic and abdominal ultrasound training	Training-focused; not designed for dynamic filling	Ultrasound
FlexBlad (Zong et al., 2021)	Cystoscopy and endoscopy training using a soft, expandable bladder	Yes—soft phantom with realistic expansion	Endoscopy; ultrasound possible
Zheng et al., 2022	Urodynamics and stent or vesicoureteral reflux research	Pressure–flow validated silicone bladder	Pressure/flow; ultrasound compatible
SIMBA phantom (ICS 2023)	Pressure–volume curve simulation	Silicone bladder in closed chamber	Pressure–volume; ultrasound possible

CHAPTER 2

BLADDER FLOW SIMULATOR DESIGN AND IMPLEMENTATION

This chapter concerns the first objective of this thesis, namely, to design and implement a modular bladder flow simulator with anatomical and physiological accuracy that permits the study of the ureteral jets and the resulting bladder flow using ultrasound and particle image velocimetry. The simulator is designed to be modular in the sense that it permits the simulation of a variety of healthy and dysfunctional urogenital conditions. The chapter begins with an overview of the bladder flow simulator in section 2.1. The subsequent sections (2.2 to 2.4) respectively discuss each of the three major design steps of the simulator: (2.2) the design, fabrication, and mechanical characterization of the bladder phantom, (2.3) the implementation of the ureteral jets, and (2.4) the surrounding design features (i.e., the octagonal chamber, the working fluid, and the fluid circuits). Section 2.5 discusses the integration of pressure measurements within the simulator and evaluates the intravesical pressure-volume response.

2.1 Overview of the Bladder Flow Simulator

The simulator is comprised of three main subsystems: the bladder fluid circuit, the ureteral jet actuation mechanism, and the enclosure fluid circuit. The design emphasizes modularity, anatomical realism, and compatibility with ultrasound imaging and particle image velocimetry (PIV). A schematic overview of the bladder flow simulator is shown in Figure 2.1.

The system includes a compliant silicone bladder that reproduces gross morphology and wall mechanics within a physiological range. The bladder phantom is housed in a transparent octagonal chamber and the system is separated into two fluid circuits: one for the bladder interior (bladder fluid circuit) and one for the surrounding environment (enclosure fluid circuit). The bladder fluid circuit includes ports for bladder filling and drainage (including the ureteral jets), a pressure sensor to monitor intravesical pressure in real time, and valves to regulate flow. The ureteral jets, responsible for physiological filling of the bladder, are actuated using a piston-cylinder mechanism (commercially available syringes) driven by programmable linear motors and controlled via LabVIEW (NI, Emerson; Ferguson, United States of America). Each ureteral jet is customizable in terms of waveform, frequency, volume per pulse, and mean flow rate. The enclosure fluid circuit surrounding the bladder phantom permits optical and acoustic access to the bladder. A peristaltic pump optionally drives the filling and voiding process for both the bladder and enclosure fluid circuits, while valve manifolds manage fluid routing.

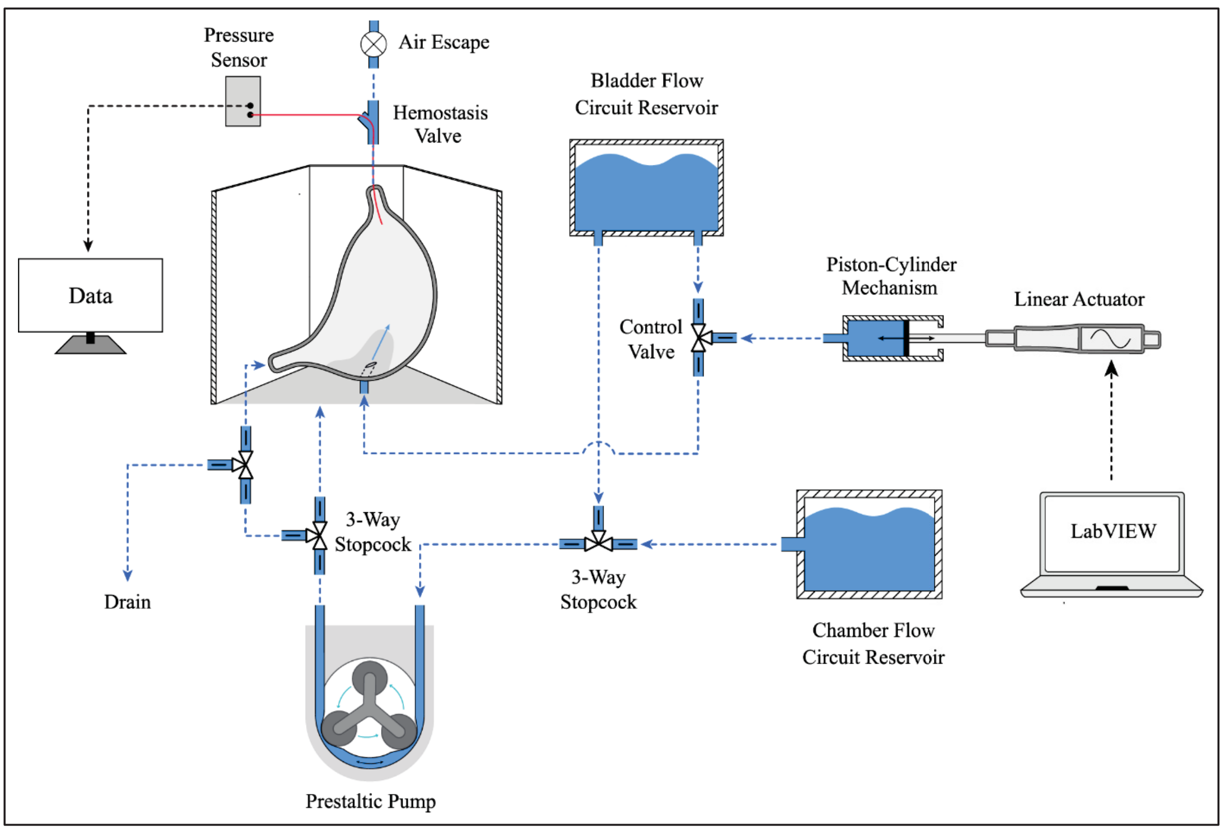

Figure 2.1 Schematic of the bladder flow simulator showing the actuator, bladder chamber, fluid circuits, and control components

2.2 Bladder Phantom Design and Fabrication

2.2.1 Bladder Geometry

The bladder geometry was modeled as an ellipsoid, consistent with imaging studies (Standring, 2016). The dimensions are determined using the ultrasound ellipsoid volume approximation (W×D×H×0.52) (Byun et al., 2003; Gyampoh et al., 2004). We selected rounded, representative dimensions (W = 8.0 cm, D = 6.8 cm, H = 9.0 cm) that preserve the reported aspect ratios. Using the ellipsoid volume formula, these dimensions yield a volume of 256 mL. This is representative of the physiological volume at which an individual typically senses the urge to void (Wyndaele, 1998). This volume is also in alignment with bladder ultrasound examinations where patients are required to have a full bladder, thus providing a clinically-relevant baseline condition for the simulator.

2.2.2 Ureter, Urethra, and Umbilical Ligament Placements

Four openings were incorporated into the bladder phantom. Most important to the simulator are the two ureteral inlets from which the ureteral jets are ejected. The angles of the ureteral jets must be anatomically realistic to ensure a correct jet trajectory within the bladder. According to cadaveric and imaging studies (Juri et al., 2016), the human ureterovesical junctions (UVJs) are positioned at a mean angle close to 70° relative to the oblique plane (*xy*-axis) and 45° relative to the vertical plane (*xz*-axis) (Figure 2.2). The urethral outlet was placed at the bladder neck (apex of the trigone at the base of the bladder), with the center-to-center distance from each ureteral orifice to the internal urethral orifice set to 2.5 cm in the contracted state, and the ureteral orifices 2.5 cm apart, matching adult anatomic measurements (Shermadou et al., 2025). The urethral outlet is included in the simulator to allow for bladder voiding and optionally for initial bladder filling. The median umbilical ligament (or urachus) is a fibrous structure that anchors the bladder to the anterior abdominal wall. In the simulator, it serves two functions: (1) it is likewise used as a structural support for the bladder, and (2) it is used as a fourth opening which serves as a vent port to allow air to escape from the bladder phantom during initial filling.

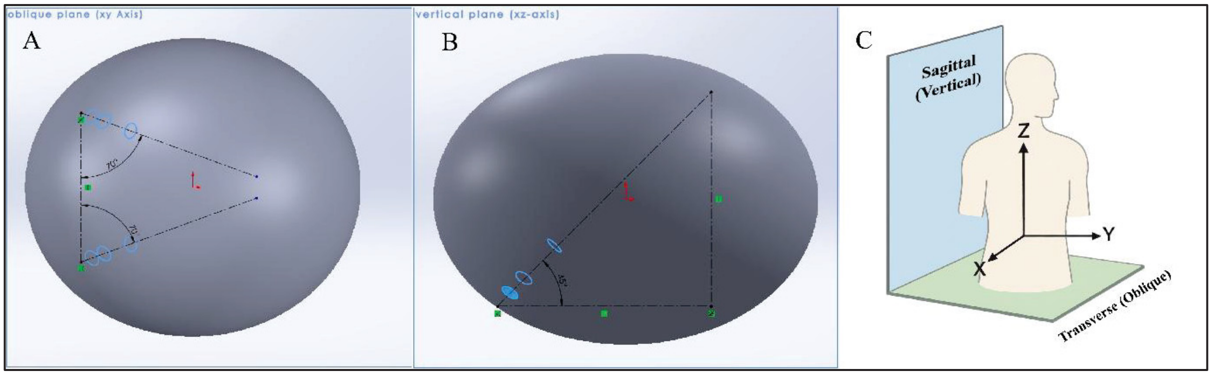

Figure 2.2 Design layout of orifice orientations and reference planes, (a) UVJ angle measured relative to the vertical *xz* (sagittal) plane, (b) UVJ angle measured relative to the oblique plane (*xy*), (c) reference body planes and axes, showing the sagittal and oblique planes

2.2.3 Fabrication Process

To produce the bladder phantom, a 3D model of the bladder interior was designed in SolidWorks based on the selected ellipsoid dimensions (Figure 2.2). The core was 3D-printed on a Fortus 450mc using the SR30 soluble support material (Stratasys; Eden Prairie, MN, USA). After printing, the surface was progressively wet-sanded to remove layer lines and achieve a smooth finish: 100, 150, 200, and 300 grit sandpaper were sequentially used to remove the visible ridges, followed by 600, 800, 1000, 1500, 2500, and 3000 grit to polish the model. The model was rinsed and dried prior to coating. To define the ureteral and urethral ports, polished ABS rods were used as removable cores. Threads were cut on the rod ends and matching threads were tapped into the printed core to allow screw-in placement and easy removal (Figure 2.3a). The smooth model was then coated with silicone rubber to form the bladder wall, after which the SR30 interior was dissolved in a warm, soapy water bath, leaving the cured silicone wall intact, representing the bladder phantom.

To form the bladder wall, Solaris silicone (Smooth-On; Macungie, United States of America) was selected due to its transparency and elastic properties, which made it well-suited for replicating the compliant nature of bladder tissue. The silicone has Shore 15A hardness, a 100% modulus of 0.17 MPa (25 psi), an elongation at break of 290%, and a refractive index of 1.41 (Smooth-On, Inc., n.d.). The silicone was applied in seven successive layers over the model, with each layer cured individually to achieve an average final wall thickness of approximately 3.0 mm, closely matching reported bladder wall thickness (~3.35 mm) at the baseline volume of 256 mL in both men and women (Hakenberg et al., 2000). To ensure uniform thickness across the bladder surface, the model was placed on a two-axis rotating platform that moved continuously during the curing process. This motion allowed the silicone to spread evenly over the model surface, eliminating localized buildup and resulting in a consistent wall thickness.

The material was chosen to match the mechanical properties of human bladder tissue. Given the Shore A hardness from the supplier, we estimated the Young's modulus using the Gent relation for elastomers (Meththananda et al., 2009):

$$E\,[\mathrm{MPa}] = \frac{0.0981\,(56 + 7.62336\,S)}{0.137505\,(254 - 2.54\,S)} \tag{2.1}$$

where S is the Shore A hardness. Solving for a target $E = 0.5$ MPa gives $S \approx 13$, so a silicone with Shore 15A hardness satisfies rather well the elastic modulus requirement. The selected Solaris silicone is estimated to have an elastic modulus of $E \approx 0.56$ MPa using the same equation (Meththananda et al., 2009).

After curing, the PVA mold was dissolved in a sodium hydroxide (NaOH) bath within an ultrasonic tank over 48 hours. This method ensured full dissolution of the model through its inlets (ureteral orifices, urethra, and urachus) without compromising the silicone integrity. To maximize optical transparency for PIV and eliminate micro-scratches left by sanding the model, the interior surface of the finished bladder phantom was coated with an additional thin layer of the same silicone and allowed to cure, yielding a smooth, clear lumen (Figure 2.3b).

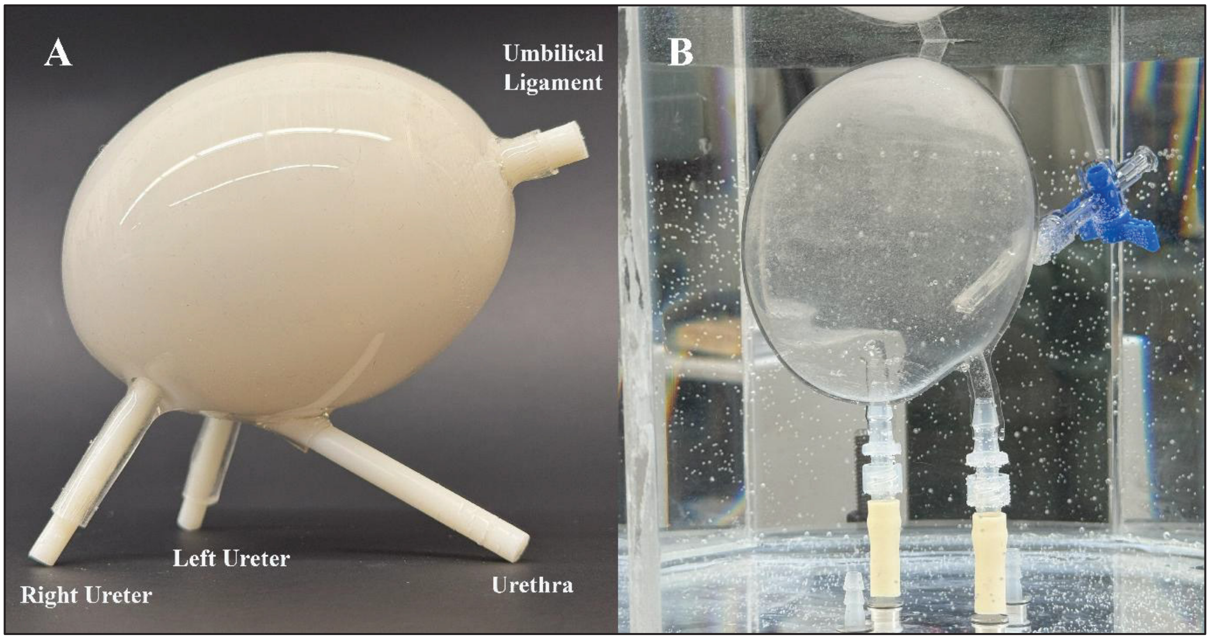

Figure 2.3 (a) Silicone-coated bladder mold with threaded rods installed
(b) Finished phantom placed in the simulator

2.2.4 Mechanical Characterization of the Bladder Phantom Material

To ensure the phantom replicated the elastic modulus of the human bladder at physiological volumes, uniaxial tensile testing was performed on four standardized dog-bone specimens of the selected silicone, prepared according to ASTM D412. Tests were conducted using an Instron universal testing machine (Norwood, United States of America) at a crosshead speed of 500 mm/min, with force measured by a calibrated load cell and strain monitored using a clip-on extensometer attached to the gauge length (Figure 2.4).

Figure 2.4 Uniaxial tensile testing setup on the Instron universal testing machine with a dog-bone silicone specimen and clip-on extensometer

Stress and strain were computed as $\sigma = F/A_0$ and $\varepsilon = (L - L_0)/L_0$, where F is the measured force, A_0 the initial cross-sectional area, L the instantaneous gauge length, and L_0 the original length. The resulting stress-strain curves (Figure 2.5) exhibited a characteristic linear elastic profile. In the low-strain regime, corresponding to physiological bladder loading, the initial slope (Young's modulus) averaged 0.2055 MPa across four realizations. For comparison, uniaxial tests on human female bladder tissue report stiffnesses ranging from 1.0 to 4.1 MPa, with a mean of 1.9 ± 0.2 MPa (Martins et al., 2011). Our silicone therefore lies at the lower end of reported bladder wall moduli under physiological filling, but remains within the correct order of magnitude for a compliant bladder wall at volumes of approximately 250–300 mL. The residual discrepancy between measured and estimated elastic modulus likely arises from fabrication-related factors such as dust, micro-bubbles, micro-scratches, and small variations in base-to-curing-agent ratio or curing environment.

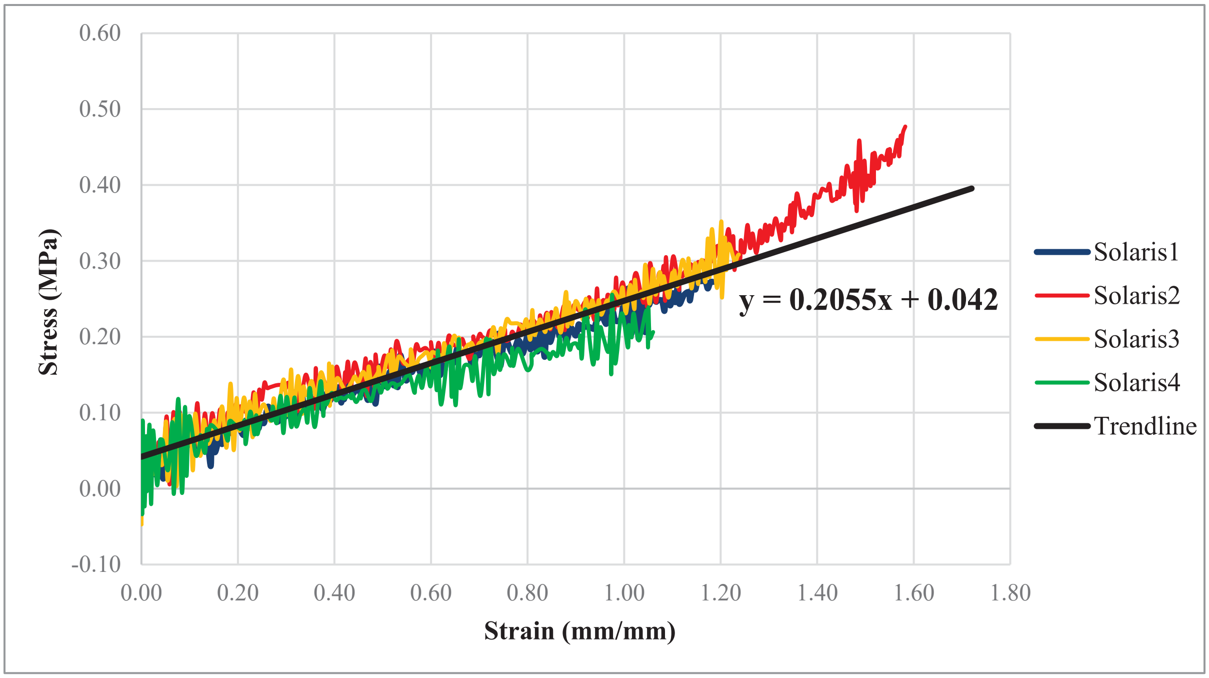

Figure 2.5 Stress–strain response of Solaris silicone samples for bladder phantom fabrication Data from four specimens (Solaris1–Solaris4) are shown

2.3 Ureteral Jet Actuation System

Each actuator assembly consists of a precision linear actuator with micrometer-scale resolution and programmable step control, a syringe holder designed to accommodate standard medical syringes ranging from 10 to 50 mL, and custom clamps and slide rails to ensure proper alignment and minimize mechanical backlash. To replicate physiologically-accurate ureteral jets, piston–cylinder mechanisms (syringes) were driven by two Ultra Motion A-series servo cylinders (model A1PZ9C) (Figure 2.6). Each actuator integrates a brushless DC (BLDC) motor with field-oriented control (FOC) and absolute position feedback, providing closed-loop position/velocity control. Our configuration uses the standard ball screw (0.125 in lead) with a 5.75 in stroke, a linear resolution of ~3.1 µm (0.00012 in), a backlash of ~0.005 in, and a top speed of ~14 in/s (load-dependent) (*Servo Cylinder Configurator – Ultra Motion*, n.d.). The A1 series operates on 8–36 VDC, is IP50, and is specified for operation between −40°C and

80°C. Controller "P" supports command lines over serial (RS-485) using analog voltage or current inputs; we interfaced via a serial converter.

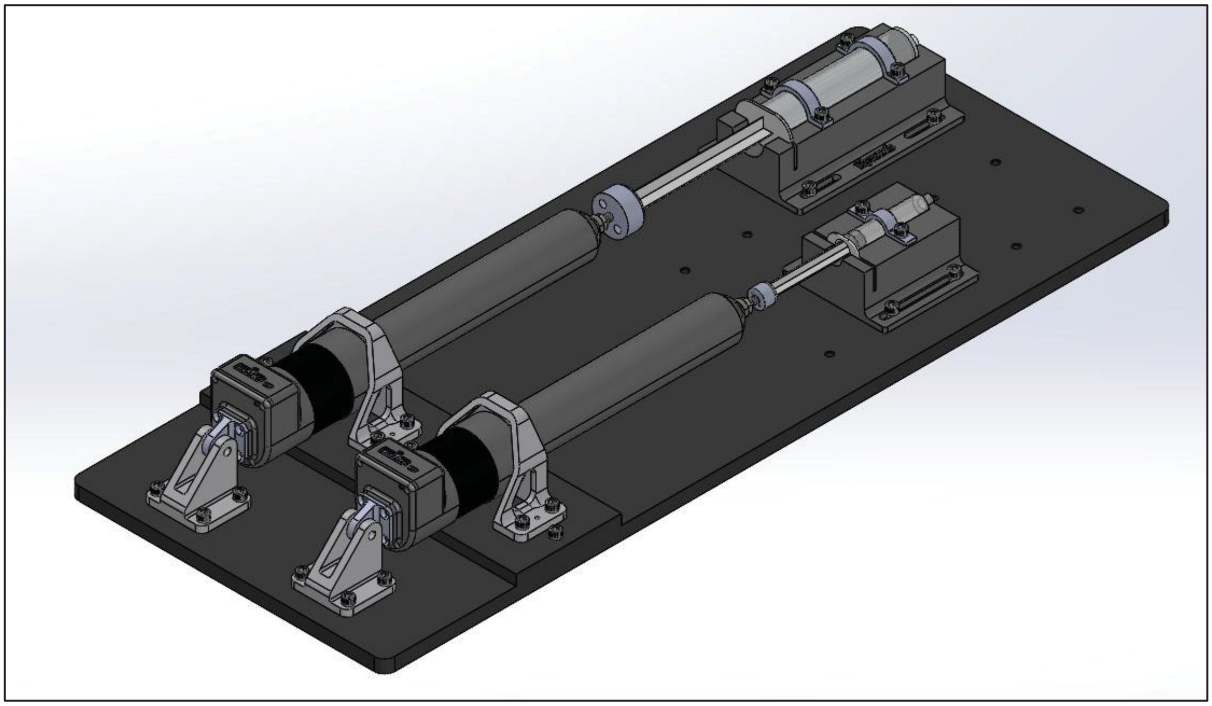

Figure 2.6 Dual-actuator syringe drive: two Ultra Motion A-series servo cylinders driving 10–50 mL syringes in adjustable holders on linear rails, mounted to a rigid baseplate

Each actuator was coupled to a 10 mL syringe (or 50 mL for later applications). This 5 to 10 mL stroke volume was chosen to generate physiological ureteral jet velocities rather than to match a specific bolus volume. Fluid delivery was routed through a three-port manifold consisting of an input from the actuator-driven syringe, a reservoir inlet for recharging the syringes, and an output directed to the ureteral inlet port of the bladder phantom. The ureteral outputs were connected to the bladder via flexible tubing that inserted into the bladder inlet extensions via barbed fittings.

2.3.1 Waveform synthesis and actuator command generation

Each waveform was programmed using an in-house Python code that generated a velocity–time profile via cubic spline interpolation fitted to ureteral jet waveforms observed in the literature via pulsed Doppler. Ureteral jet control using the linear actuators is performed by specifying displacement, which is determined by integrating the velocity waveform and adjusting for the syringe–ureter area ratio.

Ureteral jet waveforms were reconstructed from the literature (V. Y. Leung et al., 2007) by (i) digitizing peaks and troughs into normalized time–velocity pairs, (ii) enforcing smoothness via cubic spline interpolation, and (iii) mapping the resulting velocity-time waveform to position commands for the actuator.

Normalization. We parametrize all waveforms to have a normalized time $\tau \in [0,1]$ and critical points at τ_i having normalized velocity $v_n(\tau_i) \in [0,1]$. For a waveform with physical peak speed $V_{\max}$ (case-specific), the ureteral jet speed $v_u(\tau)$ is simply given by

$$v_u(\tau) = V_{\max}\, v_n(\tau). \tag{2.2}$$

Four case-dependent quantities $(v_n, V_{\max}, \tau_i, T)$ are set per experiment based on ultrasound measurements in the literature.

Flow continuity and piston velocity. With respective ureter and syringe cross-sections $A_u = \frac{\pi d_u^2}{4}$ and $A_s = \frac{\pi d_s^2}{4}$, mass conservation $Q(\tau) = A_u\, v_u(\tau) = A_s\, v_p(\tau)$ gives the piston velocity as

$$v_p(\tau) = \frac{A_u}{A_s}\, v_u(\tau). \tag{2.3}$$

The normalized velocity profiles were scaled to physiologically relevant peak velocities, typically ranging from 25 to 90 cm/s depending on the jet type. The diameters of the ureters and syringe are respectively 3.5 mm and 15 mm respectively.

Ejection duration and spline construction. A cubic spline interpolation was then employed to generate smooth, continuous velocity profiles. An ejection duration T defines physical time $t = T\,\tau$. We fit a cubic spline $\widehat{v_p}(t)$ through $\{\left(t_i, v_p(\tau_i)\right)\}$ with $t_i = T\,\tau_i$, ensuring C^2 continuity and zero end curvature:

$$\widehat{v_p}(t_i) = v_p(\tau_i), \tag{2.4}$$

For the end points we only used fixed value conditions. The spline is then sampled uniformly in time to produce a smooth velocity profile for actuation.

Displacement and command mapping. Piston displacement is obtained by time integration,

$$x(t) = \int_0^t \widehat{v_p}(\xi)\ d\xi \tag{2.5}$$

numerically integrated using the cumulative trapezoidal method.

$$x_k = x_{k-1} + \frac{\Delta t_k}{2}(v_{k-1} + v_k) \tag{2.6}$$

For an actuator with usable stroke S_{full} and command range $[PA_{\min}, PA_{\max}]$, displacement is mapped linearly to position commands:

$$PA(t) = PA_{\min} + \frac{x(t)}{S_{\text{full}}}(PA_{\max} - PA_{\min}) \tag{2.6}$$

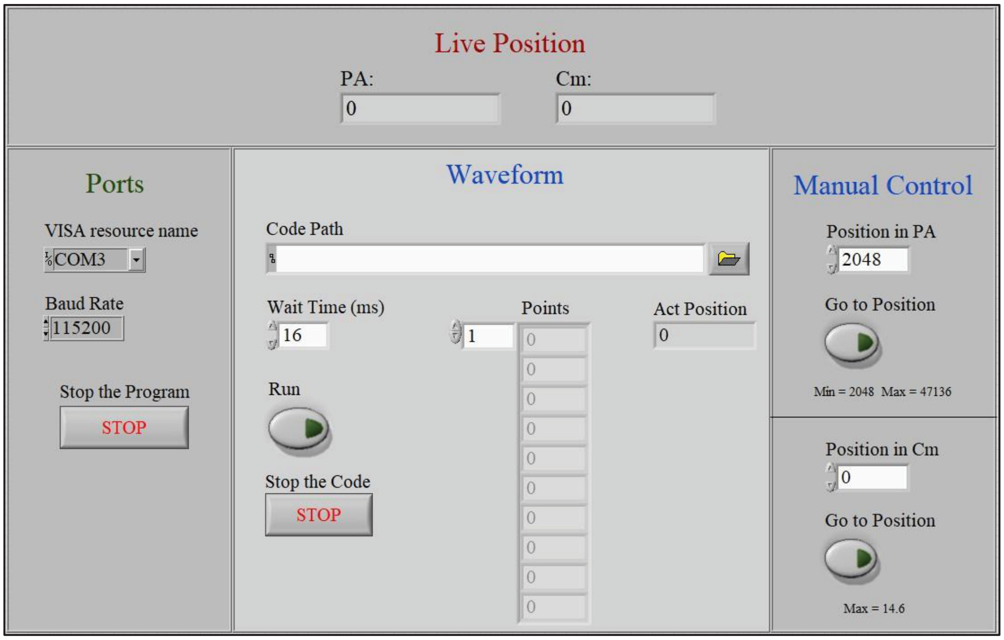

Figure 2.7 LabVIEW program front panel to control the actuators for ureteral jet ejection

The resulting sequence $\{ PA(t_k) \}_{k=1}^{N}$ were converted into actuator position commands based on the actuator's calibrated stroke length (5.75 inches) and command range (2048-47136) and saved as tab-separated files that were imported into LabVIEW for execution, with fixed time steps between points (ranging from 5 to 18 milliseconds) ensuring smooth, accurate motion control.

Multiple jet patterns were programmed to represent distinct physiological and pathological conditions. Biphasic jets, which are characteristic of healthy ureteral flow, were implemented in LabVIEW. These patterns included variations in peak velocity (25–75 cm/s) and jet duration (3–5 s) to reflect inter- and intra-patient variability observed in clinical ultrasound studies. Pathological or dysfunctional patterns were generated to mimic abnormal flow conditions. We implemented monophasic jets, characterized by a single-peak waveform with reduced velocity (35 cm/s) and prolonged duration, typically associated with impaired ureteral peristalsis. We also implemented continuous jets, representing non-pulsatile ureteral output as observed in severe obstruction cases, by maintaining a steady velocity (100 cm/s) over the programmed duration (Burge et al., 1991).

2.4 Transparent Chamber and Fluid Environment

The bladder phantom and its surrounding environment were enclosed in a transparent octagonal acrylic chamber designed to support flow visualization and additional testing conditions. The structure consisted of eight 8.5 × 5 in vertical plates forming the walls and the assembled octagonal structure measured 11 × 11 in, having a total volume of 16 814 cm^3 or 16.8 L. The octagonal box provides 8 clear optical views for PIV imaging while minimizing flow distortion (i.e., the perpendicularity between the laser and camera is easier to ensure).

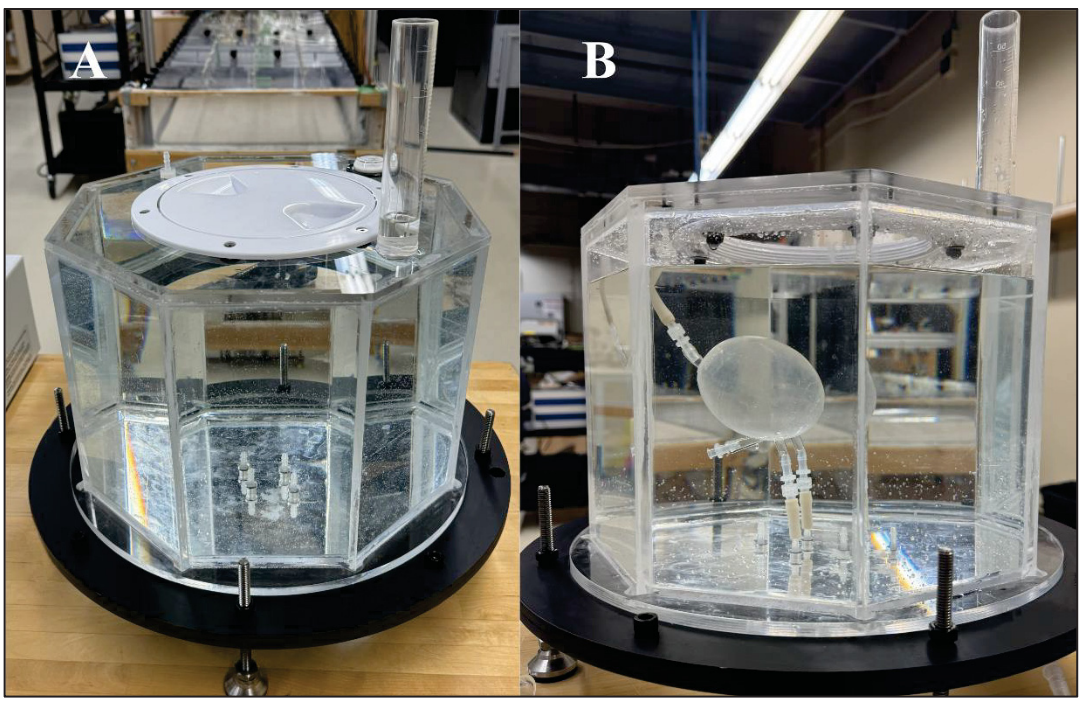

Figure 2.8 Octagonal acrylic chamber with surrounding bath: (a) chamber with access lid, (b) chamber housing the silicone bladder phantom and ureter inlets

A watertight boat-style hatch lid was installed on the top surface to provide convenient access for system assembly, phantom placement, and internal adjustments. Ports were machined into the chamber base and top plates to accommodate tubing for fluid injection and drainage, pressure sensors, and optical equipment such as cameras and ultrasound probes. Drainage outlets at the base allowed for bladder voiding and chamber emptying. A visual fluid-level with marked volume indicators enabled additional monitoring of ureteral jet ejection volume and a means to tune baseline intravesical pressure (Figure 2.8).

To simulate intra-abdominal pressure conditions, the chamber could be partially or fully filled with a surrounding fluid medium, normally the same as that used in the bladder fluid circuit. Initially, a salt–water solution was used to approximate the kinematic viscosity of urine for ultrasound imaging. For PIV measurements, the fluid is replaced with a water–glycerin mixture, which provided better optical matching with the silicone to minimize refraction errors. Figure 2.9 illustrates the complete setup of the bladder simulator.

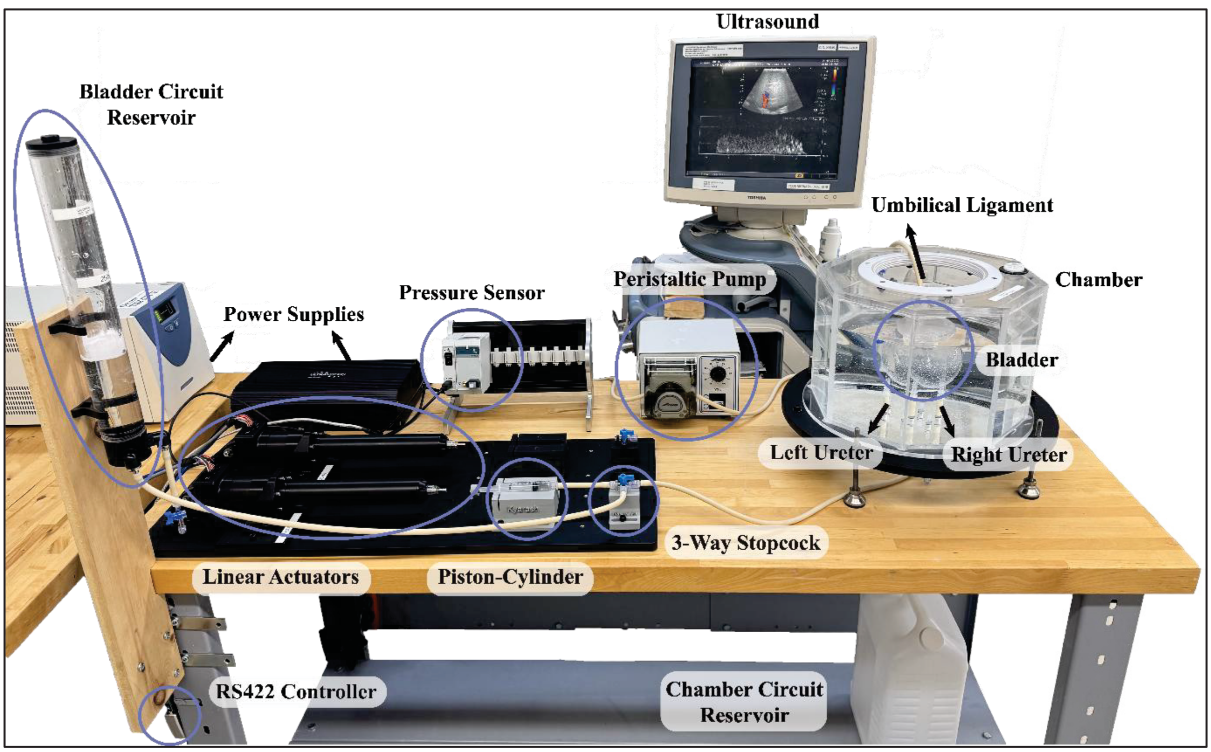

Figure 2.9 Complete bladder flow simulator showing linear actuators with syringes, pressure sensor, peristaltic pump, reservoirs, ultrasound unit, and the chamber with the bladder phantom

The working fluid was chosen to match *in vivo* ureteral jet characteristics at the UVJ via the Reynolds number $\mathrm{Re} = \mathrm{UD}/\nu$ and the Womersley number $\mathrm{Wo} = (\mathrm{D}/2)\sqrt{\omega/\nu}$. Using adult phase Doppler data for peak jet speed $\mathrm{U} \approx 0.4 - 0.8\ \mathrm{m/s}$ and cycle time $4 - 6$ s together with a UVJ diameter scale $\mathrm{D} \approx 3$ mm, we targeted $\mathrm{Re} \sim 400 - 700$ and $\mathrm{Wo} \sim 1.0 - 1.4$. The fluid properties will be discussed in more detail in Chapters 3 and 4.

2.4.1 Division of fluid circuits

The bladder fluid circuit mainly includes the actuators and syringes that drive the ureteral jet pulses, the bladder phantom, and a reservoir. The reservoir is connected to the actuator mechanisms to provide a fluid recharge supply to the syringes. To initially fill the bladder, fluid is drawn from the reservoir and delivered through the ureteral inlets using the actuators until the desired volume is reached. Draining is achieved through a dedicated urethral outlet equipped with a valve, which can be opened to allow controlled emptying of the bladder between experiments or for resetting baseline conditions. A peristaltic pump (CUBE-L400S Anko) is also integrated in the bladder fluid circuit for faster initial filling and draining.

The chamber fluid circuit forms a fluid loop independent from and surrounding the bladder and includes the octagonal chamber, a reservoir, and a pump. The chamber is normally filled with the same fluid as the bladder fluid circuit to optimize optical conditions for PIV. Filling the chamber is done through one of its inlet ports, by drawing fluid from a separate reservoir with the peristaltic pump, until the bladder is fully submerged. Drainage is accomplished through an outlet port at the base, allowing fluid to be removed either by gravity or using the pump.

2.5 Intravesical Pressure–Volume Response

The intravesical pressure was monitored using fiber-optic pressure catheters (FOP-LS-PT9-10 and FOP-LS-PT9-20; FISO Technologies, Québec, Canada) with an Evolution EVO-SD-5 chassis equipped with an FPI-LS-10 high-speed single-channel signal conditioner. The PT9-10 catheter consisted of a 307-µm tip with a 20-cm polyamide lead, followed by a one-meter nylon cable with an external diameter of 0.9 mm. The PT9-20 catheter is similar, but is extended by an additional nine-meter PVC cable with an outer diameter of 3 mm, enabling greater flexibility in experimental setups. Both probes incorporated Smart-Chip memory for calibration and had a working range of ±300 mmHg. Each catheter was supplied with dedicated cleaning kits for the optical connector and probe surface, ensuring stable and reproducible measurements over time. Per the manufacturer, the PT9 fiber-optic sensors have a sensor accuracy of ±1 mmHg and a system accuracy of ±3 mmHg; we therefore adopt ±3 mmHg as the measurement uncertainty for the intravesical pressure data.

The signal conditioner supported sampling rates of up to 15 kHz through the analog output (≤ 5 kHz digital), with a 0–5 V analog signal. During testing, data were recorded at a sampling frequency of 250 Hz and filtered with a 30 Hz low-pass cutoff, which effectively removed high-frequency disturbances while preserving the quasi-static changes induced by volume filling. The system was zeroed using a calibration offset of –14.978 psi, so that the baseline pressure at the initial bladder volume of 256 mL corresponded to 0 mmHg.

2.5.1 Measurement Protocol

The phantom bladder was initially filled to a baseline volume of 256 mL. Incremental injections were then carried out in a stepwise fashion. The first stage involved ten consecutive 1 mL injections, increasing the volume from 256 to 266 mL. This was followed by two 5 mL injections, raising the volume to 276 mL, and finally one 10 mL injection that brought the total to 286 mL. Pressure was continuously recorded during each injection, and averages were extracted once the pressure stabilized. This procedure generated a dataset of pressure–volume (P–V) relationships across small and modest filling increments.

2.5.2 Data Processing and Stepwise Acquisition

Because syringe-driven injections introduced minor fluctuations in the pressure signal, an averaging method was employed to determine the effective pressure rise for each increment. Figure 2.10 presents a representative acquisition trace corresponding to the final 10 mL injection, which increased the bladder volume from 276 to 286 mL. The trace shows an initial stable plateau, followed by a rapid rise and pressure overshoot during filling, and then a new stable plateau once the fluid had equilibrated.

For each step, two stable time windows were selected: one immediately prior to injection and another after the injection was completed and stabilized. The average pressure within each of these two windows was calculated, and the difference between the post- and pre-injection averages defined the incremental pressure rise (ΔP). In the example shown in Figure 2.10, the pressure increased from approximately 0.106 psi to 0.189 psi, resulting in ΔP = 0.0828 psi, which corresponds to 4.28 mmHg. This averaging method was applied consistently across all injections, including 1 mL, 5 mL, and 10 mL steps, ensuring that transient fluctuations did not bias the final dataset.

In this study we report both elastance and compliance using standard definitions:

$$E = \frac{dP}{dV} \approx \frac{\Delta P}{\Delta V} \quad [\mathrm{mmHg} \cdot \mathrm{mL}^{-1}] \tag{2.7}$$

$$C = \frac{dV}{dP} = \frac{1}{E} \quad [\mathrm{mL} \cdot \mathrm{mmHg}^{-1}] \tag{2.8}$$

Stepwise E is obtained from the linear fit of ΔP versus ΔV across increments, and C is reported as its inverse.

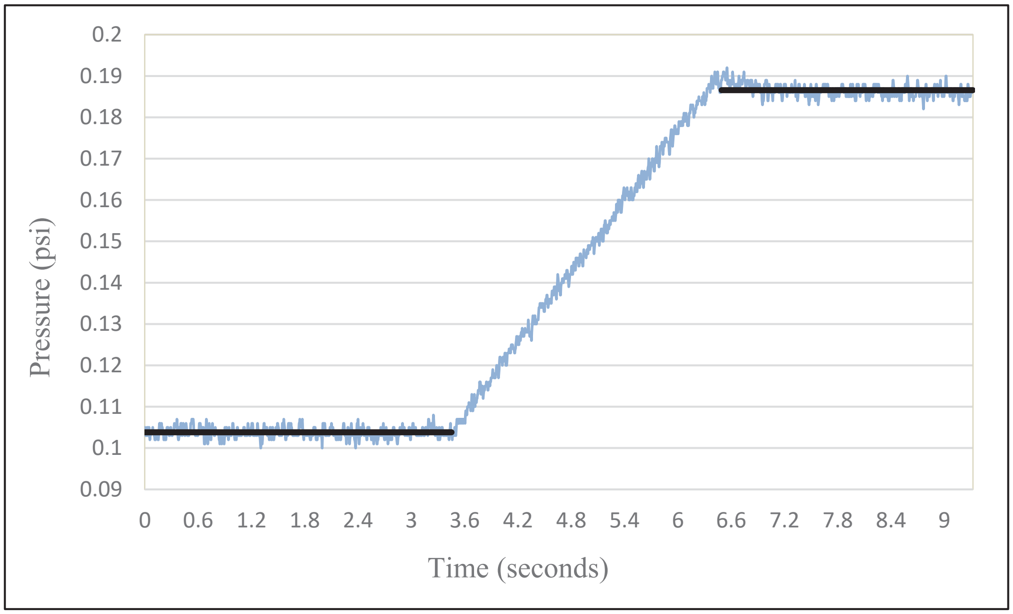

Figure 2.10 Example intravesical pressure during a 10-mL filling step: baseline ~0.10 psi, plateau ~0.18 psi (black lines represent mean levels)

2.5.3 Pressure–Volume Response

Results are illustrated in Figure 2.11. Across the full volume range of 256 to 286 mL, intravesical pressure rose in a nearly linear fashion from 0 psi (0 mmHg) to 0.256 psi (13.26 mmHg). The ten 1 mL steps produced small and consistent increases ranging from 0.42 to 0.51 mmHg/mL, with an average of 0.478 mmHg/mL. The two 5 mL injections resulted in total pressure increases of approximately 2.0 and 2.2 mmHg, equivalent to 0.40–0.44 mmHg per mL. The final 10 mL injection produced an increase of 4.28 mmHg, corresponding to 0.43 mmHg per mL. The proportionality of ΔP to ΔV across different step sizes demonstrates that the bladder phantom exhibits a nearly volume-independent elastance within this filling range.

Linear regression analysis of the P–V data yielded an elastance of 0.44 ± 0.01 mmHg/mL (R^2 = 0.999), corresponding to a compliance of 2.26 ± 0.02 mL/mmHg, or 1.66 ± 0.02 mL/cmH_2O. When the regression was restricted to only the 1 mL increments (256–266 mL), elastance increased slightly to 0.48 mmHg/mL. By contrast, the larger injection steps (5 and 10 mL) yielded slopes in the range of 0.40–0.44 mmHg/mL, indicating a subtle reduction in elastance.

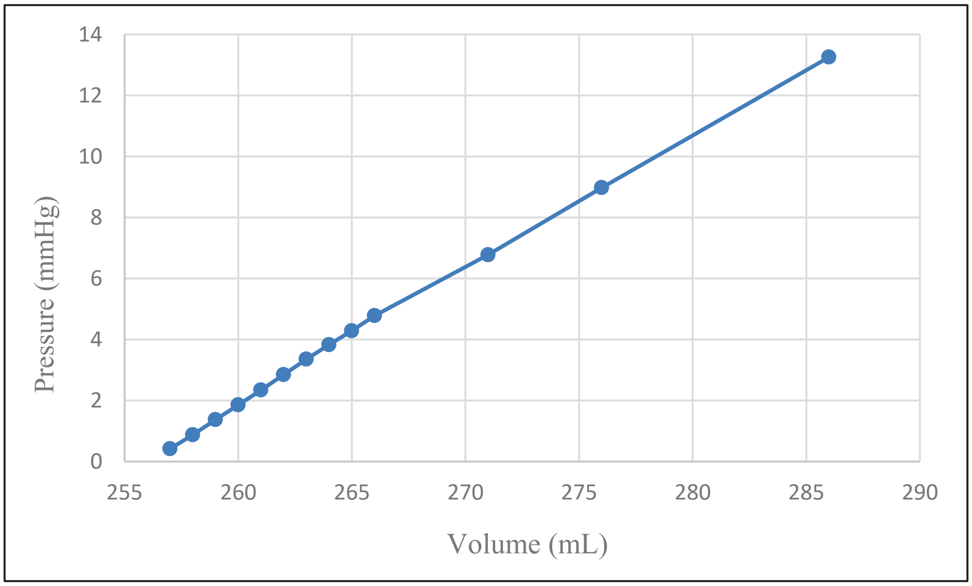

Figure 2.11 Pressure–volume relationship across the tested range demonstrating a near-linear trend

2.5.4 Interpretation and Discussion

Across the tested 256–286 mL range, intravesical pressure increases linearly with volume, with ΔP scaling closely with ΔV irrespective of step size. This indicates a nearly constant elastance over the tested range and confirms that the phantom behaves predictably under incremental fills. The global fit gives $E \approx 0.44$ mmHg·mL^{-1} ($C \approx 2.26$ mL·mmHg^{-1}), while the initial small steps are slightly stiffer (0.48 mmHg·mL^{-1}) than the later larger steps (0.40–0.44 mmHg·mL^{-1}).

The phantom behaves as a low-compliance, stiff reservoir, which is both consistent with its design and advantageous for experimental reproducibility. The global compliance of 1.66 mL/cmH_2O is lower than typical physiological values, which is expected given the phantom's passive silicone construction and the absence of detrusor adaptation. Compliance is formally defined as $\Delta V/\Delta P_{detrusor}$ during the filling phase (Gajewski et al., 2018), and the International Continence Society (ICS) emphasizes methodology and reporting rather than a single "normal" value. Many contemporary sources cite normal adult compliance as > 40 mL/cmH_2O (Yao & Simoes, 2025), while clinical guidelines for neurogenic lower urinary tract dysfunction often flag < 20 mL/cmH_2O as low compliance (Kozomara et al., 2023); older literature and some studies have used ~12.5–15 mL/cmH_2O as a severe-impairment threshold (Park, 2010). Taken together, these references consistently place our phantom's compliance below healthy ranges.

Importantly, this lower compliance does not invalidate our simulator's flow response, as will be shown in Chapter 3, likely due to the small ejection volumes and small pressure changes. Nonetheless, the phantom's compliance is lower, suggesting that the same ΔV produces a larger ΔP than *in vivo*. Consequently, our absolute pressures are higher than typical filling pressures reported clinically (often < 10–15 cmH_2O at end-fill in healthy adults), but the linear P–V behavior still allows controlled, repeatable modulation of driving pressure. We therefore use the phantom to study relative pressure-driven flow phenomena and avoid direct comparison of absolute pressures to normal physiology.

Although the measurements demonstrate strong consistency, several factors could introduce minor uncertainties. In these experiments, the sensor was fixed near the mid-height of the phantom bladder for all measurements, minimizing hydrostatic variability and ensuring that any constant bias canceled out when calculating ΔP. The low-pass filtering at 30 Hz suppressed noise but could mask rapid pressure transients; however, since the focus was on quasi-static filling, this had no effect on the measurements. Finally, syringe actuation introduced transient oscillations in the traces, but these were not included in the averaging method described above, which ensured that plateau (steady) values were used in calculating ΔP.

CHAPTER 3

ULTRASOUND DOPPLER IMAGING OF URETERIC JETS

This chapter addresses the second objective of this thesis: validating the simulator's physiological fidelity. The simulator is designed to allow the study of bladder flow so that it may be used to correlate the fluid dynamics with various urogenital conditions. The validation therefore focuses on reproducing intravesical flow, specifically the characteristics of the ureteral jets that drive the flow, for which only color and pulsed Doppler studies exist in the literature. Flow visualization and validation of the ureteral jets were performed using a Toshiba Xario ultrasound system (Toshiba Medical Systems Corporation, Otawara, Japan; 2005). The system provided a temporal resolution of up to 60 frames per second and supported multiple imaging modes including B-mode (structural imaging), color Doppler (spatiotemporal visualization of flow), and pulsed Doppler (pulsed-wave velocity profiling over time), enabling real-time visualization and quantitative assessment of ureteral jet dynamics under different simulated conditions. In this chapter, we first describe the methodology for the ultrasound repeatability and validation studies in Section 3.1 and then present the results in Section 3.2.

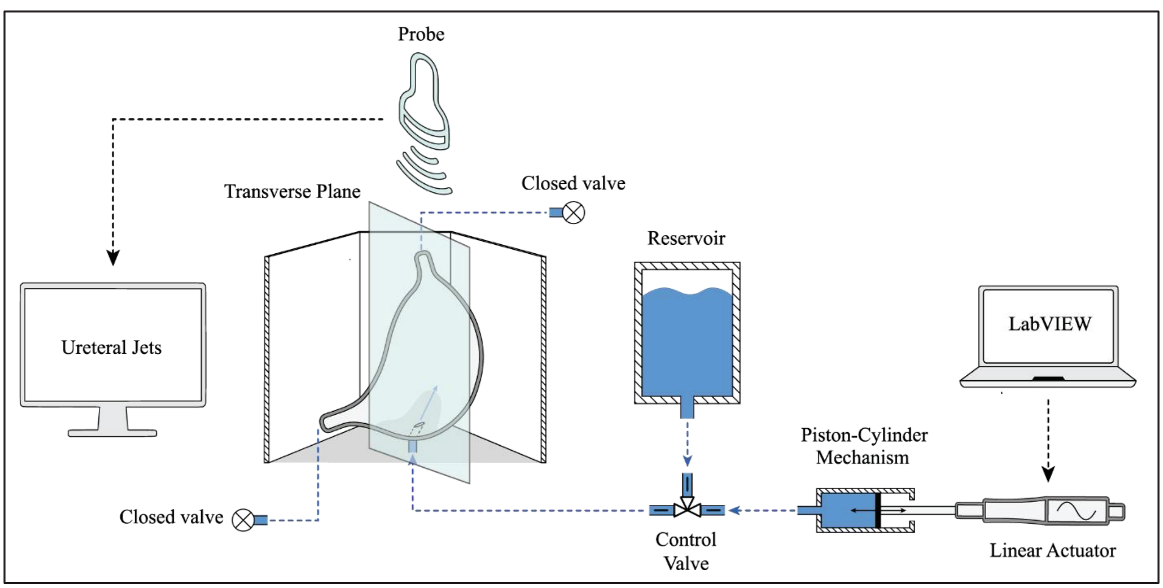

Figure 3.1 Simulator setup for ultrasound repeatability and validation studies

3.1 Ultrasound Imaging and Experimental Setup

The Xario system was used with a high-frequency linear or convex probe suitable for urological and abdominal imaging. It has an intuitive user interface and parameter presets that facilitate acquisition using different modes. Coupled with ultrasound gel, the probe was positioned above the bladder phantom, aligned with the plane containing the ureteral jets (see Figure 3.2 for probe placement). Because ultrasound measures only the velocity component aligned with the beam, the recorded speed corresponds to $v_{\text{meas}} = v_{\text{true}} \cos\theta$; thus, mesured velocities are underestimated when $\theta \neq 0°$. We therefore applied angle correction on the Xario system using the angle of the ejected ureteral jet. We note however that a spatial variation of θ exists as the jet propagates into the bladder, which implies lower accuracy for the downstream jet.

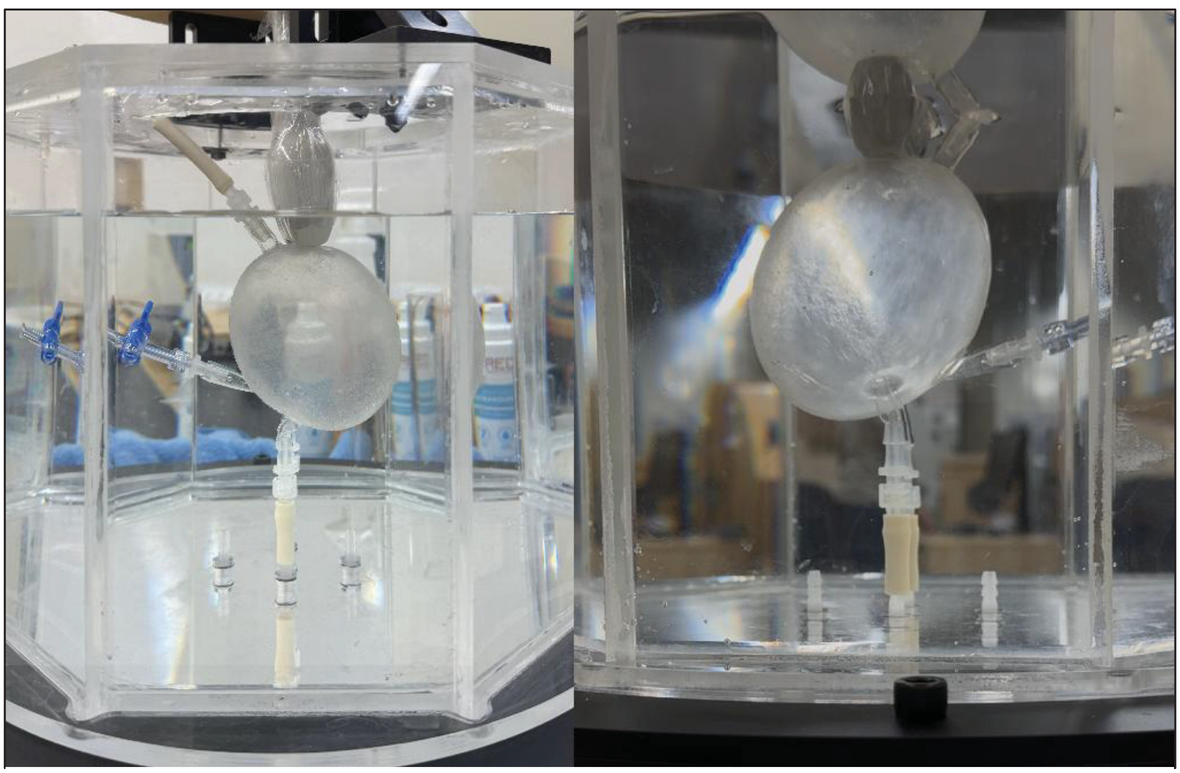

Figure 3.2 Ultrasound probe above bladder phantom, aligned with the ureteral jet plane Doppler measures the beam-aligned component, so misalignment underestimates velocity

3.1.1 Doppler Ultrasound Acquisition Parameters

Color and pulsed Doppler modes were used to visualize and quantify ureteral jet flow patterns. Color Doppler measurements confirmed the direction and general behavior of the jet, using a color velocity scale of 5.8 to 31 cm/s as indicated on the scale bars. The transducer frequency was set between 7.2 to 11.5 MHz (see example in Figure 3.3) and adjusted to optimize spatial resolution. Color-flow gain was maintained between 4.4 to 4.7 to balance noise suppression with sensitivity to low velocities. Dynamic range was set between 80 to 85 dB to enhance contrast and delineate flow against surrounding tissue. Color gain was adjusted between 40 to 47 to improve vessel and jet visualization while avoiding color bleed and overgain.

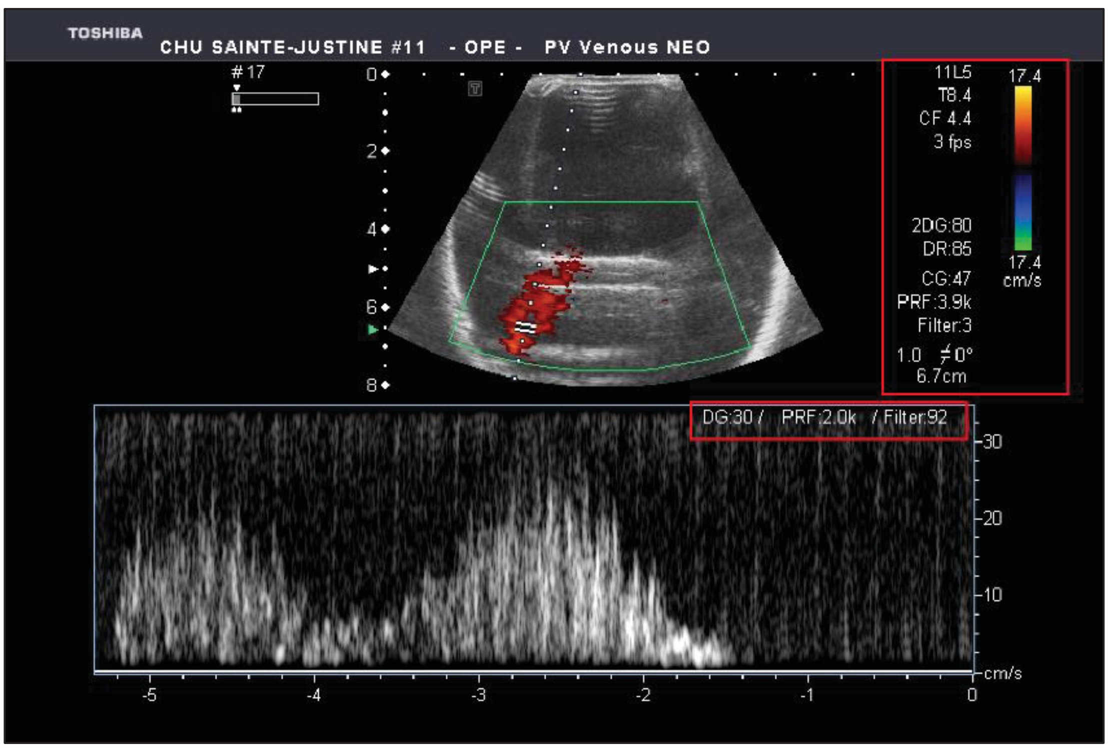

Figure 3.3 Example of ultrasound imaging parameters used for ureteral jet visualization, showing both color and pulsed Doppler

Pulsed Doppler parameters were configured to measure velocity-time profiles. Pulse repetition frequency (PRF) was adjusted from 2.0 to 5.0 kHz depending on flow velocity to avoid aliasing and accurately capture peak values. The wall filter ranged from 92 to 236 Hz to remove low-frequency noise and background motion. Sample-volume angle correction θ was set between 0° to 20°, depending on the overall jet orientation, to ensure proper alignment of the majority of the jet for velocity calculation.

These parameter ranges follow standard ultrasound practices for abdominal/urogenital applications and are consistent with guidelines on color flow gain and PRF selection, wall filters, and angle correction (Hoskins & Martin, *Diagnostic Ultrasound: Physics and Equipment*; Kremkau, *Sonography: Principles and Instruments*). During acquisition, the probe was held vertically for practicality; because the ureteral jets were inclined relative to the beam, angle correction was required to compensate for velocity underestimation. B-mode was used to ensure correct anatomical alignment before activating other modes. Velocity scales (y-axes) were chosen to match anticipated ureteral jet velocities (up to ~50 cm/s), allowing clear differentiation among monophasic, biphasic, and continuous jet patterns. All images were stored digitally and later analyzed for jet waveform shape, duration, and peak velocity to validate simulator-generated patterns against clinical studies (discussed in section 3.2).

3.1.2 Selection of Physiological and Pathological Jet Patterns

To evaluate the fidelity and versatility of the bladder simulator, we selected three clinically relevant ureteral jet patterns for replication: monophasic, biphasic, and continuous. These waveforms were chosen based on Doppler ultrasound studies that link jet morphology to specific physiological or pathological conditions.

Biphasic jets are most common in healthy adults, representing coordinated contraction and relaxation phases of the vesicoureteral junction (VUJ) (V. Y. F. Leung et al., 2002). Continuous jets are associated with abnormal conditions such as detrusor overactivity, neuromuscular dysfunction, or diuretic stimulation (Hayan et al., 2019; V. Y. F. Leung et al., 2002). Monophasic patterns are typically observed in immature ureters, such as in pediatric cases, or in transplanted ureters with limited muscular tone (V. Y. Leung et al., 2007; Wu, 2010). By replicating these distinct patterns, we aimed to validate not only the simulator's baseline functionality but also its clinical relevance for mimicking healthy and abnormal states.

3.1.3 Ureteral Jet Modes for Ultrasound Imaging

Controlled ureteral jet patterns were generated using the programmable actuation system described in Section 2.3.1. Three clinically-relevant ureteral jet waveforms were examined (biphasic, monophasic, and continuous) each programmed with peak jet velocities and durations based on available ultrasound data.

The biphasic waveform represents healthy ureteral jets with two peaks per ejection. The monophasic waveform is representative of abnormal jets with a single, prolonged peak, reflecting impaired peristaltic activity. The continuous waveform is representative of obstructive flow conditions characterized by sustained non-pulsatile discharge. These profiles were programmed into the actuator control system and executed during imaging to investigate intravesical flow patterns under each condition (Table 3.1).

Table 3.1 Summary of waveform parameters for the three jet patterns used in the experiments, including peak velocity range, duration, and defining peak characteristics

Jet Type	Velocity range (cm/s)	Duration (s)	Peaks Characteristics
Biphasic	25- 90	4	First peak ~65–75%, second peak ~85–100%, separated by troughs ~20–25%
Monophasic	20- 35	3.5	Single peak at 100%, tapering to zero at start and end
Continuous	10- 25	5	No peaks/troughs, steady flow at 100% normalized input scaled to 35 cm/s

Figure 3.4 shows representative command velocity profiles for biphasic, monophasic, and continuous jets. Each trace is plotted with its actual, case-specific duration (e.g., ~4.0 s, ~3.5 s, ~5.0 s). Because no single canonical peak velocity is prescribed clinically, peak values were adjusted run-to-run within the validated velocity range. The figure therefore only shows an example of each waveform rather than all input waveforms. Actuator commands were generated from normalized profiles via cubic-spline interpolation based on clinically reported pulsed Doppler patterns (Section 2.3). Figure 3.5 presents the corresponding syringe-piston displacements (mm) for the same cases and durations, obtained by converting ureter velocity to syringe piston velocity via the area ratio and numerically integrating over time.

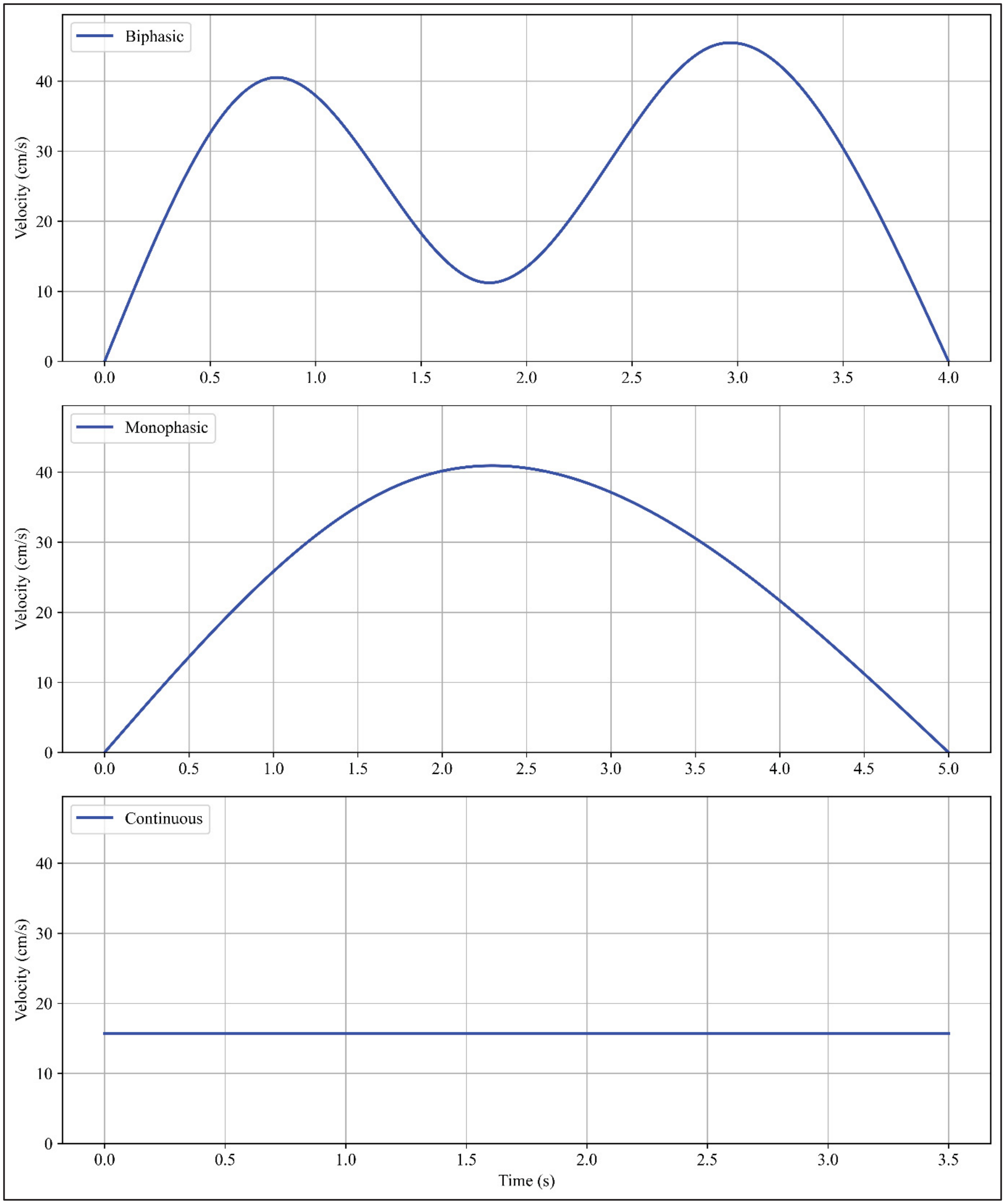

Figure 3.4 Representative command velocity profiles for biphasic, monophasic, and continuous ureteral jets

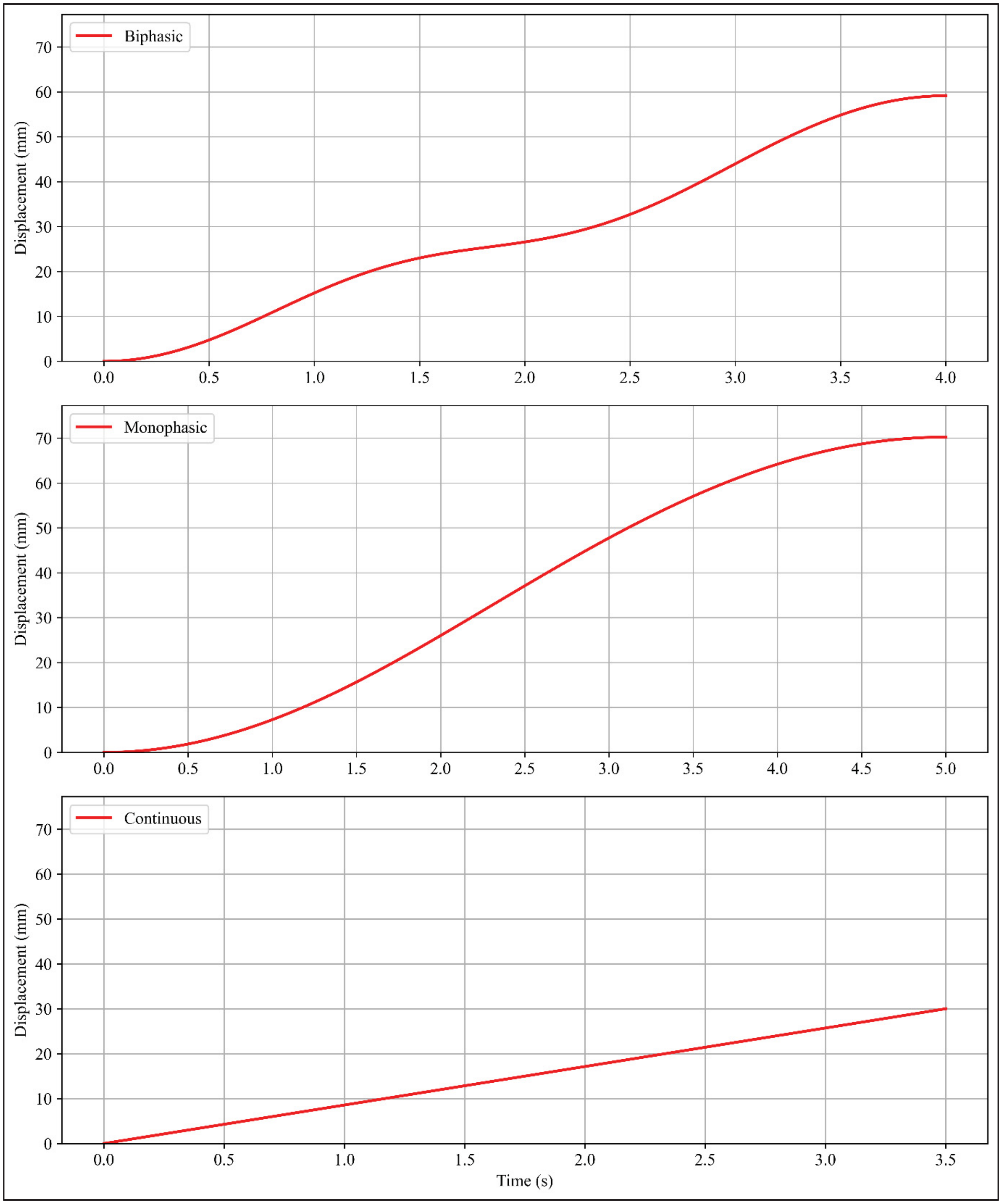

Figure 3.5 Corresponding syringe-piston displacement (mm) for the same cases and durations, obtained via ureter to syringe area-ratio conversion and numerical time-integration

3.2 Ultrasound validation results

This section reports ultrasound characterization of the ureteral jets produced by the simulator under the three programmed inflow waveforms (Section 3.1.3): biphasic, monophasic, and continuous. For each, we provide qualitative descriptions of the appearance of the jets in color Doppler as well as a quantitative summary of event onset (t_0), end (t_1), duration ($t_1 - t_0$), and peak jet velocity measured from pulsed Doppler. Jet timing was extracted directly from the exported ultrasound frames while velocities are read in cm/s on the system scale. Two working fluids were used, namely, saline and a water–glycerin mixture seeded with tracer particles. The latter working fluid is used for PIV measurements (discussed in Chapter 4), though also provides increased backscatter for ultrasound measurements.

The purpose of performing multiple programmed inflow patterns is twofold: validation and comparison. First, generating distinct jet morphologies demonstrates that the simulator is capable of reproducing different ureteral jet signatures observed *in vivo*. Second, by comparing measured durations and velocities to published reference ranges, we establish that the phantom produces quantitative physiological results and can therefore serve as a test bench for bladder flow investigations. Specifically, we compared our simulated pulsed Doppler traces directly with clinical reference images from Leung (2007). Side-by-side comparisons are presented for each programmed case, highlighting the strong phenomenological agreement between the simulator and *in vivo* ureteral jet recordings.

3.2.1 Biphasic waveforms

Qualitative appearance. The biphasic program produced two velocity maxima (P1, P2) separated by a trough. On color Doppler, a narrow, high-velocity jet extended into the bladder lumen with stable hue and minimal lateral dispersion. On pulsed Doppler, the envelope broadened modestly near each peak (increased velocity spread) without a persistent reverse-flow component (i.e., no sub-baseline signal). The optimal jet angle varied between 0° and 5° across repeated measurements (Figure 3.6).

Quantitative measurements. For the biphasic runs B1–B6 (saline) and BP (water–glycerin–tracer), the input waveform was programmed with a cycle duration of 4.00 s and target peak velocities of 20, 25, 30, 30, 35, 45, and 90 cm·s^{-1} respectively. For the saline runs B1–B6, the measured durations averaged 3.83 s (SD 0.32 s), corresponding to a mean error of −0.17 s (−4.2%) relative to the 4.00 s input. Across all cases B1–BP, the largest duration overshoot was +0.47 s (+11.6%, B1) and the largest undershoot was −0.77 s (−19.1%, BP). For the peak velocities, the smallest absolute error was 0.5 cm·s^{-1} (2.5%, B1) and the largest was −2.2 cm·s^{-1} (−7.3%, B3); all other cases remained within ±1.8 cm·s^{-1} of their respective targets. Case-by-case peak-velocity errors are reported in the last column of Table 3.2.

Table 3.2 Biphasic jet timings and velocities (Pulsed Doppler)

Case	t_0 (s)	t_1 (s)	Duration (second)	P1 (cm/s)	P2 (cm/s)	Peak (cm/s)	Error (%)
B1	-4.859	-0.394	4.465	20.5	16.3	20.5	2.5
B2	-5.223	-1.539	3.684	22.2	26.1	26.1	4.4
B3	-4.205	-0.529	3.676	27.8	19.7	27.8	7.3
B4	-4.381	-0.738	3.643	23.8	29.4	29.4	2.0
B5	-4.204	-0.563	3.641	28.8	33.7	33.7	3.7
B6	-4.661	-0.787	3.874	38.3	43.2	43.2	4.0
BP	-4.158	-0.923	3.235	71.7	87.9	87.9	2.3

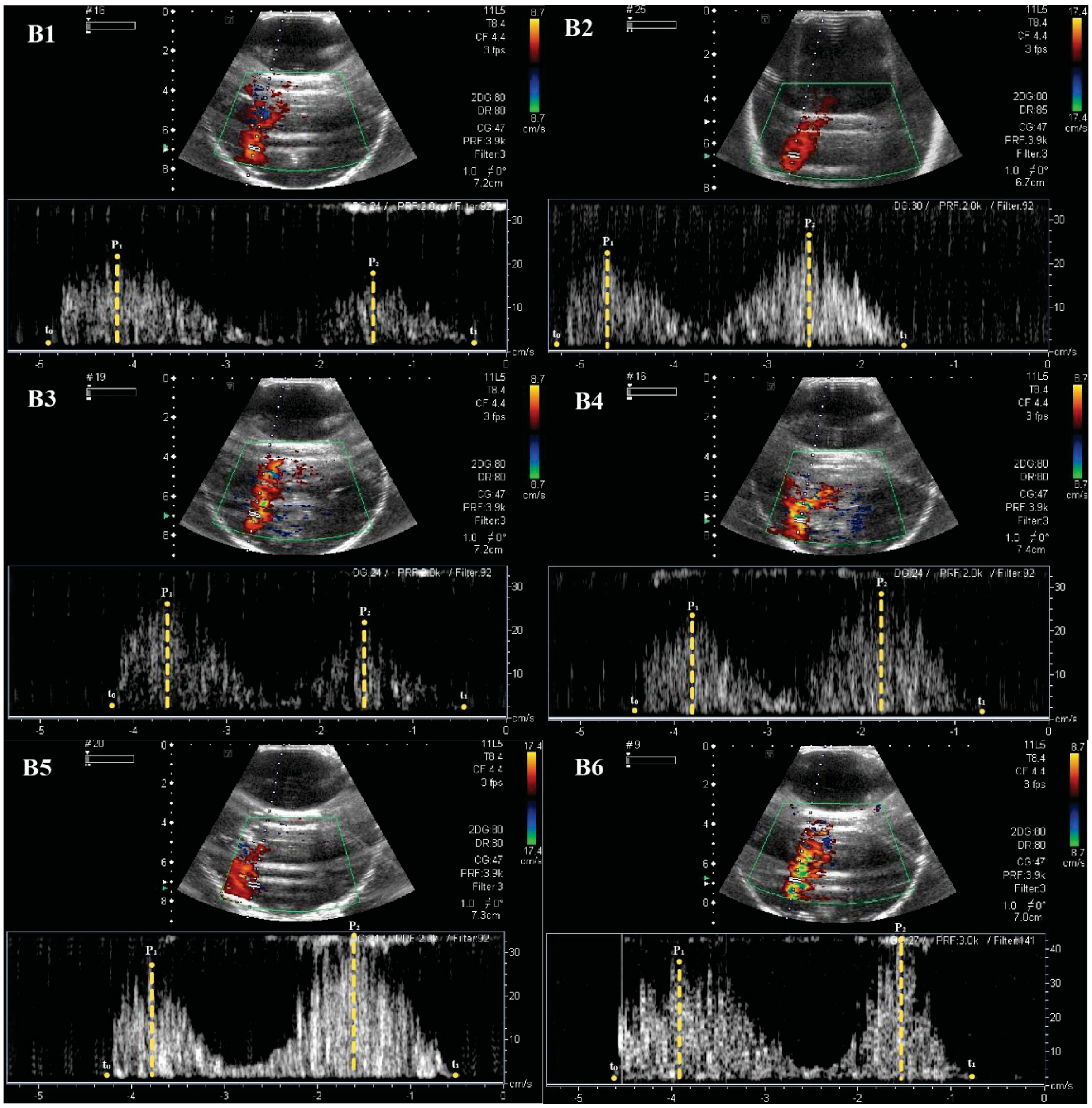

Figure 3.6 Biphasic waveforms with saline: Representative color Doppler frames with aligned spectral traces showing two distinct maxima (P1, P2) and an inter-peak trough Dashed markers indicate t_0 and t_1

The water–glycerin–tracer acquisition yields a much higher measured peak (87.9 cm/s) because particle backscatter sharpens the signal and reveals the instantaneous maxima. The overall morphology is nonetheless consistent with the saline runs, but the results are much more clear and closer to the input waveform with only a 2.3% error margin (Figure 3.7).

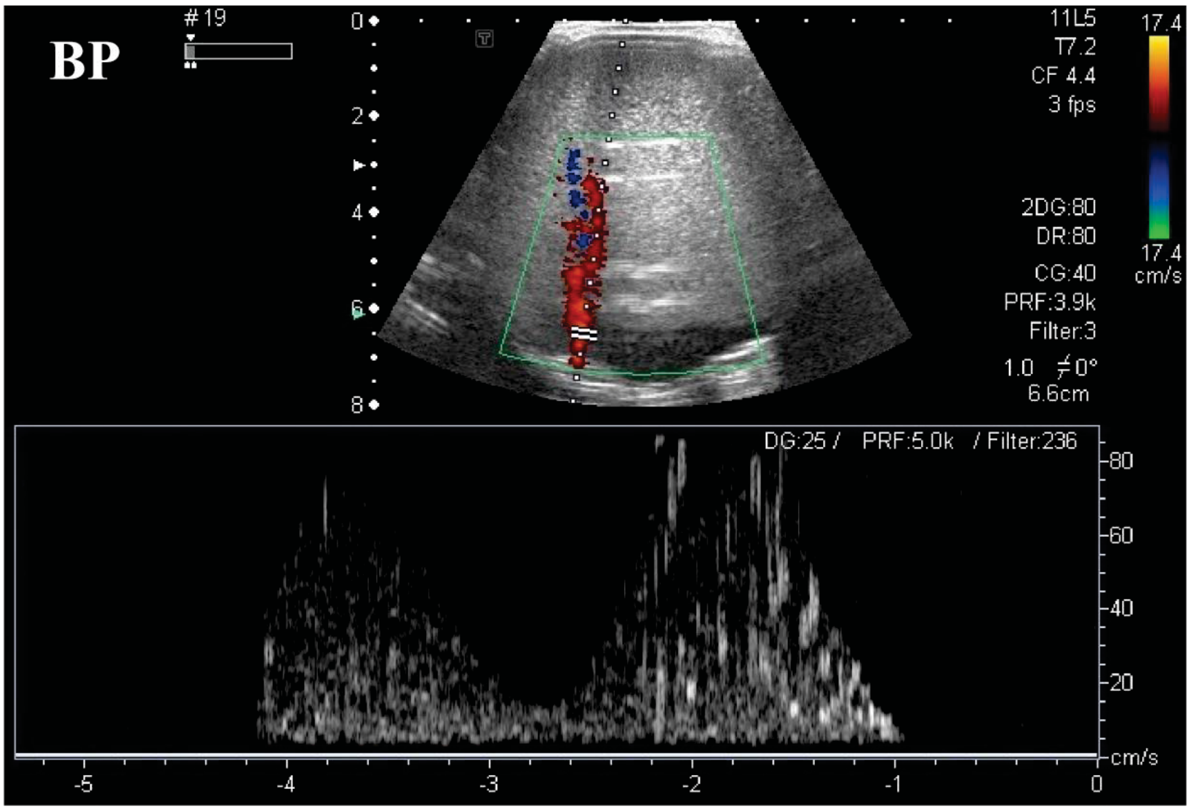

Figure 3.7 Biphasic, water–glycerin–tracer with PIV particles: Same programmed waveform with tracer seeding, sharper spectral outline reveals instantaneous peaks (higher measured maxima)

Validation with literature. Previous ultrasound studies of healthy adults report biphasic or triphasic jet morphologies with durations of ~3–5 s and velocities commonly between 20–60 cm/s (Cox et al., 1992; Burge et al., 1991). Our biphasic waveforms were generated to fall directly within this physiological envelope, and the measured output confirms that the simulator can reproduce these clinical observations. When compared side-by-side with ultrasound images from Leung (2007), the reference used to develop the baseline biphasic waveform, there is a clear agreement in envelope shape and dual-peak spacing (see Figure 3.8). This indicates that the measured output using pulsed Doppler matches closely the expected output (both qualitatively and quantitatively) from the ureteral jet actuation mechanism.

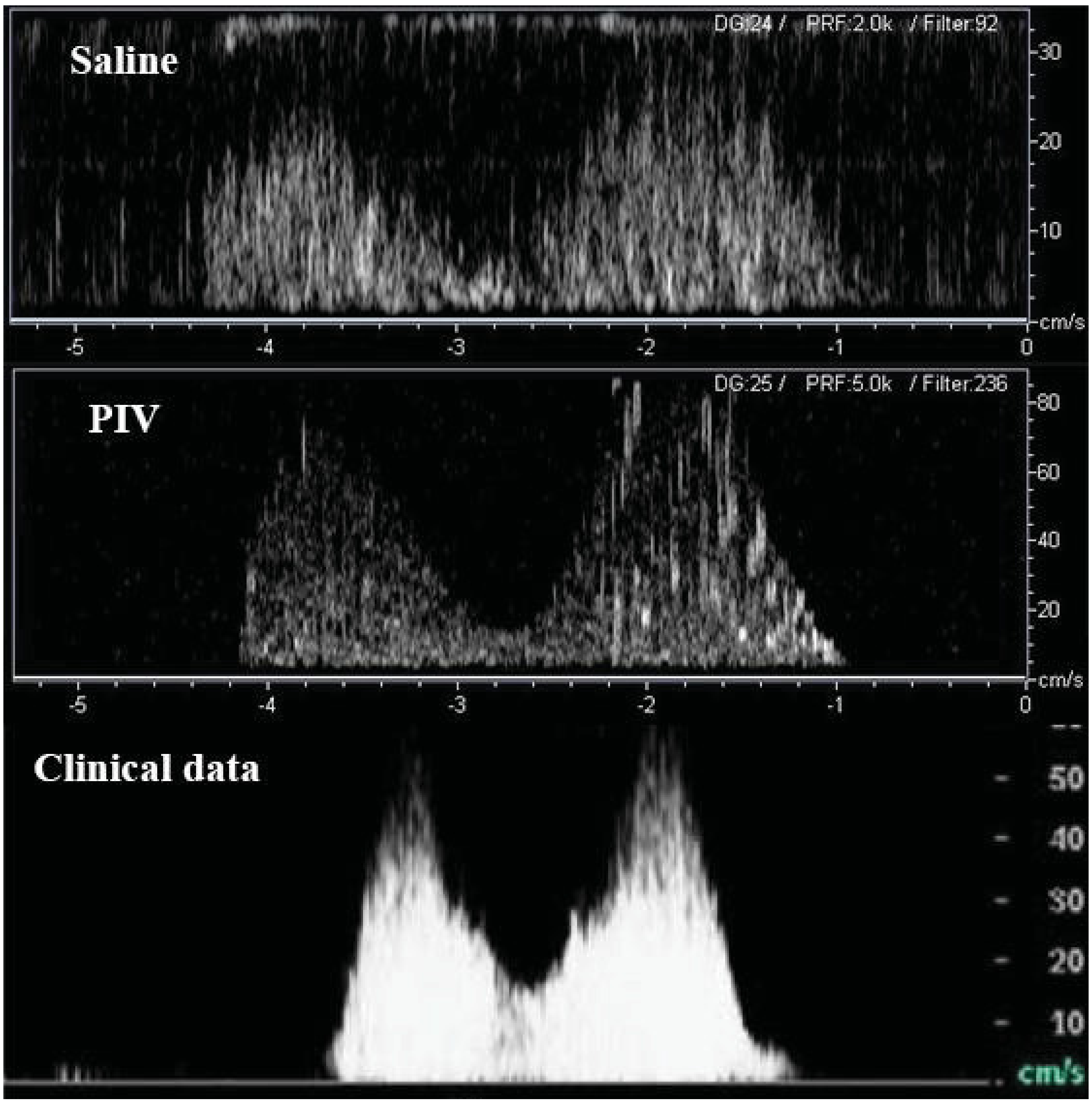

Figure 3.8 Biphasic comparison with human reference: Side by side spectral envelopes from the simulator (first and second images) and Leung (2007) (third image) highlighting close agreement in peak spacing and morphology

3.2.2 Monophasic Waveform

Qualitative appearance. The monophasic program yielded a single, compact hill in pulsed Doppler with a rapid initial ejection and slower decay. Intermittent blue-coded pixels were seen at the jet boundary (panels M1-M6 in Figure 3.9), indicating brief retrograde-directed components relative to the color map. These were small, edge-localized bursts consistent with the development of small eddies and turbulence rather than sustained reverse ureteral flow (Figure 3.9).

Quantitative measurements. For the monophasic saline runs (M1–M6), the input waveform was programmed with a 3.50 s cycle and target peak velocities of 20, 20, 25, 25, 25, and 30 $cm \cdot s^{-1}$, respectively (Table 3.3). The measured durations averaged 3.29 s (SD 0.21 s), corresponding to a mean error of −0.21 s (−6.0%) relative to the 3.50 s input. The largest duration overshoot was +0.10 s (+2.8%, M4) and the largest undershoot was −0.49 s (−14.1%, M2). For the peak velocities, the smallest absolute error was 0.1 $cm \cdot s^{-1}$ (−0.5%, M1) and the largest was −2.3 $cm \cdot s^{-1}$ (−9.2%, M3); the remaining cases stayed within ±1.5 $cm \cdot s^{-1}$ (±6%) of their targets. Case-by-case peak-velocity errors are reported in the error column of Table 3.3.

Table 3.3 Monophasic jet timings and velocities (Pulsed Doppler)

Case	t_0 (s)	t_1 (s)	Duration (s)	Peak (cm/s)	Error (%)
M1	-4.031	-0.874	3.157	19.9	0.5
M2	-3.954	-0.947	3.007	20.2	1.0
M3	-4.167	-0.982	3.185	22.7	9.2
M4	-4.308	-0.711	3.597	23.5	6.0
M5	-4.055	-0.640	3.415	26.2	4.8
M6	-3.921	-0.537	3.384	29.1	3.0

We did not acquire a monophasic run with the water–glycerin–tracer solution because that condition was not considered in the PIV study of Chapter 4. Therefore, only the saline solution and the clinical comparison are shown in this subsection.

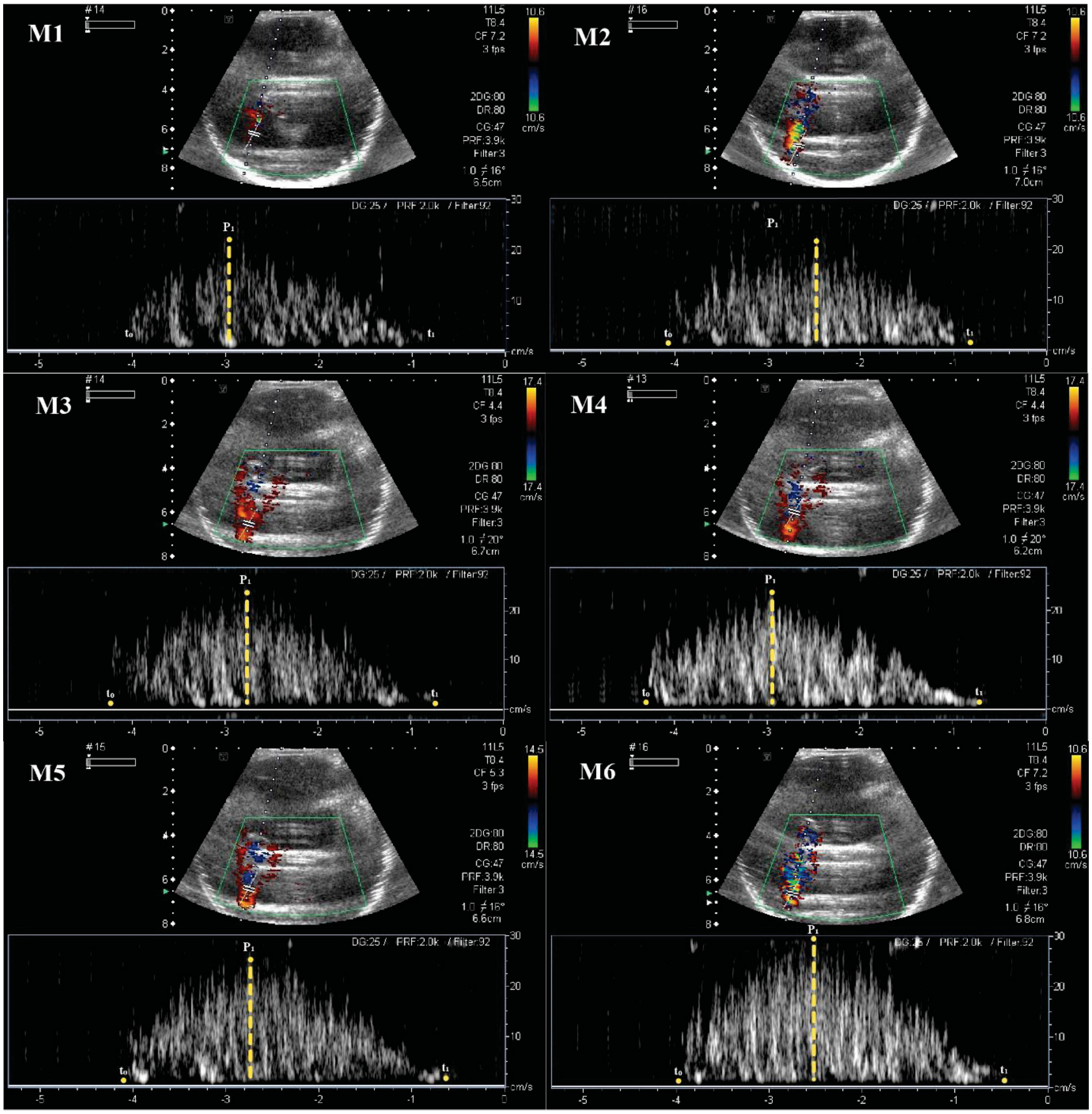

Figure 3.9 Monophasic waveform with saline: Representative frames and spectral trace with single dominant peak and annotated t_0 and t_1

Validation with literature. Monophasic events are less common in healthy patients but appear under specific hydration or bladder pressure states. Our simulator reproduced durations and velocities comparable to the lower end of reported ranges (20–35 cm/s), showing that it can mimic these less frequent but physiologically-relevant ureteral jet morphologies. Although our baseline monophasic waveform was traced from Leung (2007), the measured velocity-time signal differs modestly; see Figure 3.10. This is largely due to lower backscatter with the saline solution (no particles), which reduces the observed peak velocity. Differences in bladder compliance (which can attenuate and shift peaks) and ultrasound measurement parameters (e.g., angle correction) also contribute.

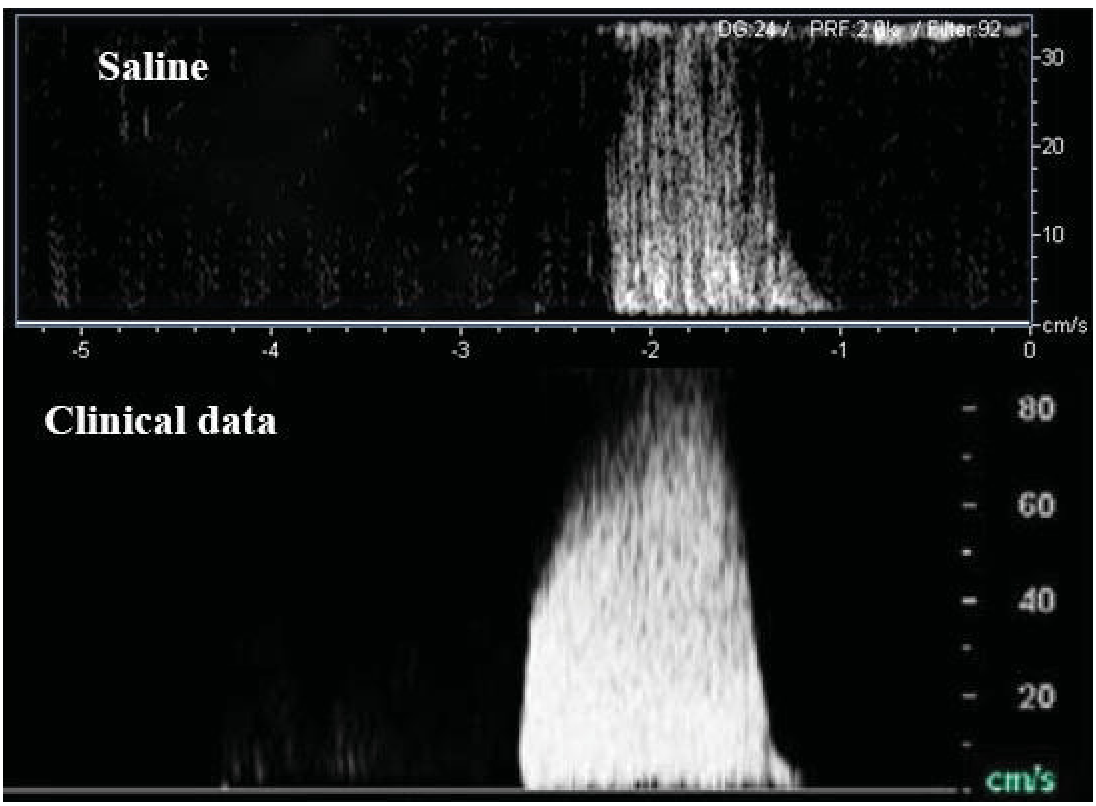

Figure 3.10 Monophasic comparison with human reference: Simulator trace (top) versus Leung (2007) (bottom) monophasic example, showing similar upstroke and decay morphology

3.2.3 Continuous Waveform

Qualitative appearance. The continuous program generated a sustained velocity plateau with gradual ramps at onset and offset. In other words, the trace rose smoothly from baseline to the plateau (no sharp corner) and returned the same way, reflecting the finite actuator acceleration and smoothing as a result of system compliance. From the pulsed Doppler trace, the plateau level was stable with low variability (Figures 3.11 and 3.12). For the water–glycerin–tracer working fluid, the plateau exhibited less noise (flatter). The saline solution produced a slightly thicker spectral band consistent with increased speckle and broader velocity dispersion.

Quantitative measurements. For the continuous runs C1–C2 (saline) and CP (water–glycerin–tracer), the waveform was programmed as a 5.00-s plateau with target mean velocities of 10, 20, and 25 $cm \cdot s^{-1}$ respectively (Table 3.4). The plateau duration was held at 5.00 s for all cases, and the measured output error ranged from +0.2 s to −0.4 s (≤ 8% error). The measured plateau velocities were 9.0, 17.1, and 23.4 $cm \cdot s^{-1}$, giving errors (measured − input) of −1.0, −2.9, and −1.6 $cm \cdot s^{-1}$, respectively. The smallest absolute velocity error was therefore 1.0 $cm \cdot s^{-1}$ (−10%, C1) and the largest was 2.9 $cm \cdot s^{-1}$ (−14.5%, C2), while with case CP a 1.6 $cm \cdot s^{-1}$ (−6.4%) undershoot was observed. Case-by-case percentage errors are reported in the error column of Table 3.4.

Table 3.4 Continuous jet (mean plateau velocity)

Case	Mean plateau velocity (cm/s)	Error (%)
C1	9.0	10.0
C2	17.1	14.5
CP	23.4	6.4

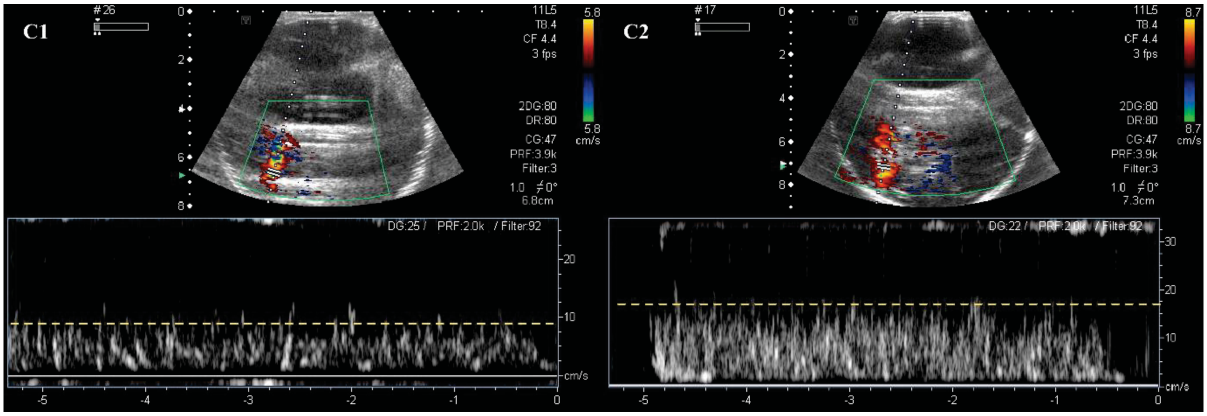

Figure 3.11 Continuous waveform with saline: Spectral plateau with annotated measurement window and stable event level

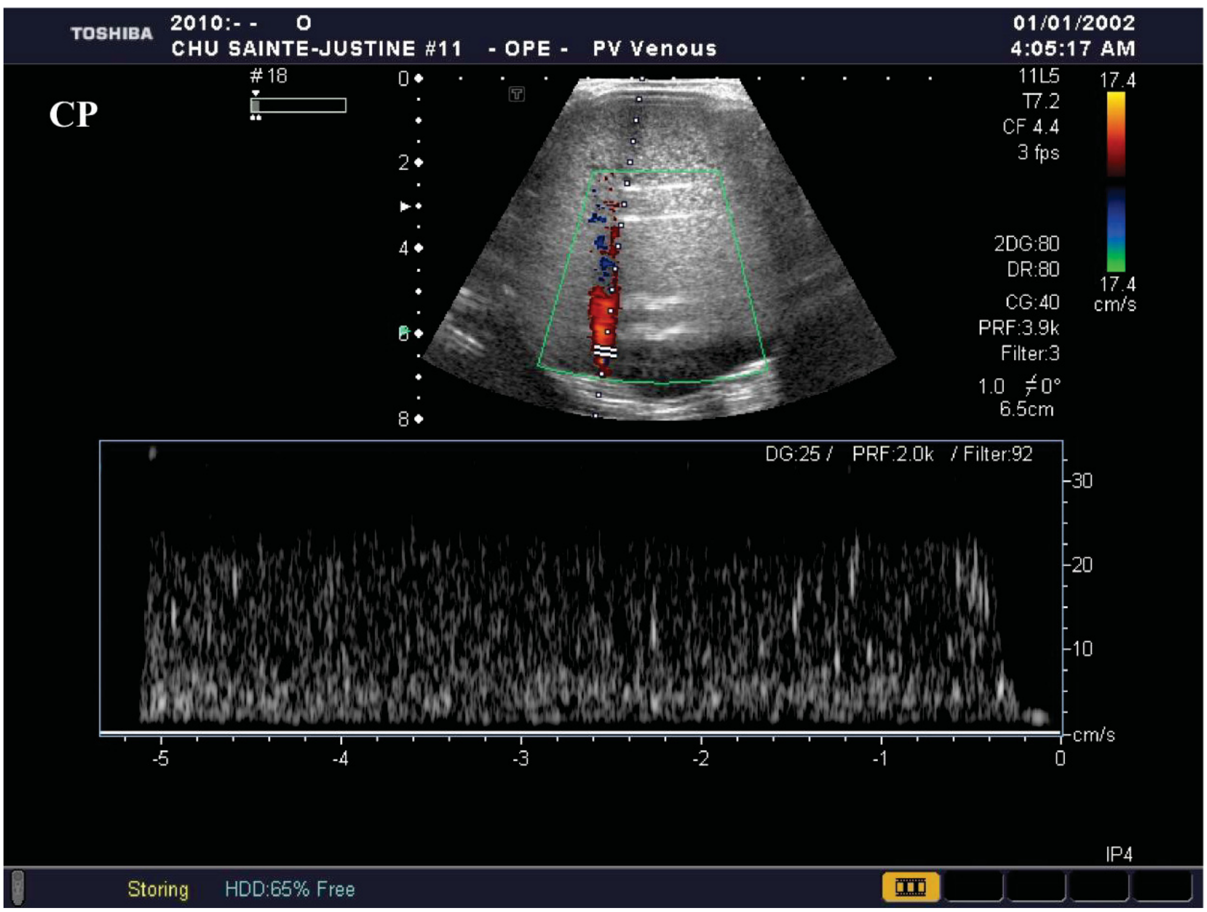

Figure 3.12 Continuous waveform with water–glycerin–tracer: Less variation in the plateau for the same programmed inflow compared with Figure 3.11

Validation with literature. A continuous signal is not common for normal kidneys but is occasionally observed in partial obstruction (Jandaghi et al., 2013). The programmed continuous output compares qualitatively and quantitatively well with the continuous trace observed by Leung (2007); see Figure 3.13.

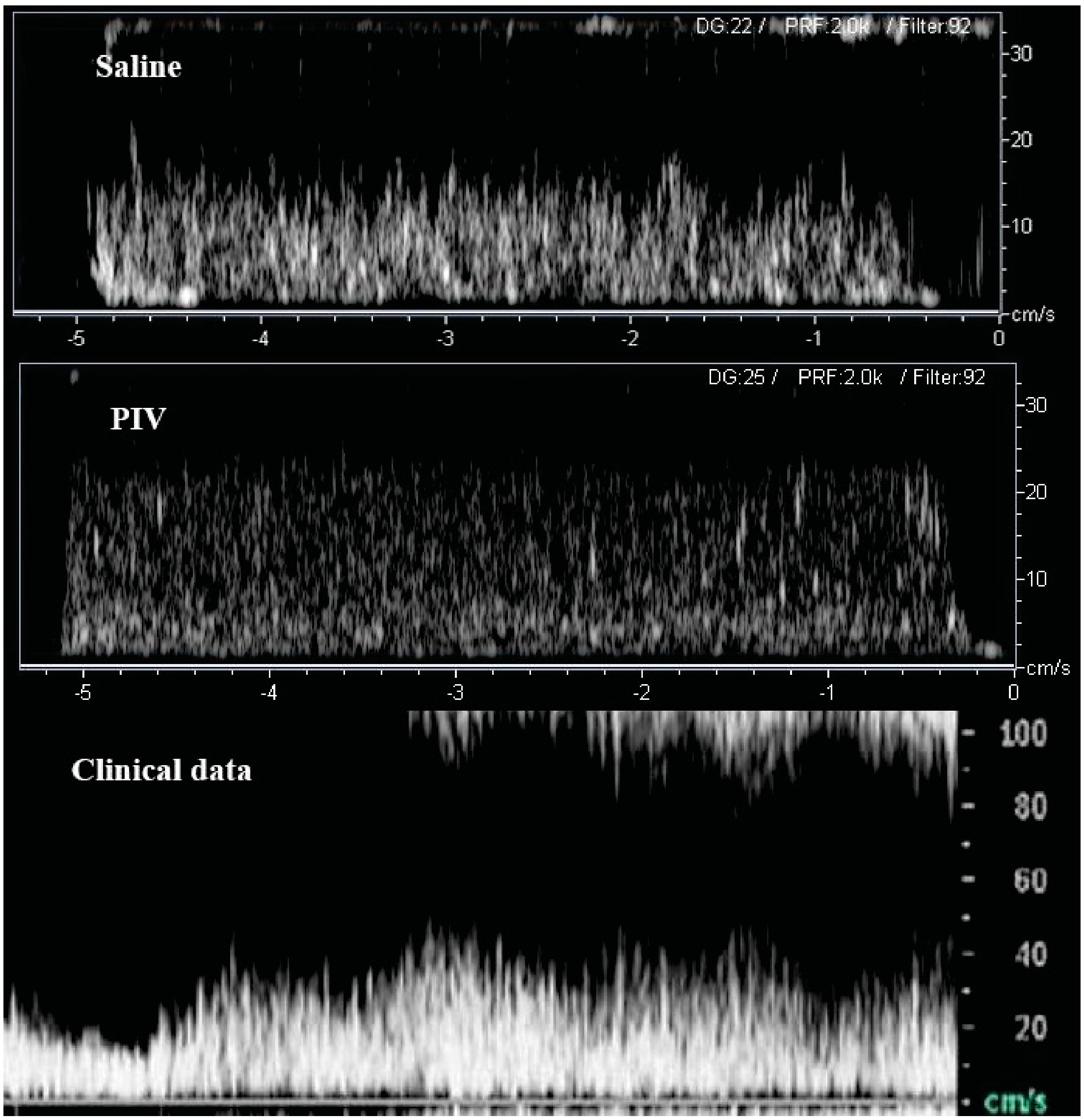

Figure 3.13 Continuous waveform comparison with human reference: Simulator plateau (first and second images) juxtaposed with Leung (2007) (third image)

Media effects (saline vs. water–glycerin–tracer)

Adding tracer particles in a water–glycerin mixture increased acoustic backscatter, which yielded sharper spectral envelopes and a quieter baseline, making peak picking more reliable. With saline, the Doppler spectrum tended to be wider (i.e., a thicker spectral envelope indicating greater apparent velocity dispersion/noise) likely from lower signal-to-noise ratio (SNR), speckle/clutter, and small angle jitter. Most importantly, the waveform morphology (single peak, biphasic, or plateau) was conserved across the two tested media.

3.2.4 Overall conclusion from ultrasound characterization

Taken together, the programmed ureteral jet waveforms demonstrate that the programmed and measured simulator outputs are consistent and that the simulator can successfully reproduce physiological ureteral jet patterns both qualitatively and quantitatively

Across all programmed waveforms, the simulator reproduced the prescribed durations and velocities with modest errors. For the biphasic jets (4.00-s cycles, 20–90 $cm \cdot s^{-1}$ peaks), the mean duration error was −0.17 s relative to the input, with extremes of +0.47 and −0.77 s, and peak-velocity errors between +0.5 and −2.2 $cm \cdot s^{-1}$ (≤ 8%). For the monophasic jets (3.50-s cycles, 20–30 $cm \cdot s^{-1}$ peaks), the mean duration error was −0.21 s, bounded by +0.10 and −0.49 s, and peak-velocity errors ranged from −2.3 to +1.2 $cm \cdot s^{-1}$ (≤ 9%). For the continuous jets (5.00-s plateaus, 10–25 $cm \cdot s^{-1}$ means), the plateau duration matched the programmed 5.00 s, and mean-velocity errors lay between −1.0 and −2.9 $cm \cdot s^{-1}$ (6–15%). Overall, duration errors stayed within about 0.8 s and velocity errors within about 3 $cm \cdot s^{-1}$ of the programmed values, indicating that the measured outputs match the expected simulator outputs closely. Direct side-by-side comparisons with *in vivo* traces from Leung (2007) showed good morphological agreement for all waveforms.

CHAPTER 4

PARTICLE IMAGE VELOCIMETRY OF INTERNAL BLADDER FLOW

This chapter addresses the third objective of this thesis, namely, to demonstrate the value of the bladder flow dynamics for diagnosis using a hypothetical test case or a mock study representing the progression of a urogenital condition. The flow fields are therefore acquired using particle image velocimetry (PIV) in the bladder flow simulator for three different waveforms representing the progression of a condition from a normal state (biphasic ureteral jet) to an abnormal state (continuous ureteral jet) with a hypothetical transitional case in between. The chapter begins with a discussion of the methodology used for PIV measurements in Section 4.1. In Section 4.2, the experimental parameters for each of the three waveforms are summarized and the post-processing methods to analyze the flow fields are presented. The results for each waveform, from biphasic to continuous ureteral jets, are presented and discussed in Sections 4.3 to 4.5. A comparison of the viscous energy dissipation between cases, a candidate indicator for diagnosis, is then presented in Section 4.6.

4.1 Particle image velocimetry

Particle image velocimetry (PIV) is an optical, non-invasive technique widely used to obtain velocity field measurements to study fluid flows. It is based on seeding the flow with tracer particles that are selected to faithfully follow the local fluid motion. These particles are illuminated using a laser and, in the case of double-frame PIV, two successive image frames are recorded with a high-speed camera within a short duration to capture their motion. By sequentially performing cross-correlations of small interrogation windows between the two successive images, the local mean displacement of the particles is obtained and by dividing by the time interval between the successive image frames, the velocity vector field can be reconstructed (Adrian & Westerweel, 2011). In the present study, time-resolved double-frame planar PIV was applied to characterize the internal bladder flow dynamics and to analyze the interaction of the ureteral jet with the surrounding flow.

4.1.1 Seeding particles

In PIV, precise flow measurements depend on the ability of tracer particles to follow the motion of the fluid without significant lag. When properly chosen, these particles move nearly in the same way as a fluid element, allowing their measured velocities to be interpreted as local fluid velocities with minimal error (Adrian & Westerweel, 2011).

For this study, solid polyamide (nylon) particles (PSP-50, Dantec Dynamics, Skovlunde, Denmark) with a nominal diameter of 50 µm (±20 µm) were used. These particles are slightly non-spherical but generally considered sufficiently uniform for flow visualization applications. With a density close to 1030 kg/m^3 and a refractive index around 1.5, they are well-suited for water-based flows, providing strong light scattering when illuminated by the laser sheet. Given the particle size relative to the laser wavelength (450 ± 20 nm), they fall into the Mie scattering regime, which ensures high signal intensity even in side-view imaging setups (Raffel et al., 2018) as performed in this work.

A key advantage of using polyamide particles is their small density mismatch with the working fluid. For a 40 wt% glycerol–water mixture at 20°C, the fluid properties are approximately $\rho \approx 1.10\ g\ cm^{-3}$ and $\mu \approx 3.7$ mPa·s (from standard density tables and the Segur–Oberstar viscosity data). Comparing with the polyamide tracers we find a relative density difference of 6–7%, which minimizes slip and settling during imaging (Segur & Oberstar, 1951). This near-neutral buoyancy ensures a rapid response to changes in flow direction and velocity. The particle response (relaxation) time was estimated using the Stokes-drag formula for small Reynolds number spheres,

$$\tau_p = \frac{\rho_p\, d_p^2}{18\,\mu} \tag{4.1}$$

with $\rho_p = 1030\ kg\ m^{-3}$ (polyamide), $\mu = 3.7 \times 10^{-3}$ Pa s (40 wt% glycerol–water at 20 °C), and particle diameters $d_p = 20 - 50\ \mu m$. This gives a response time of $\tau_p \approx 6 \times 10^{-6}$ to 3.9×10^{-5} s. For the fastest portion of the flow (the ureteral jet) we define the flow timescale as $\tau_f = D/U$, and taking the ureter diameter as $D = 3.5\ mm$ and the peak jet speed as $U = 0.6 - 1.0$ ms^{-1} yields $\tau_f \approx 3.5 - 5.8 \times 10^{-3}$s. The Stokes number,

$$\mathrm{St} = \frac{\tau_p}{\tau_f} \tag{4.2}$$

was therefore $\mathrm{St} \approx (1–7) \times 10^{-3} \ll 1$. Because the Stokes number is much less than unity, particle inertia is negligible relative to fluid acceleration, and the tracers faithfully follow the jet dynamics (where speeds are highest), ensuring accurate velocity measurement.

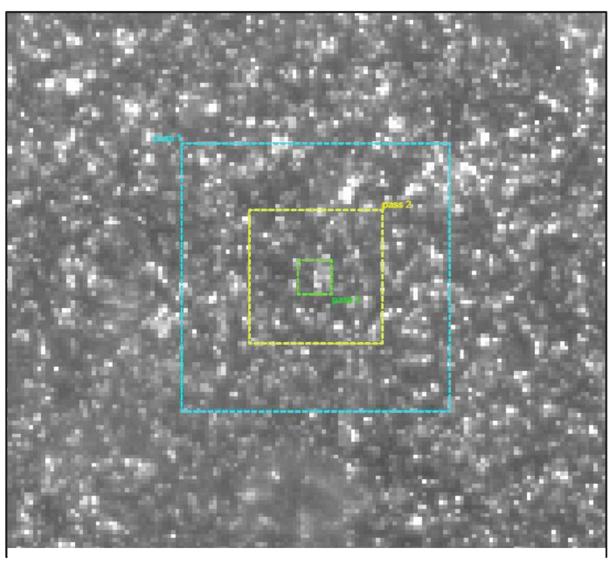

Figure 4.1 PIV raw image frame in the bladder phantom with polyamide tracers Multi-pass windows of 64→32→8 px are shown

Achieving the correct seeding concentration is also critical to ensure reliable vector field calculation. Aiming for roughly 10 to 20 particles per interrogation window (64 × 64 pixels) helps to maintain robust cross-correlation and minimize errors in vector estimation (Keane & Adrian, 1990; Raffel et al., 2018) (Figure 4.1). The overall PIV arrangement, with a laser sheet illuminating the bladder, a camera imaging the seeded flow, and interrogation window cross-correlation used to obtain velocity vectors, is summarized schematically in Figure 4.2. In practice, the seeding density was carefully adjusted before each experiment by visually inspecting sample images to ensure adequate coverage and particle separation, and consistency was maintained by using the same seeded working fluid for all experiments. This approach ensured uniform image quality across the dataset and improved the robustness of the subsequent velocity-field analysis.

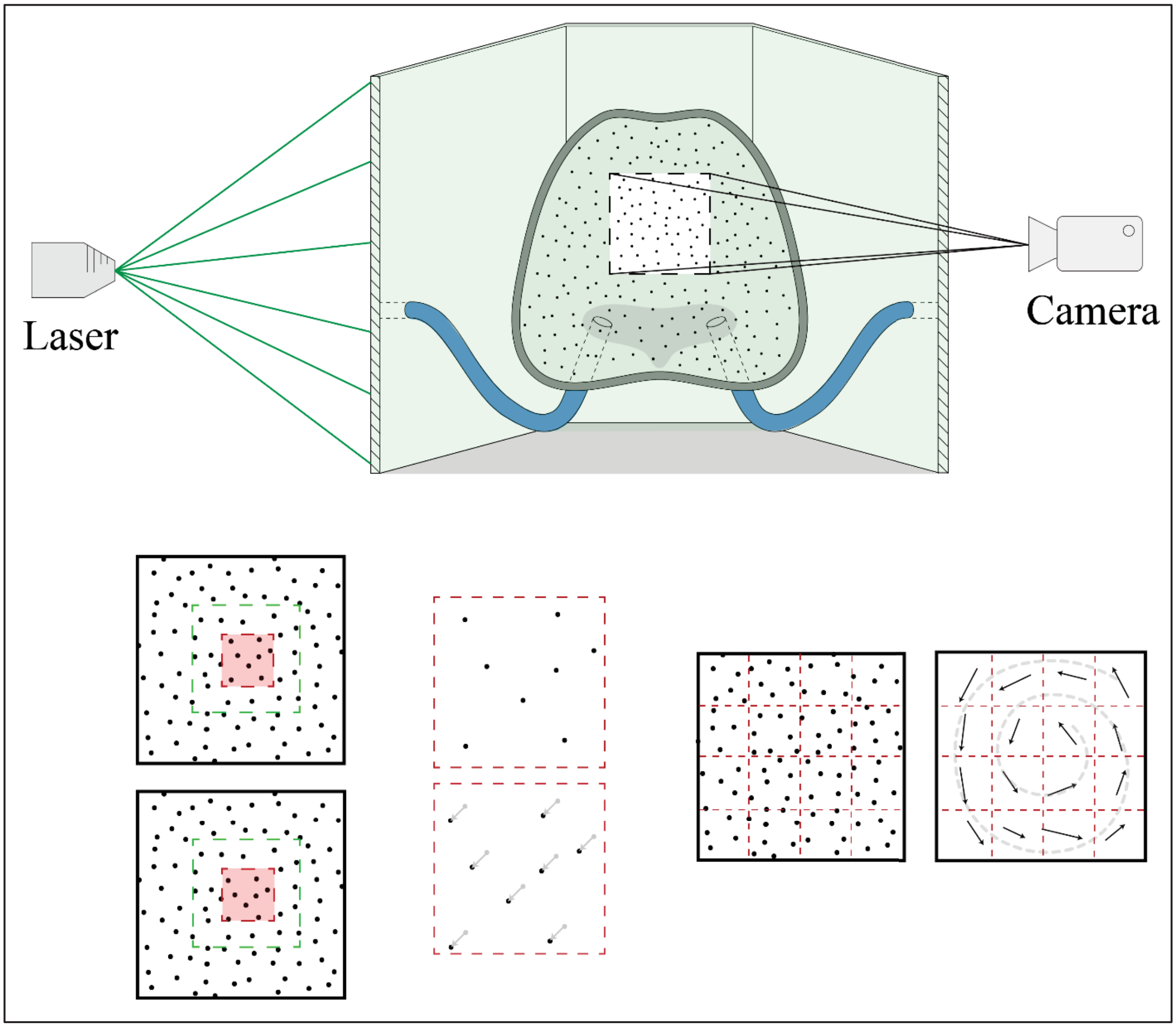

Figure 4.2 Schematic representation of the PIV setup and principle used in this study
The flow is illuminated by a laser sheet, and tracer particles are recorded in two consecutive images to determine local velocity vectors through cross-correlation

4.1.2 Field of view

The field of view (FOV) was selected to encompass the entire bladder lumen to allow for analysis of the flow structures and jet interactions within the entire bladder cross-section. We used a transverse plane capturing both ureteral inflows and the bladder dome (Figure 4.3).

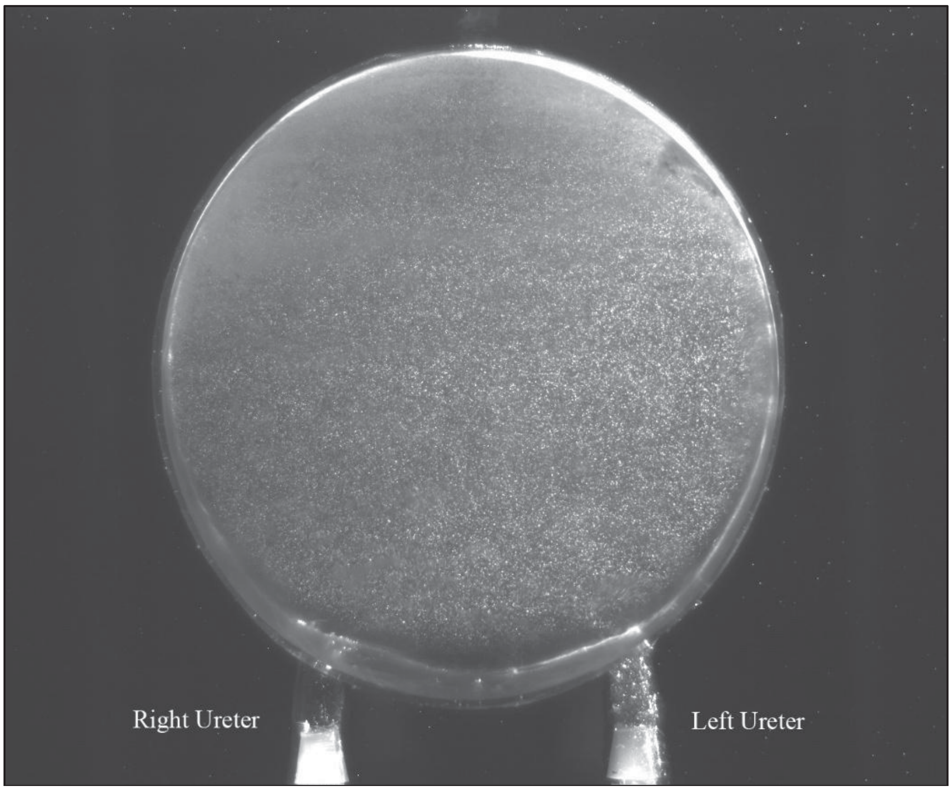

Figure 4.3 Raw PIV image showing the field of view of the bladder model Both ureteral inlets are visible, labeled as "Right Ureter" and "Left Ureter" allowing detailed analysis of jet entry and flow recirculation

Calibration was performed using a reference ruler placed inside the tank, corresponding to a physical length of 80 mm and a measured pixel length of approximately 853 px. This yielded a spatial scale of roughly 0.0938 mm/px, which was used to convert particle displacements from pixels to physical units (Figure 4.4).

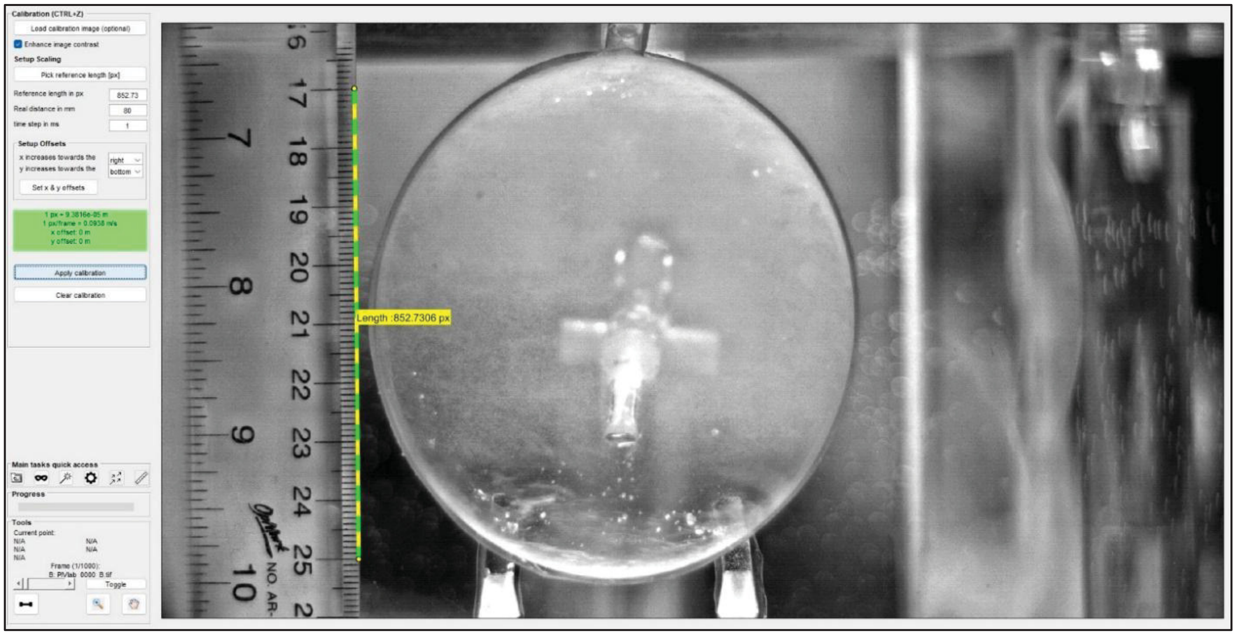

Figure 4.4 Calibration image using an in-tank ruler for spatial scaling, enabling conversion from pixel displacement to physical units (mm)

The overall FOV dimensions were approximately 19.19 cm in width and 10.79 cm in height, covering the full extent of the acrylic tank and silicone bladder model. Within this FOV, a region of interest (ROI) measuring approximately 9.07 cm in width and 9.36 cm in height was defined to restrict the domain specifically to the bladder cavity. The measurement plane and camera were carefully aligned (perpendicularity) to minimize optical distortion (i.e., all particles in focus in the measurement plane).

The single central imaging plane was selected because it captures the dominant physics of interest—ureteral jet impingement, near-orifice shear-layer development, and midline recirculation—governing momentum transfer and mixing in the bladder. This choice also reflects the scope of the present study, which is to study the dominant fluid dynamics features of the intravesical flow. Finally, this is the same plane routinely used in ultrasound to visualize ureteral jets, enabling direct qualitative comparison between the PIV results and ultrasound observations.

Figure 4.3 also illustrates two practical limitations we managed during PIV. First, particles adhered to the silicone wall over time. To mitigate this phenomenon, we cleaned and rinsed the phantom before each series of realizations. Moreover, we masked a 2–3 px circular layer offset from the bladder wall during processing to exclude nonphysical vectors. Second, the bladder base shows slightly fewer tracers because the small density mismatch implies that the particles eventually rise to the upper portion of the bladder. Our measurement protocol therefore included a homogenization step (a gentle recirculation of 30–60 s), a settling time for residual motion to cease (1 min), and acquisition within 2 min to limit segregation. The process was repeated if the mid-field intensity histogram drifted by more than 5% from a baseline measurement.

4.1.3 Laser and recording parameters

The particles in the bladder phantom were illuminated using a pulsed laser system (Optolution LD-PS, 5 W), which generated a thin and uniform laser sheet intersecting the ureteral jets. The laser was operated at a pulse length of 75 μs and a pulse distance (inter-frame delay) of 500 μs. These parameters were chosen to provide strong illumination while minimizing unwanted reflections and scattering inside the transparent bladder model.

Images were recorded using a high-speed Optronis Cyclone 2 2000 M camera equipped with a 450-nm band-pass filter, which effectively suppressed background light and enhanced the visibility of scattered light from the tracer particles. The frame rate was 250 Hz (Δt = 4 ms), chosen to resolve the jet's unsteadiness while keeping particle displacements in the optimal quarter-window range for cross-correlation.

For each run, between 650 and 950 images were acquired, corresponding to approximately 2.5 to 4 seconds of continuous measurement, depending on the duration of each ureteral jet event. The chosen pulse distance of 500 μs provided an appropriate compromise between spatial resolution and sufficient particle displacement, ensuring robust cross-correlation analysis to compute the velocity fields.

Image acquisition and synchronization were controlled using PIVlab (v3.06), a MATLAB-based open-source PIV acquisition and processing toolbox (Thielicke & Stamhuis, 2014, 2021). This software facilitated both the timing control between the camera and laser, image pre-processing, and vector field calculation. The use of PIVlab allowed for rapid real-time monitoring of image quality, live adjustment of exposure and seeding conditions, and batch processing of large image datasets (Figure 4.5).

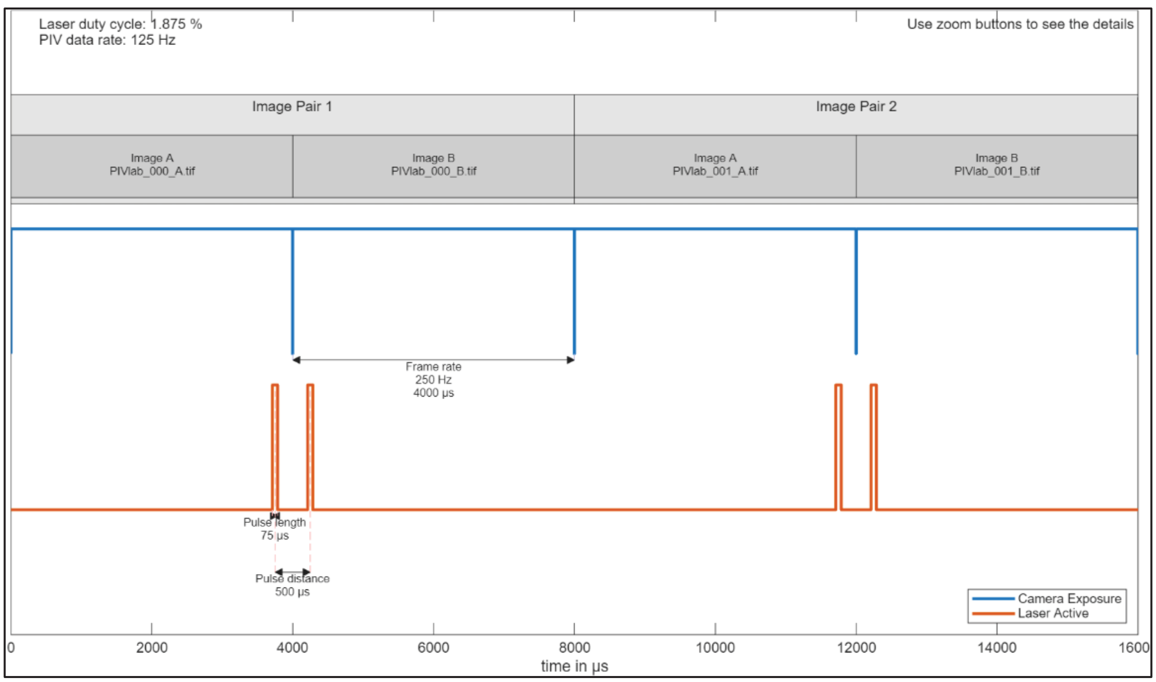

Figure 4.5 PIVlab software interface showing laser and camera synchronization settings used during image acquisition

The frame rate was set to 250 Hz with a pulse distance of 500 µs

4.1.4 Jet Waveform and Repeatability Validation

The purpose of the PIV experiments was to map the complete intravesical flow field for the first time in a configuration representative of a developing urinary condition, resolving jet penetration, vortex formation, and dome recirculation throughout the bladder volume. In addition, we performed a validation check by comparing the inflow velocity obtained from PIV at a control point just downstream of the ureteral orifice with the input inlet velocity sent to the actuator.

Three distinct ureteral jet waveforms were implemented to emulate physiological and pathological flow conditions. We simulate a progressive transition of the ureteral jet profile from biphasic to continuous as a hypothetical case used to represent the physiological degradation between a healthy ureteral jet waveform (biphasic waveform) and one representing a dysfunctional state (continuous waveform). The biphasic waveform, characterized by two velocity peaks of approximately 40 cm/s and 45 cm/s separated by a brief trough, reflects the normal peristaltic activity of a healthy ureter, where sequential contractions of the upper and lower ureteral segments produce dual pulses (Cox et al., 1992; V. Y. Leung et al., 2007). The continuous waveform, maintaining a constant plateau at 16 cm/s for 4 s, represents abnormal or detrusor-mediated flow, often associated with outlet obstruction or loss of peristaltic coordination (Jandaghi et al., 2013). The hypothetical transitional waveform was defined to exhibit an attenuated secondary peak (30 cm/s) following the primary maximum, capturing an intermediate condition that could correspond to early or partial obstruction, such as the onset of ureteral narrowing due to a developing kidney stone (Hayan et al., 2019) (Figure 4.6).

Each waveform was configured to deliver an ejection volume of 9.5 ± 0.1 mL via motor–syringe actuation. This condition allows comparison of the resulting fluid dynamics across cases under the same ejection volume, assuming a consistent fluid intake from the patient. To evaluate repeatability, four realizations were performed for each waveform. All experimental parameters (seeding density, laser pulse energy, and camera alignment) were held constant.

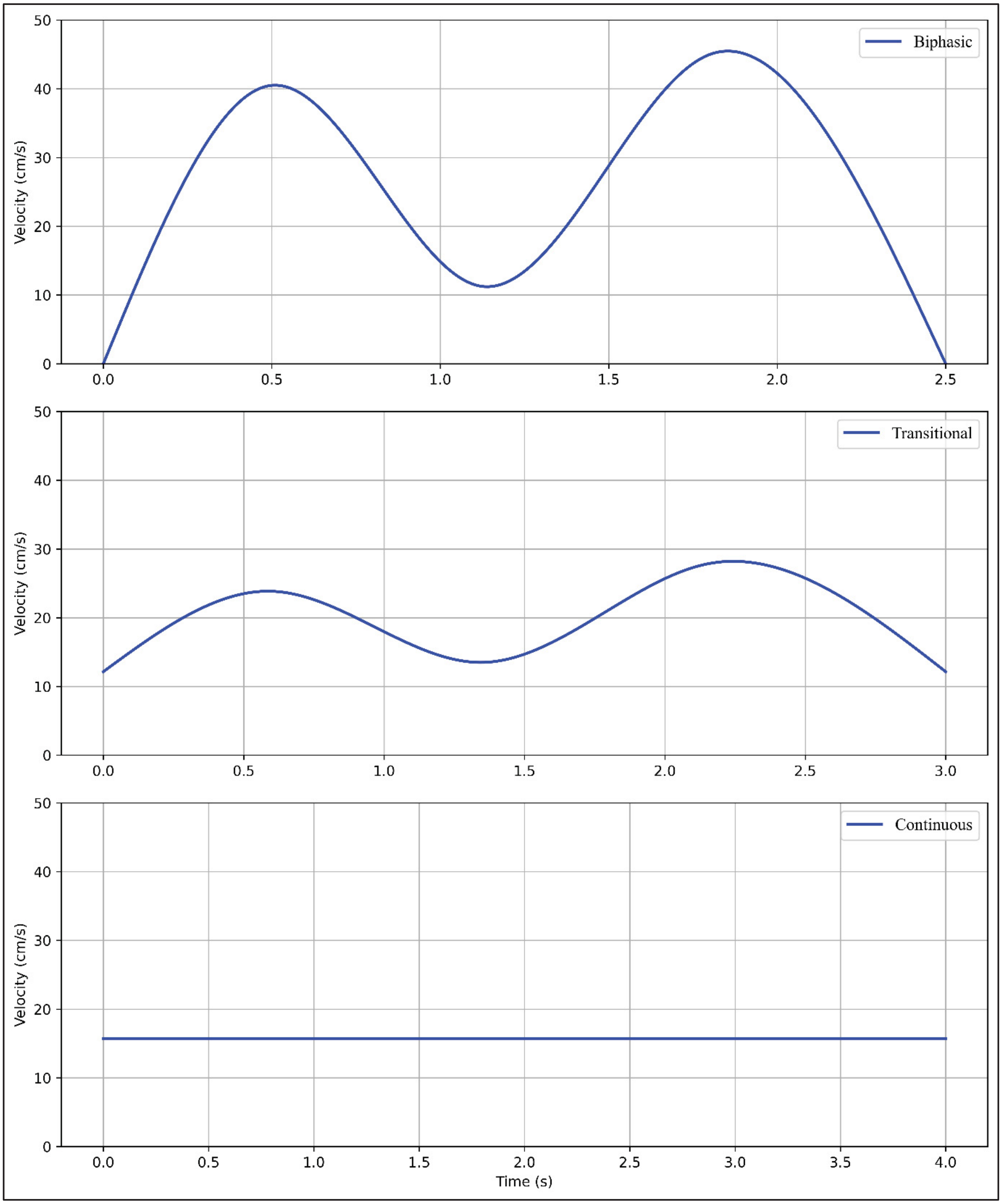

Figure 4.6 Python-generated velocity profiles including biphasic (top), transitional (middle), and continuous (bottom) waveforms
These profiles were used to program motor-syringe actuation and produce reproducible jet inputs during PIV acquisitions

4.1.5 Velocity vector calculation

The acquired images were processed using PIVlab (v3.06). Before vector calculation, a binary fixed mask was manually defined and applied across all frames to exclude areas outside the bladder model and ensure velocity calculations only within the intravesical flow region, which also improves computation time. This masking step helped prevent potential false vectors at boundaries and improved the overall signal-to-noise ratio.

Pre-processing included CLAHE (contrast-limited adaptive histogram equalization) with 64-px windows to boost local contrast in weak particle images while limiting over-enhancement; this improves particle–background separation and cross-correlation SNR (Zuiderveld, 1994). CLAHE windows were set to match the interrogation window and are therefore several particle diameters wide. Auto contrast stretching mapped intensities to the full dynamic range, sharpening particle edges for cleaner correlation peaks. Mean-intensity background subtraction removed stationary glare and illumination gradients (e.g., wall reflections), suppressing fixed patterns that cause spurious peaks and peak-locking bias (Raffel et al., 2018). Figure 4.7 shows a sample image before and after pre-processing. The background image was selected as the mean of the images of a given recording sequence.

Vector fields were calculated using a multi-pass algorithm. The first pass used an interrogation area of 64 × 64 px with 50% overlap (step size 32 px), followed by smaller window refinements of 32 × 32 px and 16 × 16 px (step sizes 16 px and 8 px, respectively). A Gaussian 2×3-point sub-pixel estimator was selected for peak localization, which is standard for high-gradient regions in PIV (Zuiderveld, 1994) and increases measurement accuracy.

Post-processing applied a local normalized-median filter (threshold = 3) to reject vectors that deviated strongly from nearby values, preserving sharp but physical gradients. A loose global standard deviation filter (8σ) was then used to catch extreme outliers. Interpolation was applied to correct deleted or spurious vectors and ensure smooth and continuous velocity fields throughout the bladder domain. The valid detection probability (VDP), a metric indicating the proportion of valid vectors relative to the total number of expected vectors, averaged around 99.6%, highlighting the robustness and quality of the images used to compute the vector fields prior to post-processing.

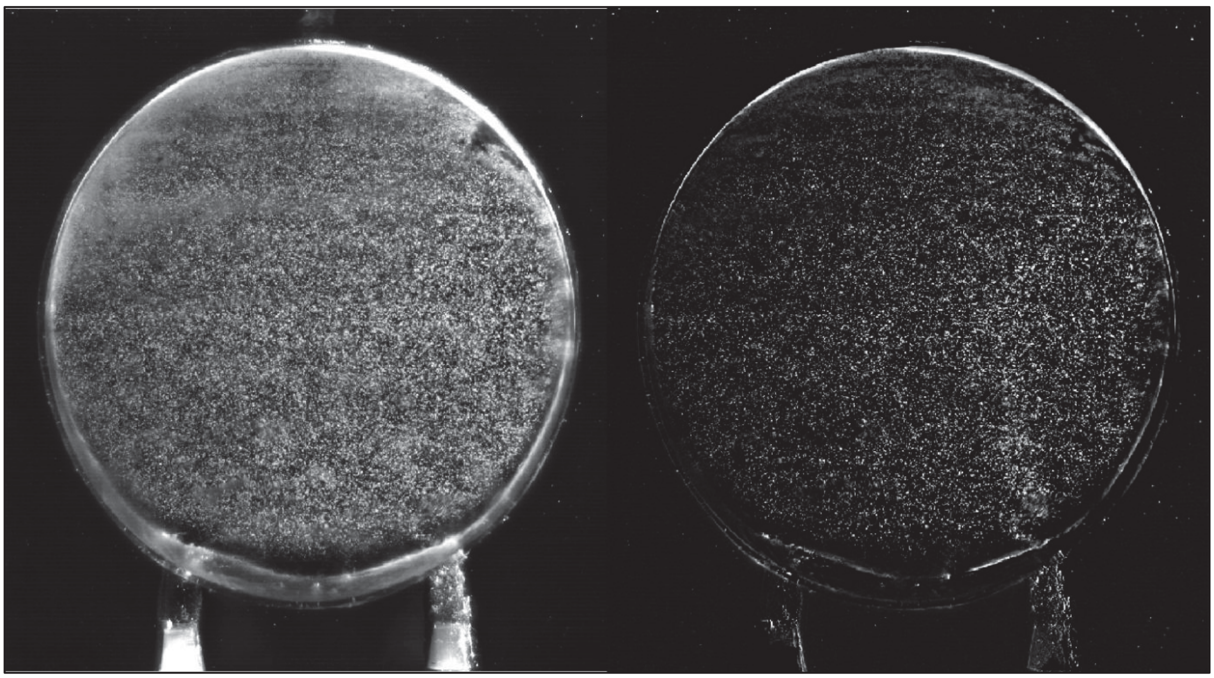

Figure 4.7 Example images before and after pre-processing, showing enhanced particle contrast and improved clarity for subsequent PIV analysis

4.1.6 Calculation of velocity gradients

The velocity gradients were calculated from the velocity fields to derive important flow quantities such as vorticity and strain rates. In particular, the in-plane vorticity component was computed using

$$\omega_z = \frac{\partial v}{\partial x} - \frac{\partial u}{\partial y} \tag{4.3}$$

where u and v denote the horizontal (x) and vertical (y) velocity components in the measurement plane, respectively.

We used a hybrid fourth-order compact (Padé) scheme with Richardson extrapolation to compute spatial derivatives because compact schemes provide spectral-like resolution and low dispersion/phase error, yielding cleaner results for shear and vorticity from noisy PIV data (Etebari & Vlachos, 2006).

The general compact finite difference scheme for the first derivative at point i can be written as:

$$\alpha f'_{i-1} + f'_i + \alpha f'_{i+1} = \frac{a}{2\Delta x}(f_{i+1} - f_{i-1}) + \frac{b}{4\Delta x}(f_{i+2} - f_{i-2}) \tag{4.4}$$

where $\alpha = \frac{1}{4}, a = \frac{3}{4}, and\ b = 0$ are scheme-specific coefficients that control accuracy and spectral resolution (Lele, 1992). In the hybrid approach, derivatives are first approximated using the compact scheme and then refined using Richardson extrapolation steps with progressively coarser resolutions (e.g., 2Δx and 4Δx). The final derivative estimate is expressed as

$$f' = \frac{A_1 f'_h + A_2 f'_{2h} + A_4 f'_{4h}}{A} \tag{4.5}$$

where f'_h, f'_{2h}, and f'_{4h} are derivatives computed with grid spacings h, $2h$, and $4h$, respectively, and $A_1 = 1024$, $A_2 = -80$, $A_4 = 1$, and $A = 945$ are noise-optimized Richardson extrapolation coefficients (Etebari & Vlachos, 2006).

Near boundaries we switched to one-sided compact stencils of 4th-order accuracy (e.g., masks, image edges). This setup mirrors prior validations of compact-difference PIV post-processing in canonical shear layers and wakes as well as internal pulsatile flows representative of cardiovascular conditions, showing accurate gradients with minimal dispersion (Etebari & Vlachos, 2006).

4.2 Experimental PIV Framework for Pulsed Jets

Time-resolved PIV at $f_s = 250\ Hz$ was used to quantify planar two-component velocity fields within the bladder phantom. The field of view (FOV) is masked to consider only the interior of the bladder. Three flow conditions are examined to represent a hypothetical test case on the simulator to deduce flow-based metrics to diagnose disease. The idea being that if a healthy individual has a biphasic pattern and one with a nonobstructive renal stone or other dysfunction displays a continuous pattern (Çelik et al., 2014; 2019), then throughout the development of the urinary condition there must exist a gradual series of transitional patterns. We therefore study three programmed ureteral jet waveforms: biphasic, transitional, and continuous. Each waveform delivered an equivalent volume of $9.5 \pm 0.1\ mL$ with durations of 2.5 s (biphasic), 3.0 s (transitional), and 4.0 s (continuous). The corresponding average inflow rates were respectively $3.80\ \pm\ 0.04\ mL/s$, $3.17\ \pm\ 0.03\ mL/s$ (transitional), and $2.38\ \pm\ 0.03\ mL/s$ (continuous). The velocity fields were then used to investigate flow behavior in terms of kinetic energy, vorticity, and energy dissipation.

For each waveform we first show the mean kinetic-energy curve from a single representative realization,

$$\mathrm{KE}(t) = \frac{1}{A}\iint \frac{1}{2}(u^2 + v^2)\,\mathrm{d}A\ [m^4\ s^{-2}] \tag{4.6}$$

and subsequently focus on three time instants (red markers labelled 1–3 on the kinetic energy curves). These characteristic time instants were selected as critical points (peaks, troughs, plateaus). For each frame, we then compute the instantaneous speed $|u| = \sqrt{u^2 + v^2}$ and the out-of-plane vorticity

$$\omega_z = \partial v / \partial x - \partial u / \partial y \tag{4.7}$$

to reveal shear-layer structure and rotational content. Local viscous dissipation per unit volume is then computed from the symmetric rate-of-strain using:

$$\Phi = \mu\left(2S_{xx}^2 + 2S_{yy}^2 + 2S_{xy}^2\right) = \left(\frac{\mu}{2}\right)\left[(2u_x)^2 + 2\left(u_y + v_x\right)^2 + \left(2v_y\right)^2\right] \tag{4.8}$$

and is shown as ved in $W\,m^{-3}$. We then integrate ved over the FOV to obtain the instantaneous viscous energy dissipation rate

$$\dot{E}_v(t) = \iint \Phi(x, y, t)\,\mathrm{d}A \tag{4.9}$$

and integrate in time to give the total viscous energy loss $E_v = \int \dot{E}_v(t)\,\mathrm{d}t$.

To reflect repeatability, the other three realizations for each case are used only to report mean ± deviation of scalar metrics at the same instants for $\dot{E}_v$. For cross-case comparability, all color plots use identical scales: velocity magnitude 0–0.25 m·s^{-1}, vorticity −40 to +40 s^{-1}, and viscous dissipation rate 0–15 W·m^{-3}. While values exceeding these imposed limits appear saturated, these regions are not very large and do not bias the comparison.

4.3 Biphasic waveform

The biphasic waveform consists of two discrete impulses separated by a brief low-energy interval. Clinically, this pattern is frequently observed in healthy ureteral jets and serves as a practical baseline against which transitional or continuous (pathology-leaning) behaviors can be contrasted. The flow concentrates momentum into two short bursts, leading to rapid penetration, strong jet shear layers, and intermittent near-wall recirculation.

4.3.1 Kinetic energy

The biphasic spatial mean kinetic energy (per unit mass) is shown in Figure 4.8. The curve displays two pronounced maxima separated by a trough, consistent with the input biphasic jet velocity waveform. We analyze three instants: (1) first peak at $t_1 = 0.688$ s, (2) trough at $t_2 = 1.324$ s, and (3) second peak at $t_3 = 1.704$ s (red points in Figure 4.8). We can readily observe more intermittency around the second peak, which may result from bladder compliance effects.

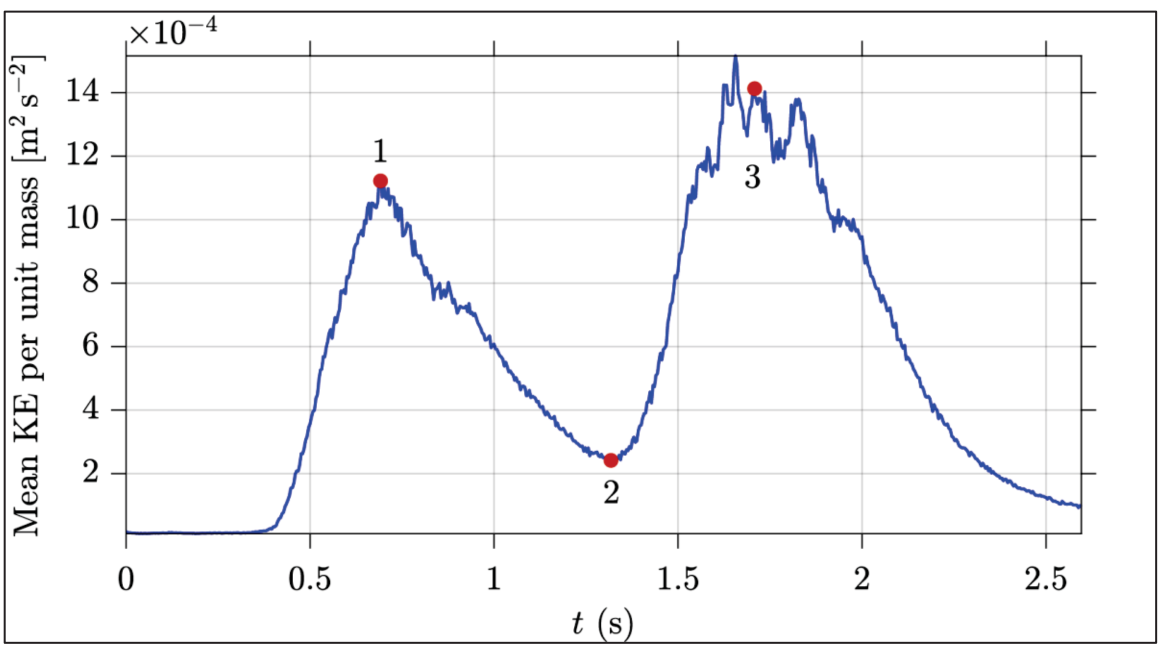

Figure 4.8 Mean kinetic energy per unit mass, KE(t), for the biphasic waveform, red markers 1–3 denote the analysis instants (first peak, trough, second peak)

4.3.2 Velocity field maps

The biphasic jet produces two discrete surges evident in both kinematics and derived fields. Figure 4.9 shows velocity vectors overlaid on velocity magnitude at the three analysis instants. The first surge forms a narrow, high-speed core at 99.73° (relative to the positive x-axis direction), peaking at 33.27 cm·s^{-1} with a 27.02° jet spreading angle, and penetrating rapidly into the bladder. The wide, abrupt velocity range near the UVJ highlights limitations of color and pulsed Doppler. Increasing color Doppler limits to capture detail reduces temporal resolution, so within fixed limits the high-speed core may appear wider and /or longer than it truly is. Pulsed Doppler is scan-line-sensitive, so small placement changes alter peak values and sharpness.

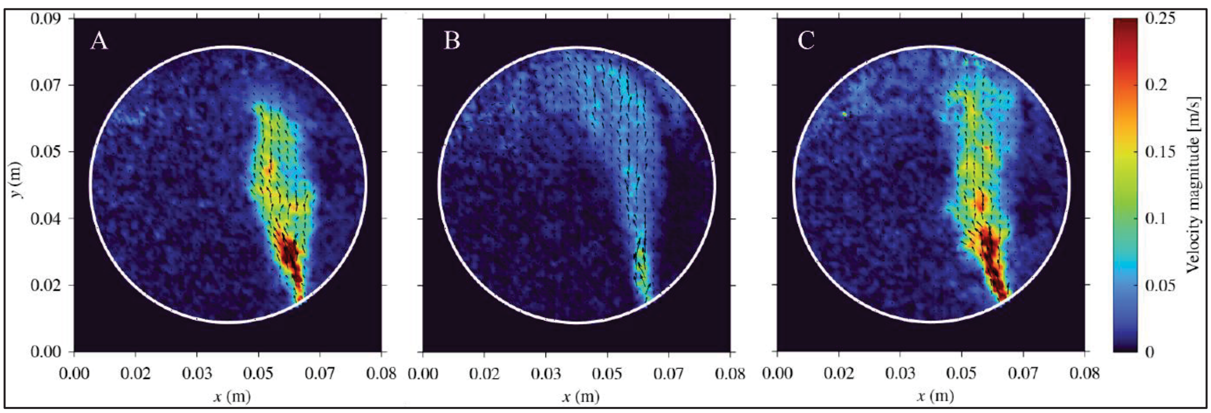

Figure 4.9 Instantaneous velocity magnitude $|u|$ with vectors for the biphasic waveform at the three analysis instants: (a) first peak, (b) trough, (b) second peak

As the jet enters the bladder, it widens from 4.23 mm at the UVJ to 21.28 mm downstream. The local UVJ maximum velocity was 38.6 cm·s^{-1} at $(x, y) = (9.42\ cm, 2.77\ cm)$. At the trough, the core slows to 6.36 cm·s^{-1} with a 12.41° jet spreading angle as the far jet decays and follows the wall curvature, driving large-scale gentle rotation. The second surge re-forms a narrow core (peak velocity of 34.40 cm·s^{-1}) and advances the front beyond the first surge, with a 26.66° jet spreading angle and a brief intensification of near-wall recirculation and mixing.

4.3.3 Vorticity fields

The vorticity field is shown in Figure 4.10. We can observe high vorticity at the boundaries of the jet throughout the ejection, which is typical of shear layers, ranging in magnitude from 155.6 s^{-1} at the peaks to 64.61 s^{-1} at the trough. The jet is observed to break up into small vortices, coherent for a short time, forming in part from the shear layer, which is typically observed as a result of shear layer instability at higher Reynolds numbers. Peak vorticity at the first surge reached 178.6 s^{-1}.

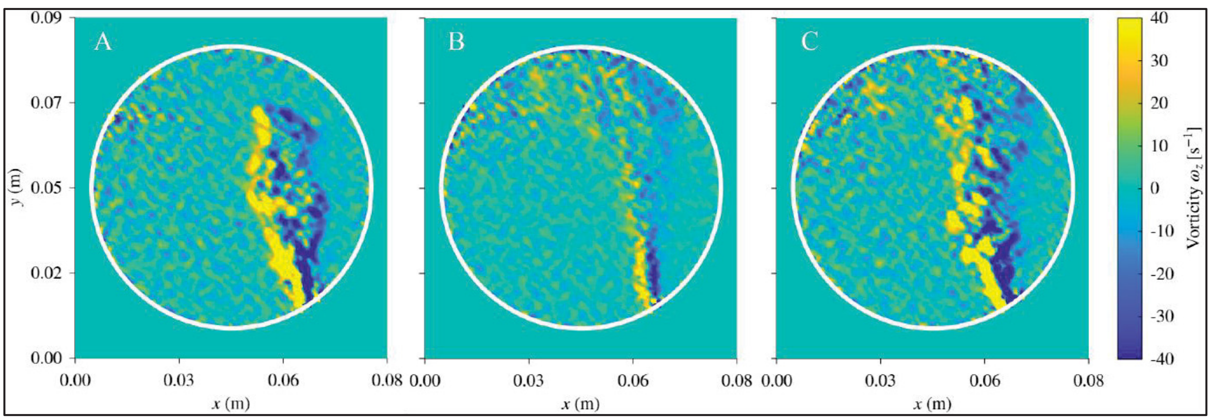

Figure 4.10 Out-of-plane vorticity ω_z for the biphasic waveform at the three analysis instants: (a) first peak, (b) trough, (c) second peak

The mean jet Reynolds number was computed as:

$$\mathrm{Re} = \frac{\rho V D}{\mu} = \frac{4\rho Q}{\pi \mu D} \tag{4.10}$$

with $\rho = 1100$ kg m^{-3}, $\mu = 3.7 \times 10^{-3}$ Pa s , mean flow rate $Q = 3.8 \times 10^{-6}\ m^3 s^{-1}$ and orifice diameter $D = 3.5 \times 10^{-3}$ m . Substitution gives $Re = 411$.

Vortices are carried downstream, gradually decaying into smaller eddies that ultimately dissipate by viscosity. Near the distal wall, an adverse pressure gradient (the fluid is quiescent at the upper bladder) slows the jet and promotes further breakdown. During the trough, only small eddies remain and they follow the curved jet path toward the upper bladder, enhancing mixing and dissipating kinetic energy. The second surge repeats these dynamics and reinforces near-jet vortices, with occasional vortex pairing/merging commonly observed in transient shear-layer instability.

4.3.4 Viscous energy dissipation

Viscous dissipation concentrates near the jet shear layer, core, and on the wall at the location of jet impingement, namely, regions of strong velocity gradients. The small vortices dissipate little energy, their contribution to dissipation is due to the overall jet breakup process and the subsequent decay of the vortices due to viscosity. The spatially-integrated dissipation rate shows the expected double-peak aligned with the two surges and with the $\mathrm{KE}(t)$. At the UVJ, maxima were 148.4 $\mathrm{W \cdot m^{-3}}$ at the first peak, 38.1 $\mathrm{W \cdot m^{-3}}$ at the trough, and 173.4 $\mathrm{W \cdot m^{-3}}$ at the second peak. The larger second peak reflects residual dissipation from the first surge plus new dissipation from the second (Figure 4.11). Overall, the biphasic pattern concentrates energy into two brief, high-intensity events that drive rapid penetration and vigorous mixing.

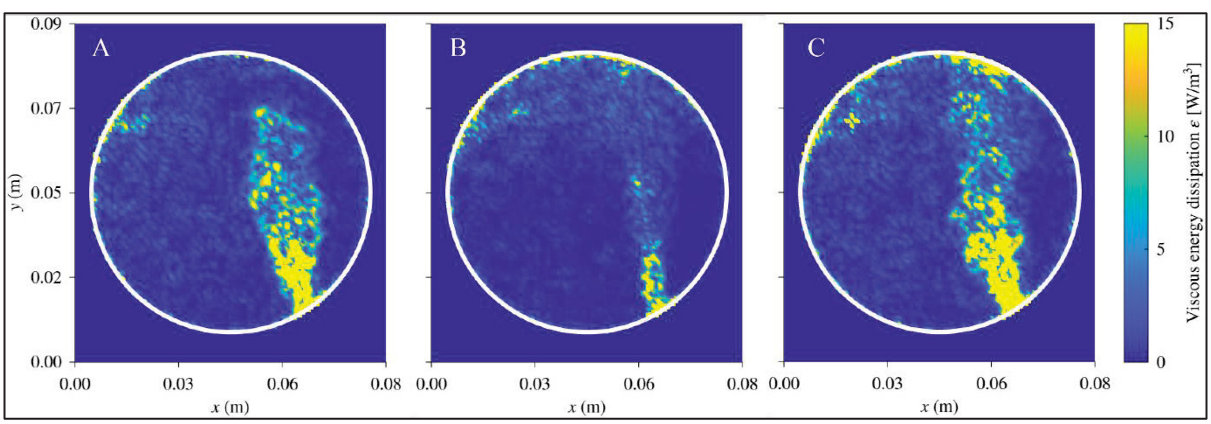

Figure 4.11 Viscous energy dissipation (ε) for the biphasic waveform at the three analysis instants: (a) first peak, (b) trough, (c) second peak

4.4 Transitional waveform

The transitional case bridges the biphasic healthy waveform and the continuous dysfunctional waveform. The waveform displays a moderately pulsatile jet with a broadened primary peak and trough rather than two strong impulses. It delivers the same volume (9.5 mL) over a longer duration (3.0 s), giving a lower mean inflow (3.17 mL·s^{-1}). Compared with the biphasic ureteral jet (Section 4.3), the shear layer growth is smoother with fewer abrupt reorganizations and the near-wall recirculation is more stable. Compared with the continuous ureteral jet (Section 4.5), it retains enough pulsatility to modulate jet penetration and mixing.

4.4.1 Kinetic energy

The mean kinetic energy shows a broadened maximum with a shallow trough (Figure 4.12). The analysis instants are (1) $t_1 = 0.79\ s$ (peak 1), (2) $t_2 = 1.12\ s$ (trough), (3) $t_3 = 1.688\ s$

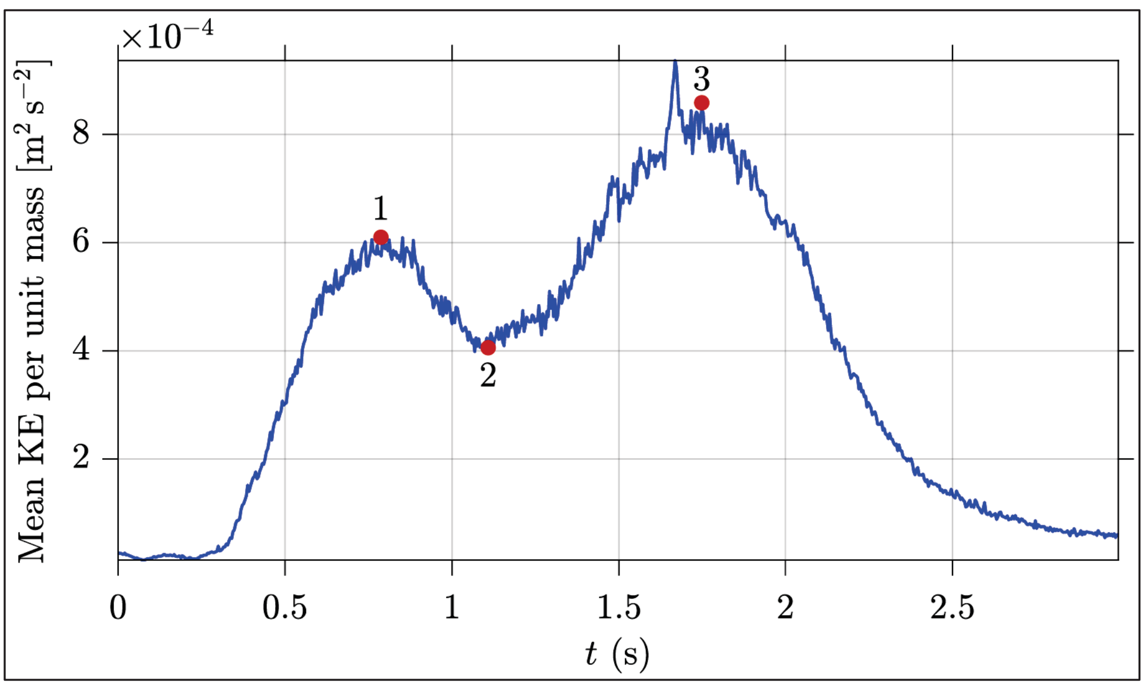

Figure 4.12 Mean kinetic energy per unit mass, KE(t), for the transitional waveform
Red markers 1–3 denote the analysis instants

(peak 2). The second peak is less affected by bladder compliance (no oscillations) than the biphasic case, likely due to the overall lower velocity impulse of the jet.

4.4.2 Velocity field maps

The instantaneous velocity magnitude and velocity vectors are shown at the three instants in Figure 4.13. We observe a coherent jet core with smoother shear layer growth and minimal re-collimation compared with the biphasic ureteral jet. Jet penetration increases monotonically from peak 1 to peak 2, while the near-wall recirculation zone at the upper bladder remains comparatively stable. The first surge forms a narrow jet core at 100.96° relative to the positive x-axis direction, reaches a peak velocity of 23.71 cm·s^{-1}, exhibits a 17.25° jet spreading angle, and penetrates rapidly into the bladder. The highest velocity at the UVJ ($x = 9.49\ cm, y = 3.29 cm$) was 29.02 cm·s^{-1}. The inter-peak trough displayed a velocity of 18.44 cm·s^{-1} with a 15.52° jet spreading angle; the second surge peaked at a velocity of 30.61 cm·s^{-1} with a 23.38° jet spreading angle. Overall, the spreading angles are consistently lower than those observed for the biphasic ureteral jet.

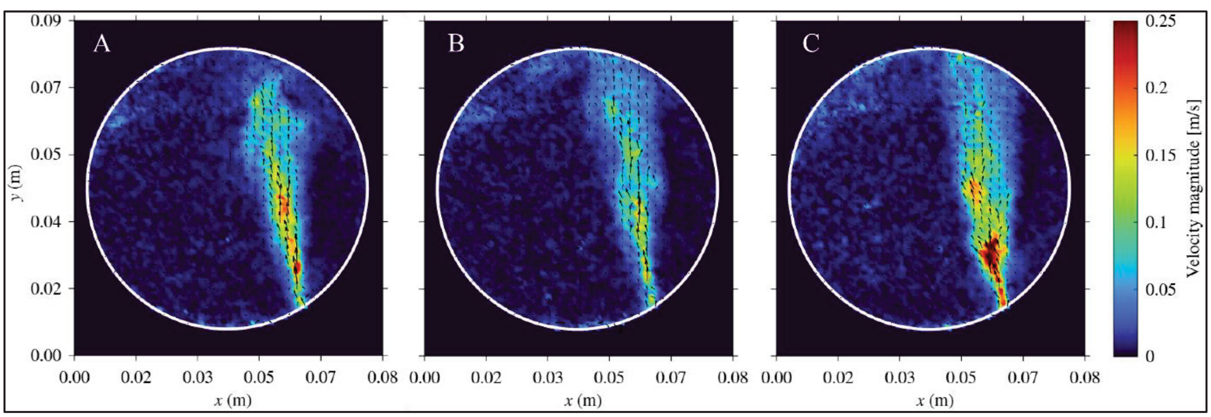

Figure 4.13 Instantaneous velocity magnitude with velocity vectors for the transitional waveform at the three analysis instants: (a) peak 1, (b) trough, (c) peak 2

4.4.3 Vorticity fields

The vorticity (Figure 4.14) envelope persists throughout the plateau and then decays, indicating sustained but gentler shear. The shear layers are broader and less compact, and coherent rollers occur less often, indicating a more stable shear layer. Peak vorticity among the two surges reached 162.5 s^{-1}. With a mean flow rate of $Q = 3.8 \times 10^{-6}\ m^3 s^{-1}$, the mean jet Reynolds number representative of the flow is $Re = 342$ (lower than the biphasic case given the lower overall velocity magnitudes).

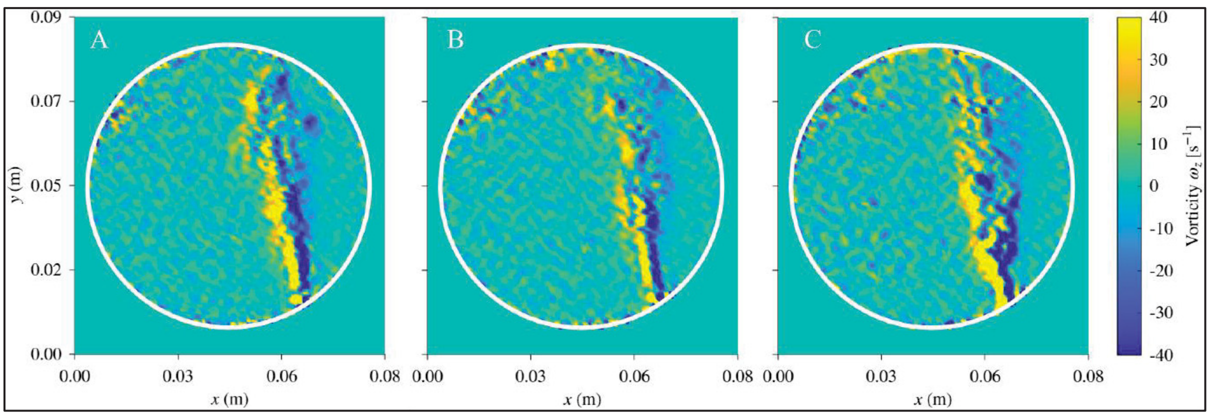

Figure 4.14 Out-of-plane vorticity ω_z for the transitional waveform at the three analysis instants: (a) peak 1, (b) trough, (c) peak 2

4.4.4 Viscous energy dissipation

The dissipation (Figure 4.15) spreads steadily across the shear layer and upper wall region. The spatially-integrated viscous dissipation rate $\dot{E}_v(t)$ exhibits a single rounded maximum with a longer tail. At the UVJ, the maximum local dissipation was 106.3 W·m^{-3} at peak 1, 60.3 W·m^{-3} at the trough, and 107.2 W·m^{-3} at peak 2. Overall, the transitional waveform promotes less vigorous mixing and demonstrates lower instantaneous peaks than the biphasic waveform sustained over a longer interval.

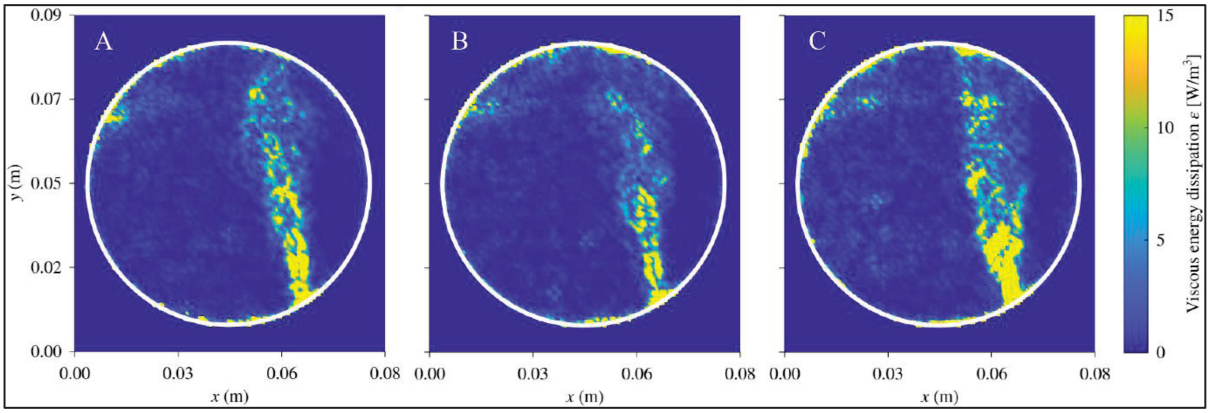

Figure 4.15 Viscous energy dissipation (ε) for the transitional waveform at the three analysis instants: (a) peak 1, (b) trough, (c) peak 2

4.5 Continuous waveform

The continuous waveform represents the most pathological limit of the jet sequence and approximates a nearly steady inflow. It delivers the same total volume (9.5 mL) over the longest duration (3.5 s), giving the lowest mean inflow rate and essentially eliminating pulsatile modulation. In this case, the jet ramps up smoothly to a quasi-steady state and establishes a persistent shear layer with a stable near-wall recirculation at the upper bladder.

4.5.1 Kinetic energy

The mean kinetic energy rises to a broad plateau over the ejection period (Figure 4.16). We select three instants for analysis: (1) early plateau at $t_1 = 0.520$ s, (2) mid-plateau at $t_2 = 1.629$ s, and (3) late plateau at $t_3 = 2.712$ s.

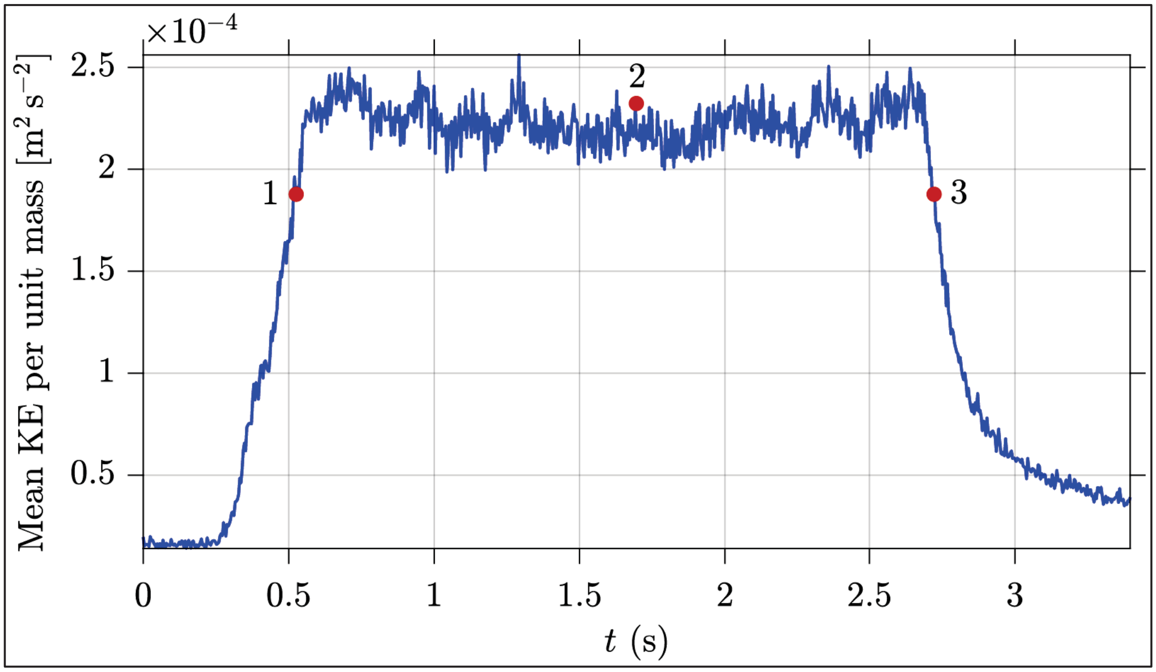

Figure 4.16 Mean kinetic energy per unit mass, KE(t), for the continuous waveform
The red markers 1–3 indicate the analysis instants (early, mid, late plateau)

4.5.2 Velocity field maps

The velocity fields (Figure 4.17) show gradual thickening of the shear layer and steady penetration, with no brief refocusing seen in the latter two cases consisting of two pulses. The jet maintains an average inclination of 95.22° to positive x-axis direction and a mean jet spreading angle of 18.17° ± 1.05°. This spreading angle is lower than the peak angle observed in the transitional case, suggesting that the maximum jet spreading angle alone may serve as a fluid dynamic marker of dysfunction. Because the peak speed is essentially steady once reached, we quantify the flow using instantaneous domain-maximum speeds sampled from t = 1.03–2.68 s with Δt = 0.21 s (every 50 frames), yielding a mean velocity magnitude of 15.21 ± 0.63 cm·s^{-1} (range 14.11–15.85 cm·s^{-1}). The highest velocity at the UVJ ($x = 9.56$ cm, $y = 3.16$ cm) was 16.05 cm·s^{-1}.

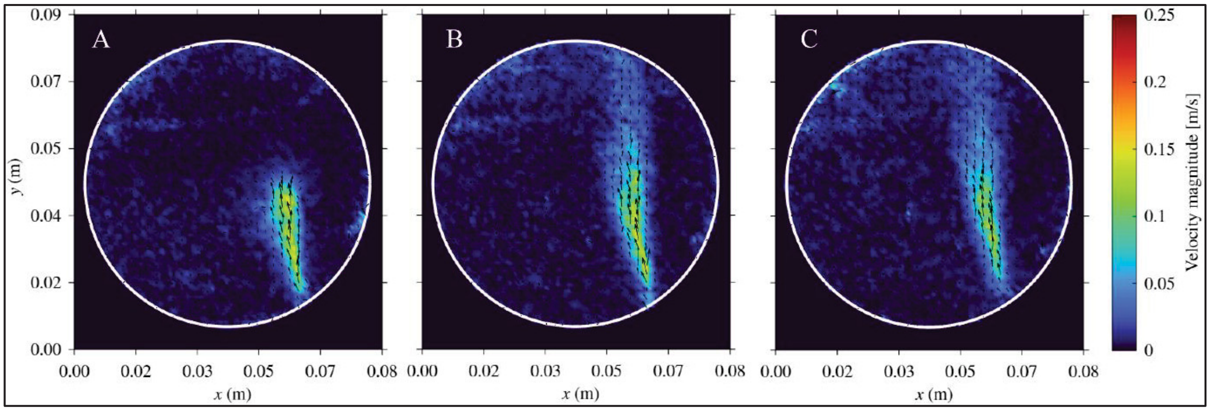

Figure 4.17 Instantaneous velocity magnitude with velocity vectors at the three analysis instants: (a) early plateau, (b) mid-plateau, (c) late plateau

4.5.3 Vorticity fields

The vorticity field is dominated by a stable shear layer, and distinct vortices are rarely observed. As shown in Figure 4.18, mixing is mainly driven by a persistent band of high shear along the jet path, which gradually breaks down downstream. During the plateau phase, peak instantaneous vorticity magnitudes are typically between 66 and 78 s^{-1}, with a maximum value of 80.4 s^{-1}, indicating a strong but relatively steady shear region throughout the continuous jet. The gentle recirculation occurring from jet impingement presents no significant vorticity, except due to shear at the upper bladder wall on the side opposite the jet.

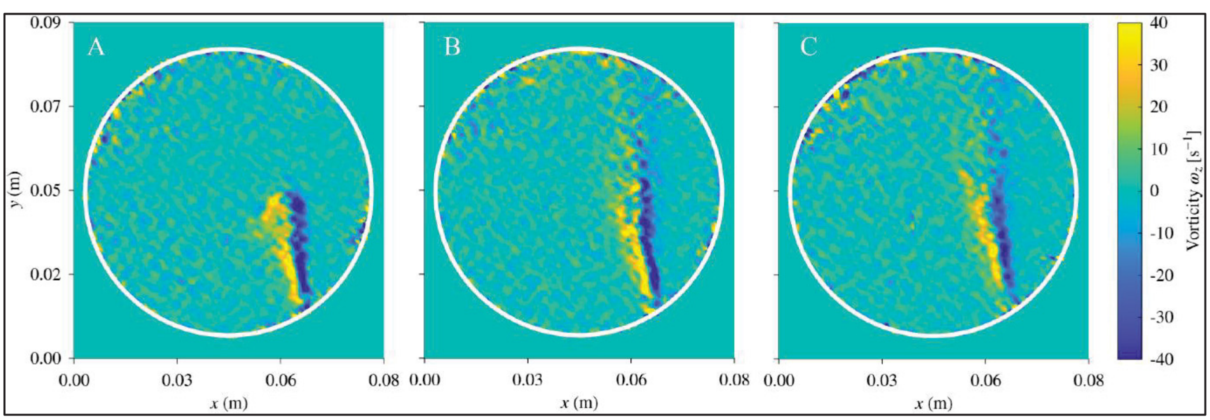

Figure 4.18 Out-of-plane vorticity ω_z at the three analysis instants: (a) early plateau, (b) mid-plateau, (c) late plateau

The mean jet Reynolds number was Re ≈ 294, lower than the previous cases because the injection duration was longer (3.5 s vs 3.0 s) with the same volume, reducing the mean volume flow rate.

4.5.4 Viscous energy dissipation

Dissipation maps show lower peaks over a broader area as the quasi-steady shear persists. The spatially-integrated viscous energy dissipation forms a broad plateau rather than sharp spikes (Figure 4.19). Sampling $t = 1.03$–2.68 s with $\Delta t = 0.21$ s (every 50 frames), the spatial maxima of dissipation averaged 27.36 ± 3.20 W·m^{-3} (range 21.19–33.45 W·m^{-3}), indicating gentler but sustained mixing with less penetration.

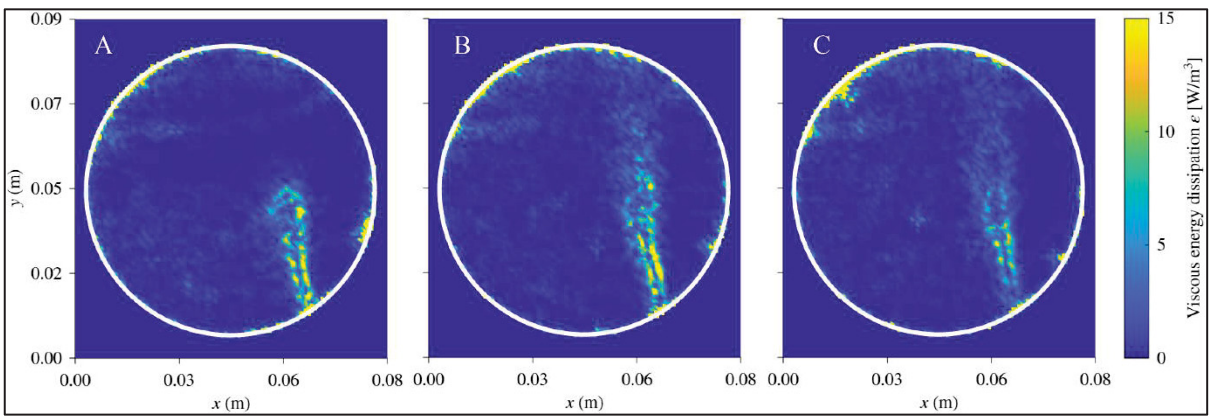

Figure 4.19 Viscous energy dissipation (ε) at the three analysis instants: (a) early plateau, (b) mid-plateau, (c) late plateau

4.6 Waveform Effects on Viscous Dissipation

The biphasic dissipation has two distinct surges with a trough in between. It first ramps up at 0.4–0.5 s to about 0.017 W/m³, then relaxes to 0.010 W/m³, and exhibits a second, sharper rise at 1.5–1.7 s reaching the global maximum of 0.035 W/m³. After this pulse, it decays to 0.007–

0.009 W/m³ by 2.6 s. The peaks are compact, the rise rates are fast, and the time above half-peak is short, so biphasic delivers short, intense bursts of shear separated by partial recovery.

The transitional dissipation has the same sequence (rise, relaxation, and peak reinforcement), but every feature is broader and the amplitudes are lower. Dissipation climbs almost linearly from 0.002 W/m³ to 0.010 W/m³ by 1.1–1.2 s, dips slightly to 1.3–1.4 s, then reaches 0.017–0.018 W/m³ at 1.6–1.7 s, and tails to 0.003–0.004 W/m³ by 2.8–3.0 s. Because ascent and descent are gentler, the time above the half-peak is much longer than in the biphasic case even though the maximum is roughly half. The transitional waveform therefore shifts shear from spikes to a thicker band of moderate dissipation, supporting steadier mixing with lower intensity.

The continuous dissipation does not spike; it rises from 0.004–0.005 W/m³ to a broad plateau at 0.009–0.011 W/m³ that lasts over 1 s, then shows a late crest of 0.014–0.015 W/m³ at 2.5–2.7 s, and finally relaxes to 0.006–0.008 W/m³. The key feature is the long dwell near peak values: once it exceeds half of its maximum, the curve remains elevated for the longest time, dissipating shear steadily and predictably.

Overall, the biphasic waveform displays the largest dissipation for the shortest time, while the continuous waveform displays the lowest dissipation for the longest time. The transitional waveform lies in between, trading some high dissipation for a longer high-shear window (Figure 4.20).

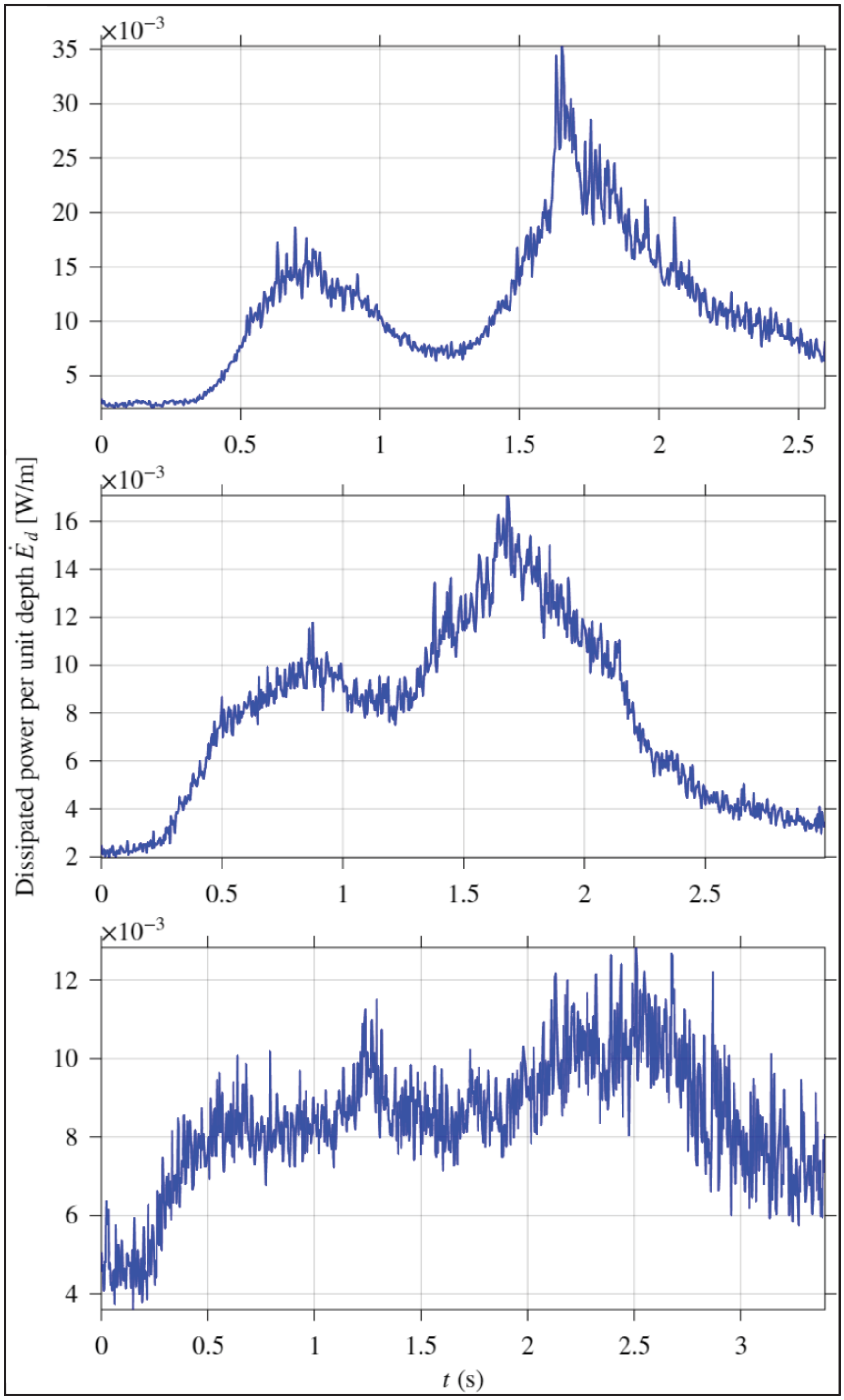

Figure 4.20 Spatially integrated viscous dissipation rate for the jet waveforms

The biphasic case (top) shows two sharp pulses, the transitional case (middle) a broadened two-step profile, and the continuous waveform (bottom) a long low plateau

CONCLUSION

This thesis set out to build and test an *in vitro* bladder flow simulator that mimics human bladder filling and ureteral jet behavior under controlled, repeatable conditions. The main goals were to create an anatomically representative compliant bladder model, to program healthy and pathological ureteral jet waveforms, and to quantify how these different waveforms reorganize intravesical flow as seen by ultrasound and PIV.

Structurally, the simulator combines a transparent octagonal chamber, a compliant silicone bladder phantom, dual syringe-driven ureteral inlets, and intravesical pressure monitoring. The simulator permits optical access for PIV and acoustic access for ultrasound. The phantom was sized to match typical adult bladder volumes, yielding a baseline capacity of 256 mL. Stepwise filling from 256 to 286 mL produced a nearly linear pressure–volume response from 0 to 13.26 mmHg, corresponding to an elastance of 0.44 ± 0.01 mmHg·mL^{-1} (compliance of 1.66 ± 0.02 mL·cmH$_2$O^{-1}). Over this range, the system behaved with reproducible, nearly volume-independent stiffness, indicating that the mechanical design is suitable for controlled studies of bladder filling.

Ultrasound characterization then verified that the programmed inlets reproduce clinically relevant ureteral jet patterns. For biphasic jets (4.00-s ejections, 20–90 cm·s^{-1} peaks), the mean duration error was −0.17 s relative to the input (extremes +0.47 and −0.77 s), and peak velocity errors ranged from +0.5 to −2.2 cm·s^{-1} ($\leq$ 8%), with all realizations falling inside the prescribed velocity bands. For monophasic jets (3.50-s ejections, 20–30 cm·s^{-1} peaks), the mean duration error was −0.21 s (bounded by +0.10 and −0.49 s) and peak velocity errors lay between −2.3 and +1.2 cm·s^{-1} ($\leq$ 9%). For continuous jets (5.00-s plateaus, 10–25 cm·s^{-1} means), the plateau duration matched the programmed 5.00 s within 8% and mean velocity errors remained within about −1.0 to −2.9 cm·s^{-1} (6–15%). Across all cases, the recorded velocity waveforms closely matched published recordings in the literature qualitatively and quantitatively, indicating that the simulator can reliably reproduce both normal and dysfunctional ureteral jet signatures.

Planar PIV in a water–glycerin working fluid was then used to see how delivering the same 9.5 mL volume with different jet waveforms, representing a hypothetical progression of a urogenital condition, changed intravesical flow. With the biphasic (healthy) waveform, the volume was injected over the shortest time (2.5 s), creating a narrow high-speed jet with core velocities of about 33–34 $cm \cdot s^{-1}$ and local UVJ speeds near 39 $cm \cdot s^{-1}$. The biphasic waveform generated compact vortices with peak vorticity 170–180 s^{-1} and two short dissipation peaks of around 0.035 $W \cdot m^{-3}$. In the transitional case, the same volume was spread over about 3.0 s, so peak speeds dropped to about 30 $cm \cdot s^{-1}$. The shear layer thickened, vortices were smaller but longer-lived, and dissipation gathered into a single broader hump of about 0.017–0.018 $W \cdot m^{-3}$. For the continuous (pathology-like) waveform, the jet ramped up smoothly to a quasi-steady plateau near 15 $cm \cdot s^{-1}$ with vorticity in the range of 70–80 s^{-1}. The continuous waveform produced the lowest instantaneous dissipation (~0.014–0.015 $W \cdot m^{-3}$), while keeping the flow near its maximum shear level for the longest time and producing extended regions of slow recirculation along the walls. Overall, this shows that when the waveform changes from biphasic to continuous, the flow inside the bladder changes from short, strong mixing events to weaker but longer-lasting shear with larger slowly recirculating regions; in addition, vortices become weaker and smoother, dissipation peaks become lower and broader (less efficient mixing), and the jet spreading angle becomes smaller (narrower) as the ureteral jet becomes more abnormal.

Taken together, these results show that the presented setup can reliably link ureteral jet waveform shape to the fluid dynamics within the bladder. By keeping the bladder geometry, compliance, and ejected volume fixed and changing only the waveform from biphasic to continuous, we showed that pulsatility alone can strongly alter intravesical flow, with clear signatures in both Doppler ultrasound and PIV. This provides a valuable experimental framework to help interpret clinical ureteral jet measurements and a flexible platform for future studies on how disease, treatment, or anatomy affect bladder filling.

RECOMMENDATIONS

Several simplifying assumptions were made in the design and testing of the bladder flow simulator developed as part of this thesis. Below we describe the main limitations of this thesis and provide recommendations for future work.

With respect to the bladder phantom, while the elastic modulus agreed with the literature at the design volume, the phantom compliance did not ultimately match the average bladder compliance of adults. This implies that the same volume increment produced a larger pressure rise. Overall compliance is also affected by other components of the system (i.e., flexible tubing, valves, connectors). The main consequence in this work is that absolute pressure-volume relationships are not always physiological. However, given the small volume and pressure changes, we do not expect the resulting flow to be far from physiology as we correctly reproduce ureteral jet patterns as observed through color and pulsed Doppler ultrasound. Moreover, the selected phantom geometry was also designed as an idealized ellipsoidal bladder representing average adult dimensions. In reality, there is significant inter- and intra-patient variability in bladder shape and size. Patient-specific studies can help to further validate the ability of the simulator to reproduce physiology. We also add that the ureteral orifices were not active. The addition of a miniature duckbill valve can help reproduce the active opening and closing dynamics of the UVJ.

The working fluids were also simplified for our application. The saline medium possesses fluid properties that are similar to urine, though the lack of backscatter impairs measured velocity peaks using ultrasound. Moreover, repeated injections gradually reduced acoustic contrast (reduction in density difference between the ejected fluid and that within the bladder). As a result, frequent resetting (flushing and refilling) of the experiment was required. The water–glycerin mixture with tracer particles for PIV improved signal quality, though the fluid properties are different from urine and we opted to match the Reynolds and Womersley numbers with the hypothesis that these nondimensional numbers are most important to the resulting fluid dynamics. In future work, a thorough study is required to establish a urine analog that is suitable in terms of both fluid properties as well as optical properties for PIV.

The PIV analysis in this study was designed to provide a first detailed characterization of the intravesical flow beyond standard color and pulsed Doppler imaging. The seeding quality imposed some practical limits. Over time, particles adhered to the bladder wall and were not easily resuspended, requiring periodic flushing and cleaning of the bladder interior to maintain optical clarity of the phantom. We also limit measurements to 2D, which agrees with clinical practice. A natural extension for future work is to consider volumetric measurements. Our mock study, considering a gradual transition of a healthy biphasic ureteral jet waveform to a dysfunctional continuous waveform, is notably hypothetical. As a result, the fluid dynamics analyses, although promising for diagnostic purposes, require further *in vivo* validation. In future work, it would be interesting to conduct a true prospective study *in vivo* and subsequently replicate the conditions *in vitro* on the bladder flow simulator to fine tune the flow-based diagnostic metrics such as total viscous dissipation.

BIBLIOGRAPHY

Adrian, R. J., & Westerweel, J. (2011). Particle image velocimetry. *The Aeronautical Journal,* 116(1176), 219–220. https://doi.org/10.1017/S0001924000006734

Ahyou, J., Li, Y., Thangarajah, P., Wu, Y., & Hyun, C. (2023). Development of an urinary bladder simulator, SIMBA - Silicone-based Interactive Model of Bladder Anatomy. *Continence*. https://ics-eus.org/2023/abstract/716

Andersson, K.-E., & Arner, A. (2004). Urinary bladder contraction and relaxation: Physiology and pathophysiology. *Physiological Reviews*, *84*(3), 935–986. https://doi.org/10.1152/physrev.00038.2003

Baker, S. M., & Middleton, W. D. (1992). Color Doppler sonography of ureteral jets in normal volunteers: Importance of the relative specific gravity of urine in the ureter and bladder. *AJR. American Journal of Roentgenology*, *159*(4), 773–775. https://doi.org/10.2214/ajr.159.4.1529841

Barker, A. J., van Ooij, P., Bandi, K., Garcia, J., Albaghdadi, M., McCarthy, P., Bonow, R. O., Carr, J., Collins, J., Malaisrie, C., & Markl, M. (2014). Viscous Energy Loss in the Presence of Abnormal Aortic Flow. *Magnetic Resonance in Medicine : Official Journal of the Society of Magnetic Resonance in Medicine / Society of Magnetic Resonance in Medicine*, *72*(3), 620–628. https://doi.org/10.1002/mrm.24962

Berry, S. J., Coffey, D. S., Walsh, P. C., & Ewing, L. L. (1984). The development of human benign prostatic hyperplasia with age. *The Journal of Urology*, *132*(3), 474–479. https://doi.org/10.1016/s0022-5347(17)49698-4

Yezitronix Bladder Scanner Phantom. (n.d.). Retrieved October 15, 2025, from https://www.yezitronix.com/html-subpages/bladder-scanner-phantom.html

Burge, H. J., Middleton, W. D., McClennan, B. L., & Hildebolt, C. F. (1991). Ureteral jets in healthy subjects and in patients with unilateral ureteral calculi: Comparison with color Doppler US. *Radiology*, *180*(2), 437–442. https://doi.org/10.1148/radiology.180.2.2068307

Byun, S.-S., Kim, H. H., Lee, E., Paick, J.-S., Kamg, W., & Oh, S.-J. (2003). Accuracy of bladder volume determinations by ultrasonography: Are they accurate over entire bladder volume range? *Urology*, *62*(4), 656–660. https://doi.org/10.1016/S0090-4295(03)00559-4

Campbell-Walsh Urology 12th Edition Review. (2020). https://shop.elsevier.com/books/campbell-walsh-urology-12th-edition-review/partin/978-0-323-63969-9

Cebral, J. R., Mut, F., Weir, J., & Putman, C. M. (2011). Association of hemodynamic characteristics and cerebral aneurysm rupture. *AJNR. American Journal of Neuroradiology*, *32*(2), 264–270. https://doi.org/10.3174/ajnr.A2274

Choi, E., Waldbillig, F., Jeong, M., Li, D., Goyal, R., Weber, P., Miernik, A., Grüne, B., Hein, S., Suarez-Ibarrola, R., Kriegmair, M. C., & Qiu, T. (2021). Soft Urinary Bladder Phantom for Endoscopic Training. *Annals of Biomedical Engineering*, *49*(9), 2412–2420. https://doi.org/10.1007/s10439-021-02793-0

Cox, I. H., Erickson, S. J., Foley, W. D., & Dewire, D. M. (1992). Ureteric jets: Evaluation of normal flow dynamics with color Doppler sonography. *American Journal of Roentgenology*, *158*(5), 1051–1055. https://doi.org/10.2214/ajr.158.5.1566665

Delair, S. M., & Kurzrock, E. A. (2006). Clinical utility of ureteral jets: Disparate opinions. *Journal of Endourology*, *20*(2), 111–114. https://doi.org/10.1089/end.2006.20.111

Di Labbio, G., & Kadem, L. (2018). Jet collisions and vortex reversal in the human left ventricle. *Journal of Biomechanics*, *78*, 155–160. https://doi.org/10.1016/j.jbiomech.2018.07.023

Etebari, A., & Vlachos, P. P. (2006). Improvements on the accuracy of derivative estimation from DPIV velocity measurements. *Experiments in Fluids*, *40*(3), 500–502. https://doi.org/10.1007/s00348-005-0085-6

Female Pelvic Ultrasound Phantom Full set (7weeks) | KYOTO KAGAKU. (n.d.). Retrieved October 15, 2025, from https://www.kyotokagaku.com/en/products_data/us-10a

Foxman, B. (2014). Urinary tract infection syndromes: Occurrence, recurrence, bacteriology, risk factors, and disease burden. *Infectious Disease Clinics of North America*, *28*(1), 1–13. https://doi.org/10.1016/j.idc.2013.09.003

Gajewski, J. B., Schurch, B., Hamid, R., Averbeck, M., Sakakibara, R., Agrò, E. F., Dickinson, T., Payne, C. K., Drake, M. J., & Haylen, B. T. (2018). An International Continence Society (ICS) report on the terminology for adult neurogenic lower urinary tract dysfunction (ANLUTD). *Neurourology and Urodynamics*, *37*(3), 1152–1161. https://doi.org/10.1002/nau.23397

Gemmell, C., Edwards, C., & Reddan, T. (2024). Diagnostic Accuracy of Ureteric Jet Angle Measurement Using Color Doppler Ultrasonography in Children With Vesico-Ureteric

Reflux. *Journal of Ultrasound in Medicine*, *43*(11), 2015–2025. https://doi.org/10.1002/jum.16543

Gharib, M., Rambod, E., Kheradvar, A., Sahn, D. J., & Dabiri, J. O. (2006). Optimal vortex formation as an index of cardiac health. *Proceedings of the National Academy of Sciences*, *103*(16), 6305–6308. https://doi.org/10.1073/pnas.0600520103

Glass Clark, S., Nagle, A. S., Bernardo, R., Vinod, N., Carucci, L., Carroll, A., Speich, J., & Klausner, A. P. (2020). Use of Ultrasound Urodynamics to Identify Differences in Bladder Shape Between Individuals With and Without Overactive Bladder. *Female Pelvic Medicine & Reconstructive Surgery*, *26*(10), 635–639. https://doi.org/10.1097/SPV.0000000000000638

Gyampoh, B., Crouch, N., O'Brien, P., O'Sullivan, C., & Cutner, A. (2004). Intrapartum ultrasound estimation of total bladder volume. *BJOG: An International Journal of Obstetrics & Gynaecology*, *111*(2), 103–108. https://doi.org/10.1046/j.1471-0528.2003.51107.x-i1

Hakenberg, O. W., Linne, C., Manseck, A., & Wirth, M. P. (2000). Bladder wall thickness in normal adults and men with mild lower urinary tract symptoms and benign prostatic enlargement. *Neurourology and Urodynamics*, *19*(5), 585–593. https://doi.org/10.1002/1520-6777(2000)19:5%253C585::AID-NAU5%253E3.0.CO;2-U

Hall, J. E., Hall, J. E., & Guyton, A. C. (2011). *Guyton and Hall textbook of medical physiology: Student consult. Activate at studentconsult.com. Searchable full text online* (12. ed). Saunders, Elsevier.

Hassan, W., Sharif, I., El Khalid, S., Ellahibux, K., Sultan, S., Waqar, A., Zohaib, A., & Yousuf, F. (2021). Doppler-Assessed Ureteric Jet Frequency: A Valuable Predictor of Ureteric Obstruction. *Cureus*, *13*(9), e18290. https://doi.org/10.7759/cureus.18290

Hayan, F., Bacha, R., Farooq, S. M. Y., Hassan, Z., Yousaf, M., Gilani, S. A., Javed, M., Fatima, M., & Zubair, M. (2019). *Doppler Comparison between Ureteric Obstruction and Ureteric Jet Velocity*. *1*.

Inman, B. A., Etienne, W., Rubin, R., Owusu, R. A., Oliveira, T. R., Rodriques, D. B., Maccarini, P. F., Stauffer, P. R., Mashal, A., & Dewhirst, M. W. (2013). The impact of temperature and urinary constituents on urine viscosity and its relevance to bladder hyperthermia treatment. *International Journal of Hyperthermia: The Official Journal of European Society for Hyperthermic Oncology, North American Hyperthermia Group*, *29*(3), 206–210. https://doi.org/10.3109/02656736.2013.775355

Irwin, D. E., Kopp, Z. S., Agatep, B., Milsom, I., & Abrams, P. (2011). Worldwide prevalence estimates of lower urinary tract symptoms, overactive bladder, urinary incontinence and bladder outlet obstruction. *BJU International*, *108*(7), 1132–1138. https://doi.org/10.1111/j.1464-410X.2010.09993.x

Jandaghi, A. B., Falahatkar, S., Alizadeh, A., Kanafi, A. R., Pourghorban, R., Shekarchi, B., Zirak, A. K., & Esmaeili, S. (2013). Assessment of ureterovesical jet dynamics in obstructed ureter by urinary stone with color Doppler and duplex Doppler examinations. *Urolithiasis*, *41*(2), 159–163. https://doi.org/10.1007/s00240-012-0542-7

Jesuthasan, A., Ali, A., Lee, J. K. W., & Rutherfurd-Markwick, K. (2022). Assessment of Changes in Physiological Markers in Different Body Fluids at Rest and after Exercise. *Nutrients*, *14*(21), 4685. https://doi.org/10.3390/nu14214685

Johnson, B., Campbell, S., & Campbell-Kyureghyan, N. (2020). Biomechanical properties of abdominal organs under tension with special reference to increasing strain rate. *Journal of Biomechanics*, *109*, 109914. https://doi.org/10.1016/j.jbiomech.2020.109914

Juri, H., Yamamoto, K., & Narumi, Y. (2016). Analyses of the Anatomy of the Ureter near Ureterovesical Junction on the Unenhanced CT. *Open Journal of Radiology*, *06*(02), 84–91. https://doi.org/10.4236/ojrad.2016.62012

Keane, R. D., & Adrian, R. J. (1990). Optimization of particle image velocimeters. I. Double pulsed systems. *Measurement Science and Technology*, *1*(11), 1202. https://doi.org/10.1088/0957-0233/1/11/013

Kirsch, A. J., Kaye, J. D., Cerwinka, W. H., Watson, J. M., Elmore, J. M., Lyles, R. H., Molitierno, J. A., & Scherz, H. C. (2009). Dynamic Hydrodistention of the Ureteral Orifice: A Novel Grading System With High Interobserver Concordance and Correlation With Vesicoureteral Reflux Grade. *Journal of Urology*, *182*(4S), 1688–1693. https://doi.org/10.1016/j.juro.2009.02.061

Kozomara, M., Birkhäuser, V., Anderson, C. E., Bywater, M., Gross, O., Kiss, S., Knüpfer, S. C., Koschorke, M., Leitner, L., Mehnert, U., Sadri, H., Sammer, U., Stächele, L., Tornic, J., Brinkhof, M. W. G., Liechti, M. D., & Kessler, T. M. (2023). Neurogenic Lower Urinary Tract Dysfunction in the First Year After Spinal Cord Injury: A Descriptive Study of Urodynamic Findings. *Journal of Urology*, *209*(1), 225–232. https://doi.org/10.1097/JU.0000000000003021

Lamonerie, L., Marret, E., Deleuze, A., Lembert, N., Dupont, M., & Bonnet, F. (2004). Prevalence of postoperative bladder distension and urinary retention detected by ultrasound measurement. *British Journal of Anaesthesia*, *92*(4), 544–546. https://doi.org/10.1093/bja/aeh099

Lele, S. K. (1992). Compact finite difference schemes with spectral-like resolution. *Journal of Computational Physics*, *103*(1), 16–42. https://doi.org/10.1016/0021-9991(92)90324-R

Leslie, S. W., Rathi, B. M., Sharif, S., & Rout, P. (2025). 24-Hour Urine Collection and Analysis. In *StatPearls*. StatPearls Publishing. http://www.ncbi.nlm.nih.gov/books/NBK482482/

Leung, V. Y., Chu, W. C., Yeung, C., & Metreweli, C. (2007). Doppler waveforms of the ureteric jet: An overview and implications for the presence of a functional sphincter at the vesicoureteric junction. *Pediatric Radiology*, *37*(5), 417–425. https://doi.org/10.1007/s00247-007-0433-1

Leung, V. Y. F., Metreweli, C., & Yeung, C. K. (2002). THE URETERIC JET DOPPLER WAVEFORM AS AN INDICATOR OF VESICOURETERIC SPHINCTER FUNCTION IN ADULTS AND CHILDREN. AN OBSERVATIONAL STUDY. *Ultrasound in Medicine and Biology*, *28*(7).

Leung, V. Y.-F., Chu, W. C.-W., Yeung, C.-K., & Metreweli, C. (2006). Ureteric jet Doppler waveform and bladder wall thickness in children with nocturnal enuresis. *Pediatric Research*, *60*(5), 582–586. https://doi.org/10.1203/01.PDR.0000242304.64309.6c

Li, C., Guan, G., Zhang, F., Song, S., Wang, R. K., Huang, Z., & Nabi, G. (2014). Quantitative elasticity measurement of urinary bladder wall using laser-induced surface acoustic waves. *Biomedical Optics Express*, *5*(12), 4313. https://doi.org/10.1364/BOE.5.004313

Lukacz, E. S., Sampselle, C., Gray, M., MacDiarmid, S., Rosenberg, M., Ellsworth, P., & Palmer, M. H. (2011). A healthy bladder: A consensus statement. *International Journal of Clinical Practice*, *65*(10), 1026–1036. https://doi.org/10.1111/j.1742-1241.2011.02763.x

Malek, A. M., Alper, S. L., & Izumo, S. (1999). Hemodynamic shear stress and its role in atherosclerosis. *JAMA*, *282*(21), 2035–2042. https://doi.org/10.1001/jama.282.21.2035

Martins, P. A. L. S., Filho, A. L. S., Fonseca, A. M. R. M., Santos, A., Santos, L., Mascarenhas, T., Jorge, R. M. N., & Ferreira, A. J. M. (2011). Uniaxial mechanical behavior of the human female bladder. *International Urogynecology Journal*, *22*(8), 991–995. https://doi.org/10.1007/s00192-011-1409-0

Meththananda, I. M., Parker, S., Patel, M. P., & Braden, M. (2009). The relationship between Shore hardness of elastomeric dental materials and Young's modulus. *Dental Materials: Official Publication of the Academy of Dental Materials*, *25*(8), 956–959. https://doi.org/10.1016/j.dental.2009.02.001

Ogobuiro, I., & Tuma, F. (2025). Physiology, Renal. In *StatPearls*. StatPearls Publishing. http://www.ncbi.nlm.nih.gov/books/NBK538339/

O'Reilly, P., Aurell, M., Britton, K., Kletter, K., Rosenthal, L., & Testa, T. (1996). Consensus on diuresis renography for investigating the dilated upper urinary tract. Radionuclides in Nephrourology Group. Consensus Committee on Diuresis Renography. *Journal of Nuclear Medicine: Official Publication, Society of Nuclear Medicine*, *37*(11), 1872–1876

Park, W. H. (2010). Management of Low Compliant Bladder in Spinal Cord Injured Patients. *LUTS: Lower Urinary Tract Symptoms*, *2*(2), 61–70. https://doi.org/10.1111/j.1757-5672.2010.00076.x

Price, D., Wallbridge, D., & Stewart, M. (2000). Tissue Doppler imaging: Current and potential clinical applications. *Heart*, *84*(Suppl 2), ii11–ii18. https://doi.org/10.1136/heart.84.suppl_2.ii11

Raffel, M., Willert, C. E., Scarano, F., Kähler, C. J., Wereley, S. T., & Kompenhans, J. (2018). *Particle Image Velocimetry: A Practical Guide*. Springer International Publishing. https://doi.org/10.1007/978-3-319-68852-7

Rahn, D. D., Bleich, A. T., Wai, C. Y., Roshanravan, S. M., Wieslander, C. K., Schaffer, J. I., & Corton, M. M. (2007). Anatomic relationships of the distal third of the pelvic ureter, trigone, and urethra in unembalmed female cadavers. *American Journal of Obstetrics and Gynecology*, *197*(6), 668.e1-668.e4. https://doi.org/10.1016/j.ajog.2007.08.068

Sam, P., Jiang, J., Leslie, S. W., & LaGrange, C. A. (2025). Anatomy, Abdomen and Pelvis, Sphincter Urethrae. In *StatPearls*. StatPearls Publishing. http://www.ncbi.nlm.nih.gov/books/NBK482438/

Scales, C. D., Smith, A. C., Hanley, J. M., Saigal, C. S., & Urologic Diseases in America Project. (2012). Prevalence of kidney stones in the United States. *European Urology*, *62*(1), 160–165. https://doi.org/10.1016/j.eururo.2012.03.052

Segur, J. B., & Oberstar, H. E. (1951). Viscosity of Glycerol and Its Aqueous Solutions. *Industrial & Engineering Chemistry*, *43*(9), 2117–2120. https://doi.org/10.1021/ie50501a040

Servo Cylinder Configurator – Ultra Motion. (n.d.). Retrieved October 22, 2025, from https://www.ultramotion.com/servo-cylinder-configurator

Shermadou, E. S., Rahman, S., & Leslie, S. W. (2025). Anatomy, Abdomen and Pelvis: Bladder. In *StatPearls*. StatPearls Publishing. http://www.ncbi.nlm.nih.gov/books/NBK531465/

Song, H.-J., Cho, S.-T., & Kim, K.-K. (2010). Investigation of the Location of the Ureteral Stone and Diameter of the Ureter in Patients with Renal Colic. *Korean Journal of Urology*, *51*(3), 198. https://doi.org/10.4111/kju.2010.51.3.198

Standring, S. (Ed.). (2016). *Gray's anatomy: The anatomical basis of clinical practice* (Forty-first edition). Elsevier Limited.

Urine Specific Gravity. (n.d.). Ucsfhealth.Org. Retrieved October 15, 2025, from https://www.ucsfhealth.org/medical-tests/urine-specific-gravity-test

Wu, C.-C. (2010). Ureteric Jet. *Journal of Medical Ultrasound*, *18*(4), 141–146. https://doi.org/10.1016/j.jmu.2010.11.001

Wyndaele, J. J. (1998). The normal pattern of perception of bladder filling during cystometry studied in 38 young healthy volunteers. *The Journal of Urology*, *160*(2), 479–481.

Yang, X., Chen, H., Zheng, Y., Qu, S., Wang, H., & Yi, F. (2022). Disease burden and long-term trends of urinary tract infections: A worldwide report. *Frontiers in Public Health*, *10*, 888205. https://doi.org/10.3389/fpubh.2022.888205

Yao, M., & Simoes, A. (2025). Urodynamic Testing and Interpretation. In *StatPearls*. StatPearls Publishing. http://www.ncbi.nlm.nih.gov/books/NBK562310/

Yildirim, D., Gurses, B., & Kocaoglu, M. (2010). Doppler characteristics of the ureteric jet-streams in patients with non-obstructive nephrolithiasis: Mechanism of dysfunctional propagation of the peristaltic activity from the pelvic pacemaker to the ureterovesical sphincter. *Türk Üroloji Dergisi/Turkish Journal of Urology*, *36*(3), 280–285. https://doi.org/10.5152/tud.2010.030

Zheng, S., Amado, P., Obrist, D., Burkhard, F., & Clavica, F. (2022). An in vitro bladder model with physiological dynamics: Vesicoureteral reflux alters stent encrustation pattern. *Frontiers in Bioengineering and Biotechnology*, *10*, 1028325. https://doi.org/10.3389/fbioe.2022.1028325

Zuiderveld, K. (1994). Contrast limited adaptive histogram equalization. In *Graphics gems IV* (pp. 474–485). Academic Press Professional, Inc.